Molecular Dynamics Simulations of the Wetting Behavior of Nanodroplets of Water and Aqueous Surfactant Solutions on Solid Substrates of Varying Surface Energy

by

Jonathan D. Halverson

A dissertation submitted to the Graduate Faculty in Chemical Engineering in partial fulfillment of the requirements for the degree of Doctor of Philosophy, City University of New York

2008

This manuscript has been read and accepted for the
Graduate Faculty in Engineering in satisfaction of the
dissertation requirement for the degree of Doctor of Philosophy.

Date	Prof. Joel Koplik (Co-mentor) Chair of Examining Committee
Date	Mumtaz K. Kassir Executive Officer

Prof. Charles Maldarelli (Co-mentor)

Prof. Alexander Couzis (Co-mentor)

Prof. Jae W. Lee

Prof. M. Silvina Tomassone (Rutgers University)

Supervision Committee

City University of New York

Abstract

Molecular Dynamics Simulations of the Wetting Behavior of Nanodroplets of Water and Aqueous Surfactant Solutions on Solid Substrates of Varying Surface Energy

by

Jonathan D. Halverson

Advisors: Prof. Joel Koplik, Prof. Charles Maldarelli, and Prof. Alexander Couzis

Trisiloxane surfactants have the unique ability to promote the rapid and complete wetting of aqueous drops on hydrophobic, hydrocarbon substrates. Molecular dynamics simulations have been conducted to elucidate the mechansim by which these surfactants operate.

The substrates used in this work are graphite and self-assembled monolayers (SAMs) of varying surface energy. Before investigating aqueous surfactant droplets, pure droplets of water on SAMs composed of 1-undecanethiol ($CH_3(CH_2)_{10}SH$) and 11-mercapto-1-undecanol ($HOCH_2(CH_2)_{10}SH$) on Au(111) are considered. With χ_p denoting the mole fraction of $HOCH_2$-terminated chains, the equilibrium contact angles of water droplets consisting of 4000 molecules on homogeneous monolayers are reported for χ_p = 0, 0.25, 0.5, 0.75, and 1. Good agreement is seen between the simulation results and experimental data. Phase separated monolayers are also considered. The nanoscale wetting behavior of the SAM is found to be sensitive to its nanostructure.

Wetting simulations of droplets of aqueous trisiloxane ($M(D'E_4OH)M$) and alkyl polyethoyxlate ($C_{12}E_4$) solutions were conducted. Spherical and cylindrical droplet

shapes were considered. While the $C_{12}E_4$ systems showed a behavior that is consistent with a simple wetting theory based on the Young equation, the trisiloxane systems showed a different behavior. For initial surface concentrations above the maximum packing concentration the M(D′E_4OH)M/H_2O droplet did not spread appreciably. When the initial surface concentration was below the maximum packing concentration the trisiloxane droplet showed increased spreading but the final contact angle was still large.

The interfacial and bulk properties of aqueous trisiloxane and alkyl polyethoxylate surfactant solutions were investigated. The surfactant molecules of a 35.2 wt% M(D′E_4OH)M solution, which were randomly distributed throughout the solution at initialization, were found to self-assemble into a bilayer in less than 50 ns at 375 K. The alkyl polyethyoxylate surfactant was also found to form a bilayer on the same time scale. The adsorption isotherms at 298.15 K for each surfactant system were determined. In the case of the M(D′E_4OH)M monolayer, the simulation results were found to overestimate the experimental values while for $C_{12}E_4$ the computed tensions are found to be within one standard deviation of the experimental data for each surface concentration considered.

Acknowledgements

Many thanks to Joel Koplik, German Drazer, Igor Baryshev, Junjun Mao, Makonnen Payne, Mary Wright, Andy Eng, Jacob Kurzak, Ken Tasaki, Berend Smit and CECAM, the Levich Institute, the San Diego Supercomputer Center, and the National Energy Research Scientific Computing Center.

Contents

1 Introduction **1**

1.1 Wetting Phenomena and Surfactants 1

1.2 Superspreading 4

1.3 Computational Wetting Studies 9

2 Methodology **14**

2.1 Classical Dynamics 15

2.2 Intermolecular Potential Functions 16

2.3 Constant-Temperature Simulations 17

2.4 Atomic Systems with Molecular Constraints 19

2.5 Atom Evolution Equation 21

2.6 Parallel Simulations 24

3 Wetting Behavior of Nanodroplets of Water on Homogeneous and Phase Separated Self-Assembled Monolayers **26**

3.1 Introduction 27

3.2 SAM Model 33

3.3 Simulation Methodology 39

3.4 Results and Discussion 42

3.4.1 SAM Structural Properties 42

3.4.2 Homogeneous Monolayers 47
3.4.3 Phase Separated Monolayers 57
3.4.4 Effect of Line Tension 67
3.5 Conclusions 72

4 Motion of a Nanodroplet of Pure Liquid on a Wetting Gradient 74
4.1 Introduction 75
4.1.1 Theory 79
4.2 Simulation Methodology 81
4.2.1 Lennard-Jones System 81
4.2.2 Water-SAM System 82
4.3 Results and Discussion 85
4.3.1 Lennard-Jones System 85
4.3.2 Water-SAM System 86
4.4 Conclusions 105

5 Wetting of Hydrophobic Substrates by Nanodroplets of Aqueous Superspreading and Alkyl Polyethoxylate Surfactant Solutions 107
5.1 Introduction 108
5.2 Simulation Methodology 109
5.2.1 Wetting of Graphite by Aqueous Surfactant Droplets 110
5.2.2 Wetting of SAMs by Aqueous Surfactant Droplets 112
5.3 Results and Discussion 113
5.3.1 Spherical Droplets 113
5.3.2 Cylindrical Droplets 121
5.4 Conclusions 122

6 Bulk and Interfacial Properties of Aqueous Superspreading and Alkyl Polyethoxylate Surfactant Solutions **125**

6.1 Introduction 126

6.2 Simulation Methodology 129

6.2.1 Solid-Liquid Interface and Bulk Properties 130

6.2.2 Properties of the Liquid-Vapor Interface 131

6.3 Results and Discussion 132

6.3.1 Solid-Liquid Interface and Bulk Properties 132

6.3.2 Properties of the Liquid-Vapor Interface 142

6.4 Conclusions 149

7 Summary and Future Work **150**

A Surfactant Force Field **156**

B Best-Fit Ellipse **160**

Bibliography **163**

List of Tables

3.1 Force field for the MD simulations. [a]These parameters apply to SPC/E water while all others apply to the binary SAM. [b]A CH_2 united atom is neutral except when directly bonded to an alcohol group where it has a partial charge of $0.435e$. The OPLS combining rules are $\sigma_{ij} = \sqrt{\sigma_{ii}\sigma_{jj}}$ and $\epsilon_{ij} = \sqrt{\epsilon_{ii}\epsilon_{jj}}$. 41

3.2 Wetting behavior of a nanodroplet of water on a homogeneous SAM for different choices of χ_p. The microscopic contact angle is θ, the droplet height is h, the base radius of the droplet is r_B, the z-component of the average center-of-mass position is z_{CM}, and E is the root-mean-square error of the best-fit circle to the boundary profile data. h, r_B, z_{CM}, and E are in units of Å. 54

3.3 The wet and dry heights of the homogeneous monolayers. All values are given in units of Å. h_0 is the sum of the second and third terms in Eqn. 3.3 (i.e., $h_{W/D} = \langle z_{W/D} \rangle + h_0$). 55

3.4 Same as Table 3.2 except for seven runs on a phase separated SAM with small domains and $\chi_p = 0.5$. 63

3.5 Same as Table 3.2 except for seven runs on a phase separated SAM with large domains and $\chi_p = 0.5$. 64

3.6 A summary of the water contact angle on SAMs with the same overall composition but different degrees of mixing of the chains. [a]When the domain size is much larger than the droplet size the droplet is assumed to reside entirely on a hydrophilic domain. 67

3.7 The line tension, macroscopic and microscopic water contact angles, and the correlation coefficient for homogeneous monolayers. θ is taken as the value for the water droplet composed of 4000 molecules. 70

A.1 Bond lengths and valence angles. [a]water, [b]alcohol group, [c]ethoxylate group, [d]trisiloxane group, and [e]hydrocarbon. 157

A.2 Dihedral angle parameters for the surfactant molecules. [a]water, [b]alcohol group, [c]ethoxylate group, [d]trisiloxane group, and [e]hydrocarbon. 158

A.3 Lennard-Jones and Coulomb parameters for the surfactant molecules. [a]water, [b]alcohol group, [c]ethoxylate group, [d]trisiloxane group, [e]hydrocarbon, and [f]graphite. 159

List of Figures

1.1 (left) M(D′E_4OH)M and (right) $C_{12}E_4$ shown in all-trans configurations. In aqueous solution the hydrophilic groups of these molecules form a structure that resembles a helix. Methyl and methylene groups are shown as green/yellow, silicon is orange, oxygen is red, and hydrogen is white. 3

1.2 A small quantity of alkyl polyethoxylate/alcohol solution is added to a sessile water droplet on a hydrophobic solid. The aqueous surfactant solution is $C_{12}E_8$ at 7 times the CAC and $C_{12}E_0$ at 21 times the solubility limit. 4

1.3 Same as Fig. 1.2 except for a trisiloxane solution. The superspreading solution is >60 wt% methyl (propylhydroxide, ethoylated) bis(trimethylsiloxy) silane, 15 – 40 wt% polyethylene oxide monoallyl ether, ≤9 wt% polyethylene glycol at 20:1 water. 5

3.1 The profiles of three water drops of different size are shown on a chemically heterogeneous substrate composed of polar (p) and apolar (a) regions. 30

3.2 The orientation of each chain in the monolayer is described by a tilt angle (θ), a direction of tilt (χ), and a twist angle about the molecular axis (φ). This diagram is shown for a methyl-terminated chain with its eight atomic units. The x-direction corresponds to a nearest-neighbor (NN) direction. 36

3.3 The top image shows the top view of a region of a monolayer with methyl-terminated chains. The twist angles are indicated by color in the bottom image. The next-nearest neighbor (NNN) direction corresponds to $\chi = 30°$ in Fig. 3.2. 37

3.4 Atomic density profiles normal to the surface for two choices of χ_p. . 42

3.5 Percentage of gauche defects as a function of dihedral angle number for two choices of χ_p. The numbering scheme begins with angle 1 which involves the two fixed atoms. Note that the ordinate is interrupted. 44

3.6 Probability distribution function for the tilt angle for two choices of χ_p. 45

3.7 Probability distribution function for the direction of tilt for two choices of χ_p. Nearest-neighbor directions correspond to $\chi = 0°$ and $60°$ while the next-nearest neighbor direction corresponds to $\chi = 30°$. 45

3.8 Structural results for three fixed atoms: (a) Methyl and methylene density, (b) gauche defects, (c) tilt angle distribution and (d) direction of tilt distribution. 46

3.9 The normal component of the center-of-mass position of a water droplet on a homogeneous SAM as a function of time for different values of χ_p. The bottom layer of fixed atoms is located at $z = 0$. . . 48

3.10 The transverse components of the center-of-mass position of the droplet are shown for all time on a homogeneous monolayer: (a) $\chi_p = 0$, (b) $\chi_p = 0.25$, (c) $\chi_p = 0.5$, (d) $\chi_p = 0.75$, and (e) $\chi_p = 1$. The open circle in each plot indicates the final position of the droplet. 49

3.11 Side view of the final configuration of a water droplet composed of 4000 molecules on a homogeneous SAM for three choices of χ_p. The width of the simulation cell is roughly 50 Å larger than shown. The water molecules are shown with oxygen colored red and hydrogen in white, while the substrate is shown with methyl and methylene groups as gray, oxygen as orange, and hydrogen as white. 50

3.12 Top view of the final configuration of a water droplet composed of 4000 molecules on a homogeneous SAM with $\chi_p = 0.5$. The base area of the simulation cell is roughly twice as large as that shown. Same color scheme as Fig. 3.11. 52

3.13 The best-fit circle and liquid-vapor boundary profile data points are shown for a water nanodroplet on a homogeneous SAM with $\chi_p = 0.5$. The tangent line at the droplet edge is also shown. The height of the monolayer, h_W, is indicated by the horizontal line. The bottom layer of fixed atoms is located at $z = 0$. 55

3.14 Comparison of the wetting data between simulation and experiment. Error bars for the simulation data points are smaller than the size of the symbols. 56

3.15 The oxygen-oxygen radial distribution functions for three monolayers with different degrees of phase-separation and $\chi_p = 0.5$. 59

3.16 Same as Fig. 3.13 except for a phase-separated SAM with small domains. 60

3.17 Same as Fig. 3.12 except for a phase separated monolayer with small domains (Run 3 of Table 3.4). 61

3.18 Same as Fig. 3.12 except for a phase separated monolayer with large domains (Run 5 of Table 3.5). 62

3.19 Same as Fig. 3.13 except for a phase-separated SAM with large domains. 63

3.20 The transverse components of the center-of-mass position for all time on a phase separated monolayer with small domains and $\chi_p = 0.5$. The open circle in each plot indicates the final position of the droplet. The four representative runs from Table 3.4 are (a) Run 1, (b) Run 2, (c) Run 3, and (d) Run 6. 65

3.21 Same as Fig. 3.20 except for a phase separated monolayer with large domains. The four representative runs from Table 3.5 are (a) Run 1, (b) Run 2, (c) Run 3, and (d) Run 7. 65

3.22 Cosine of the water contact angle versus inverse base radius for two choices of χ_p. 70

4.1 Side view of a liquid drop on a wetting gradient with $\theta_a < \theta_r$, where θ_a and θ_r are the advancing and receding contact angles, respectively. On a surface where contact angle hysteresis is negligible a drop of any size will move in the direction of increasing γ_{SV}. 75

4.2 The orientation of each chain in the monolayer is described by a tilt angle (θ), a direction of tilt (χ), and a twist angle about the molecular axis (φ). This diagram shows a methyl-terminated chain with its eight atomic units. The x-direction corresponds to a nearest-neighbor (NN) direction. 85

4.3 A log-log plot of the axial component of the center-of-mass position versus time for a Lennard-Jones droplet on a wetting gradient. The coefficient and exponent of the power law fit are $c_{LJ} = 3.37\sigma\tau^{-0.42}$ and $n_{LJ} = 0.42$, respectively. 86

4.4 Side views of a Lennard-Jones droplet at different times on a wetting gradient. 87

4.5 The number density of hydroxyl groups as a function of position along the gradient is shown for the (a) non-uniform gradient and (b) uniform gradient. The line running through the data in both plots is the ideal or target gradient. 89

4.6 The axial component of the center-of-mass position is shown for two different size water droplets on the (a) non-uniform gradient and (b) uniform gradient. 89

4.7 Side views of the $N = 2000$ water nanodroplet at different times on a uniform wetting gradient. 91

4.8 The center-of-mass position versus time on a log-log plot for water droplets on a uniform wetting gradient with (a) $N = 2000$ and (b) $N = 4000$ molecules per drop. The lines are the power law fits to the data between 5 and 35 ns. 93

4.9 Best-fit ellipses to the liquid-vapor boundary profile data at (a) $t =$ 7.5 ns and (b) $t = 15.0$ for the $N = 2000$ water droplet on a uniform wetting gradient. 93

4.10 The base length of a cylindrical-cap water droplet on a uniform wetting gradient as a function of time. The lines are drawn to guide the eye. 95

4.11 Advancing and receding contact angles as a function of time for (a) $N = 2000$ and (b) $N = 4000$ water molecules per drop. The lines are drawn to guide the eye. 96

4.12 Advancing and receding contact angles as a function of position along the gradient for the (a) $N = 2000$ and (b) $N = 4000$ water molecule droplet. The angles were measured by fitting each time-averaged droplet profile to an ellipse. The data were calculated for the smaller droplet every 2 ns from 3 to 35 ns and for the larger droplet every 2 ns from 5 to 29 ns. $\theta_e(x)$ is given by the solid curve. 97

4.13 Droplet velocity as a function of position along the gradient as gotten by simulation and theory for (a) $N = 2000$ and (b) $N = 4000$ water molecules per drop. Edge effects are taken into account by only considering velocities on the intermediate region of the gradient. . . . 102

5.1 At $t = 0$, a spherical nanodroplet consisting of 9997 water molecules and 475 trisiloxane molecules is placed in the vicinity of a graphite substrate. 114

5.2 Cross-sectional view of the final configuration of the $M(D'E_4OH)M/H_2O$ droplet at 1.1 ns. 115

5.3 Same as Fig. 5.1 except for a $C_{12}E_4/H_2O$ droplet. 116

5.4 Cross-sectional view of the final configuration of the $C_{12}E_4/H_2O$ droplet at 1.3 ns. 117

5.5 Base radius versus time for the $M(D'E_4OH)M/H_2O$ and $C_{12}E_4/H_2O$ droplets. 118

5.6 Water density in the normal direction. 119

5.7 Number of hydrogen bonds per water molecule in the normal direction. 120

5.8 Contact angle versus time for five surfactant-laden droplets on graphite. The number of water molecules was 9997 in all cases. 122

5.9 Final configurations of cylindrical $M(D'E_4OH)M/H_2O$ (top) and $C_{12}E_4/H_2O$ (bottom) droplets on a self-assembled monolayer with $\chi_p = 0.25$. . . . 123

5.10 Center-of-mass position versus time for water and three surfactant-laden droplets. 124

6.1 Initial and final configurations of the $M(D'E_4OH)M/H_2O$ system on graphite. 133

6.2 Solid-liquid interface of the $M(D'E_4OH)M/H_2O$ solution at $t = 100$ ns with the graphite substrate removed. The white rectangle indicates the transverse area of the central simulation cell. Same coloring scheme as Fig. 6.1. 135

6.3 Positions of the central Si atoms in the yz-plane. Open/filled circles indicate that the hydrophilic moiety of the molecule extends from the bilayer in the positive/negative x-direction. The line through each circle indicates the orientation of the trisiloxane group. 136

6.4 Same as Fig. 6.1 except for a $C_{12}E_4/H_2O$ solution. 138

6.5 Solid-liquid interface for the $C_{12}E_4/H_2O$ solution at $t = 100$ ns with the graphite substrate removed. Same coloring scheme as Fig. 6.1. . . 139

6.6 The average y- and z-coordinates of the atoms composing the hydrocarbon chain for each $C_{12}E_4$ molecule are shown in the yz-plane. Open/filled circles indicate that the hydrophilic moiety of the molecule extends from the bilayer in the positive/negative x-direction. The top and bottom planes of fixed atoms are located at $z = 0$ and -3.41 Å, respectively. 141

6.7 Adsorption isotherms at 298.15 K for monolayers of $M(D'E_4OH)M$ and $C_{12}E_4$. 143

6.8 Side view of a M(D′E_4OH)M monolayer at 298.15 K with an inverse surface concentration of 57.2 Å^2/molecule. The central simulation cell, which is not completely shown in the vertical direction, is indicated by the white lines. Same coloring scheme as Fig. 6.1. 144

6.9 Same as Fig. 6.8 except the top view is shown. 145

6.10 Side view of a $C_{12}E_4$ monolayer at 298.15 K with an inverse surface concentration of 57.2 Å^2/molecule. The central simulation cell, which is not completely shown in the vertical direction, is indicated by the white lines. Same coloring scheme as Fig. 6.1. 147

6.11 Same as Fig. 6.10 except the top view is shown. 148

7.1 A wetting system with additional walls that are designed to promote the formation of a bilayer. 153

7.2 Cross-sectional view of a neat droplet of 500 M(D′E_4OH)M molecules at equilibrium on a methyl-terminated SAM at 450 K. The 2000 water molecules in the simulation are not shown. Same coloring scheme as Fig. 6.1. 154

7.3 Same as Fig. 7.2 except for a hydroxyl-terminated SAM. 154

Chapter 1

Introduction

1.1 Wetting Phenomena and Surfactants

When a small drop of water is placed on a clean glass surface the drop will spread spontaneously until it forms a film of monomolecular thickness. If a second drop of water is placed on a surface that has been coated with Teflon® (e.g., a non-stick cooking pan) a qualitatively different behavior is observed. Instead of wetting the surface the water drop is found to form a spherical cap with a well-defined contact angle. In the absence of contaminants the angle formed by water on a smooth Teflon® surface is 110°. The Young equation relates the interfacial tensions or surface energies to the contact angle:

$$\gamma_{SV} = \gamma \cos(\theta) + \gamma_{SL}, \tag{1.1}$$

where γ_{SV} is the solid-vapor surface energy, γ is the liquid-vapor surface energy, γ_{SL} is the solid-liquid surface energy, and θ is the macroscopic equilibrium contact angle.

There are many cases in industry where it is necessary for aqueous solutions to spread out on difficult-to-wet surfaces. One example from the agrochemical industry is the application of herbicides or pesticides to plant leaves [1]. These additives are dissolved in water and sprayed onto the leaves of plants. However, when the solution contacts the leaf's waxy coating it tends to bead-up and come away from the leaf. When this occurs the active ingredients are lost. Ideally, the solution would completely wet the surface of the leaf. Similar difficulties are encountered in the coating, painting, cosmetics, and printing industries.

The most common approach taken to deal with difficult-to-wet surfaces is the addition of surface-active agents or surfactants to the solution. Surfactants are molecules that consist of a nonpolar tail group and a polar head group capable of forming hydrogen bonds. Surfactants are classified as amphiphilc molecules because of their dual nature in that they are attracted to and repelled by water. A common nonionic surfactant is diethylene glycol monododecyl ether or $CH_3(CH_2)_{11}(OCH_2CH_2)_2OH$. When a monolayer of diethylene glycol monododecyl ether forms at the water-air interface the alkyl chains are found pointing into the vapor phase while the polar head groups interact with water.

Surfactants enhance the wetting of aqueous solutions on difficult-to-wet surfaces by adsorbing at the liquid-vapor and solid-liquid interfaces. This leads to a reduction in the interfacial tension of each interface. According to Eqn. 1.1, a decrease in γ and γ_{SL} corresponds to a decrease in the equilibrium contact angle (when θ is initially less than ninety degrees). The wetting of smooth solids by pure, simple liquids is fairly well understood [2]. However, when additives are present the situation becomes more complicated. Since most industrial wetting processes involve mixtures containing surfactant molecules more attention should be devoted to this area.

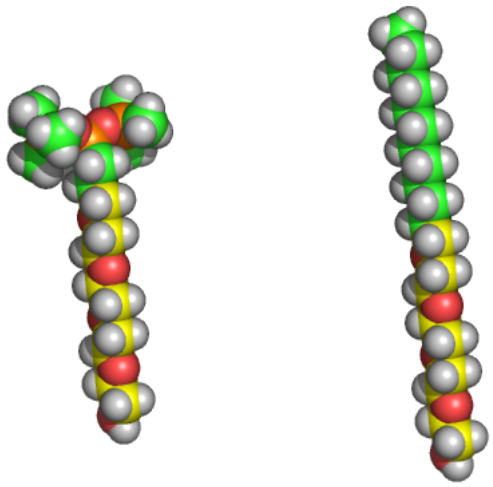

Figure 1.1: (left) M(D′E_4OH)M and (right) $C_{12}E_4$ shown in all-trans configurations. In aqueous solution the hydrophilic groups of these molecules form a structure that resembles a helix. Methyl and methylene groups are shown as green/yellow, silicon is orange, oxygen is red, and hydrogen is white.

Diethylene glycol monododecyl ether is an example of an alkyl polyethoxylate surfactant. The chemical formula for the alkyl polyethoxylate surfactants in shorthand notation is C_mE_n, where C_m is $CH_3(CH_2)_{m-1}-$, E_n is $-(OCH_2CH_2)_nOR$, and R is typically $-H$, $-CH_3$, or $-CH_2CO_2H$. A $C_{12}E_4$ molecule is shown in Fig. 1.1. A trisiloxane superspreading surfactant is also shown in Fig. 1.1. The shorthand notation for these surfactants is M(D′E_n)M, where M is $(CH_3)_3SiO-$ and D′ is $(CH_3)Si(CH_2)_3-$. The hydrophobe of these surfactants is a methyl-terminated trisiloxane group, MD′M. The trisiloxanes are referred to as superspreaders because they promote the rapid and complete wetting of aqueous drops on difficult-to-wet (hydrocarbon) substrates. The choice of the terminal group, R, is often written explicitly as in M(D′E_4OH)M.

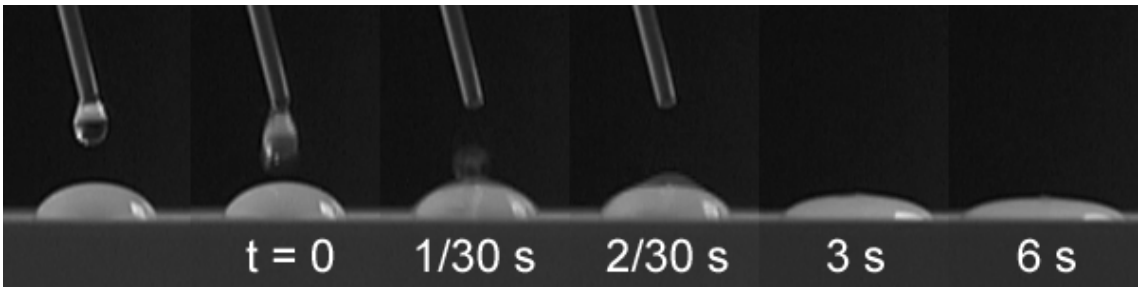

Figure 1.2: A small quantity of alkyl polyethoxylate/alcohol solution is added to a sessile water droplet on a hydrophobic solid. The aqueous surfactant solution is $C_{12}E_8$ at 7 times the CAC and $C_{12}E_0$ at 21 times the solubility limit.

1.2 Superspreading

To illustrate the superior properties of the trisiloxane surfactants we first consider adding a small amount of a dilute polyethoxylate solution to a pure water drop which is on a moderately hydrophobic surface (Fig. 1.2). At $t = 0$, the droplet subtends a contact angle of roughly ninety degrees. A small quantity of conventional surfactant solution is added and the behavior of the drop is followed. The drop is seen to spread during the first few seconds of the experiment. Beyond $t = 6$ s, the shape of the drop does not change appreciably. The final contact angle of the drop is tens of degrees lower than the initial value but complete wetting was not observed.

A discrepant event is seen when a small amount of superspreading solution is added to the pure drop (Fig. 1.3). The trisiloxane solution causes the drop to completely wet the substrate in less than a second.

While superspreading was first observed in the 1960's [3], its mechanism is still not understood. It has proven difficult to explain why the trisiloxane surfactants promote the rapid and complete wetting of aqueous drops on highly hydrophobic substrates while all other surfactants do not.

An early study by Ananthapadmanabhan et al. [4] considered three silicone sur-

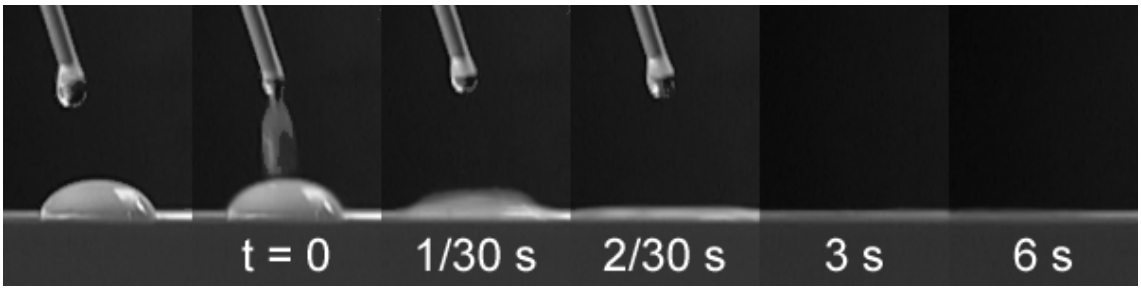

Figure 1.3: Same as Fig. 1.2 except for a trisiloxane solution. The superspreading solution is >60 wt% methyl (propylhydroxide, ethoylated) bis(trimethylsiloxy) silane, 15 – 40 wt% polyethylene oxide monoallyl ether, ≤9 wt% polyethylene glycol at 20:1 water.

factants including $M(D'E_8OCH_3)M$. The trisiloxane surfactant gave the best wetting results. Aqueous drops of $M(D'E_8OCH_3)M$ exhibited superspreading on Parafilm® at 5 – 10 times the critical aggregation concentration (CAC) of the solution. The authors speculated that superspreading was due to the ability of the trisiloxane surfactant molecules to reduce the liquid-air surface tension to low values (∼20.5 mN/m), a high affinity of the surfactants for low energy substrates, fast adsorption kinetics at the liquid-vapor and solid-liquid interfaces, and a favorable molecular orientation at the spreading edge.

Zhu et al. [5] investigated the wetting of six silicone surfactants on Parafilm® and found that the four that gave a dispersed surfactant-rich phase were the ones that exhibited superspreading. The wetted area of the drops was found to increase linearly with time suggesting a Marangoni-driven flow. The initial rate of spreading increased with decreasing particle size. Furthermore, in a dry atmosphere the solutions did not superspread. Based on this the authors speculated that a thin, high tension film may be present at the leading edge of the drop. Such a film would support the hypothesis that superspreading is largely driven by the Marangoni effect. The origin of the water film is unknown and its stability on a surface as

hydrophobic as Parafilm® is questionable. Of the various linear and hammer-like alkyl polyethoxylate surfactants considered none were shown to be superspreaders.

A number of studies have explored the link between superspreading and surfactant phase behavior. Gradzielski et al. [6] examined the aqueous phase behavior of various siloxane surfactants. Scriven and Davis and coworkers investigated the phase behavior of $M(D'E_nOH)M/H_2O$ for n = 5, 8, 12, and 18 using a variety of experimental techniques [7]. For the same value of n, the phase behavior between the trisiloxanes and the alkyl polyethoxylates was found to be similar. Hill et al. [8] studied the aqueous phase behavior of $M(D'E_8OH)M$, $M(D'E_8OCH_3)M$, and $M(D'E_8OAc)M$. The terminal group was found to be important. At low concentrations the surfactants were found to form unilamellar and multilamellar vesicles. A linear surfactant with a trisiloxane hydrophobe ($MDM'E_8OH$, where D is $-OSi(CH_3)_2-$ and M′ is $-OSi(CH_3)_2(CH_2)_3-$) was shown to superspread at 0.1 wt% on Parafilm®. This provides further evidence that the hammer-like geometry does not uniquely explain superspreading.

Wagner et al. [9] determined phase transition temperatures for $M(D'E_nOCH_3)M/H_2O$ for $n = 5 - 9$ and a commercial superspreading solution at concentrations of 1 and 5 wt%. Li et al. [10, 11] produced phase diagrams for $M(D'E_6OH)M/H_2O$ and $M(D'E_{10}OH)M/H_2O$. Ternary mixtures have also been studied [12, 13, 14]. More on the subject of surfactant phase behavior may be found in Chapter 6.

Stoebe et al. [15, 16] investigated the wetting of $M(D'E_nOR)M$ and C_mE_n surfactant solutions on SAMs of varying surface energy. The self-assembled monolayers were composed of $CH_3(CH_2)_{11}SH$ and $HOCH_2(CH_2)_{11}SH$ on Au(111). While the trisiloxanes were shown once again to be the only surfactants to cause complete wetting of aqueous drops on highly hydrophobic substrates, on moderately hydrophobic

substrates the two surfactant classes showed similar behavior. The authors referred to this phenomena as surfactant-enhanced spreading. The spreading rate was found to go through a maximum as a function of both concentration and substrate surface energy. And the initial wetted area was directly proportional to time. An aqueous $M(D'E_8OH)M$ drop at a concentration of 0.6 wt% on a substrate with a water contact angle of 66° gave a spreading rate of 90 mm^2/s. Similarly, an aqueous $C_{12}E_3$ drop at a concentration of 0.2 wt% on a substrate with a water contact angle of 53° gave a spreading rate of 85 mm^2/s. These are the maximum values reported for the two classes. On Parafilm® the trisiloxane solution gave a spreading rate of 7 mm^2/s while the $C_{12}E_3$ solution did not spread at all. Humidity was shown to be less important as suggested by Ref. [5]. Ionic surfactants were also found to exhibit the characteristics of surfactant-enhanced spreading [17]. Liquid substrates have been considered [18, 19]. And spreading rates for trisiloxane solutions have been measured using a quartz crystal microbalance [20].

Wagner et al. [21] investigated the spreading rate of trisiloxane surfactants on low energy surfaces as a function of temperature. At room temperature, the trisiloxane with six ethoxylate groups was found to spread the fastest. At 40 °C, $M(D'E_8OCH_3)M$ and a commercial superwetting agent were found to prevail.

Svitova et al. [22] measured the contact angle of aqueous droplets of $M(D'E_nOCH_3)M$ for $n = 6$, 8, and 12 on highly hydrophobic surfaces at concentrations below the CAC. The structures formed by $M(D'E_6OH)M$, $M(D'E_8OH)M$, and $C_{12}E_3$ were studied on graphite using AFM [23]. At low concentrations the alkyl polyethoxylate surfactant was found to form a striped pattern. Multilayer structures were found at the critical wetting transition. For substrates of varying surface energy, Grant et al. [24] have studied the adsorption of C_mE_n surfactants while Dong et al. [25]

have investigated M(D′E_nOH)M for $n = 6$, 8, and 12. Similar structures are found between the two classes for similar values of n.

Svitova et al. [26] measured the dynamic surface tension of trisiloxane and alkyl polyethoxylate surfactants at high concentrations using the drop volume method. Solutions containing vesicles were found to reduce the surface tension faster than micellar solutions. Wetting studies on a liquid hydrocarbon surface were also conducted. Gentle et al. [27] determined the equilibrium surface tension below the CAC for M(D′E_nOH)M for $n = 4 - 16$. They found the surface adsorption to be the same for $n < 16$ implying that the maximum packing concentration is determined by the hydrophobe over this range.

The wetting behavior of neat trisiloxane and alkyl polyethoxylate droplets on hydrophobic and hydrophilic surfaces have been studied using ellipsometry [28, 29]. Cazabat and Tiberg and coworkers found that trisiloxane droplets form reverse bilayers on low energy substrates and wedge or sand pile-shaped precursor films on high energy substrates. Each precursor film was found to be autophobic. The alkyl polyethoxylate surfactants did not spread and humidity was found to play a role in determining the spreading rate. Ruckenstein suggests that the formation of the bilayer on the hydrophobic surface is driven by short-range attractive forces between the hydrophobe of the surfactant and the substrate [30].

Churaev et al. [31] found good agreement between experimental data and their hydrodynamic calculations when the disjoining pressure was included. The authors suggest that thick wetting films, which are stabilized by vesicles and electrostatic forces, are the equilibrium shapes formed by aqueous trisiloxane droplets. Evidence was found for a bilayer structure in the thinner of the two concentric films found. Churaev et al. [31] demonstrated the removal of silicone oils from hydrophobic

surfaces using aqueous solutions of $M(D'E_8)M$.

Nikilov et al. [32] propose that superspreading is due to an enhanced Marangoni effect. Their molecular simulation results for a single $M(D'E_8OCH_3)M$ molecule at the water-air interface are questionable because the polyethoxylate chain is in an all-trans conformation instead of a structure resembling a helix. Rafaï and Bonn and coworkers [33, 34] have also proposed that the Marangoni effect is the driving force behind superspreading.

Kumar et al. [35] measured the rate of adsorption of trisiloxane surfactants ($M(D'E_nOH)M$ for $n = 4$, 8, and 12) at the liquid-vapor interface for bulk concentrations below the CAC. The authors concluded that the adsorption rates were not large enough to maintain the high surface concentrations necessary for superspreading. The direct adsorption of molecular aggregates instead of monomer may supply the interfaces with the needed surfactant. Kumar et al. [36] used infrared spectroscopy to infer the arrangement $M(D'E_8OH)M$ and $C_{12}E_8$ molecules at the surface of a methyl-terminated alkylsilane SAM. The trisiloxane surfactant was shown to be more effective at removing water from this interface and its cylindrical shape was cited as the dominant reason. Solutions above and below the CAC were considered.

1.3 Computational Wetting Studies

Blake et al. [37] examined the dynamics of a spreading drop on an atomic surface. All nonbonded interactions were of the Lennard-Jones type. The solvent consisted of up to sixteen atoms per molecule. The contact angle and base area were computed as a function of time.

Hautman and Klein [38] were among the first to use molecular simulation to

study the wetting of self-assembled monolayers by water. In their study the substrate consisted of an alkylthiol monolayer with either methyl or hydroxyl termination. For the methyl-terminated monolayer the water contact angles was found to be 135°. Only 90 SPC water molecules were used in the study. On the polar monolayer the water contact angle was 5 – 17° depending on the initial configuration of the water molecules. Striking agreement was seen between the microscopic contact angles gotten by simulation and the experimental macroscopic contact angles.

The interaction of water with carbon nanotubes (CNT) is an active area of research. An related problem is the wetting of graphite by water. Lundgren et al. [39] have investigated the wetting of a single layer of hexagonal graphite by water at room temperature using molecular dynamics simulation. Using 900 TIP-3P water molecules the authors found that the water drop formed a microscopic contact angle of 83°. A range of values have been cited for the experimental macroscopic contact angle of water on graphite [40]. Equilibrium configurations were shown to be independent of the initial configuration. When small amounts of ethanol were added to the drop the contact angle was found to decrease by up to tens of degrees. The alcohol was found to preferentially adsorb at the liquid-vapor and solid-liquid interfaces. A solution of 30 wt% ethanol was shown to give a 30° decrease in the contact angle, which is consistent with experimental findings. This is one of the first computational studies to explore the effect of additives on wetting.

A second work on the wetting of graphite by water determined the Lennard-Jones parameters for the carbon-oxygen interaction that reproduces the experimental contact angle. Werder et al. [40] showed that previous parameters used to described CNT-water interactions give drastically different behavior when applied to the water-graphite system. The behavior ranged from non-wetting to complete

wetting. The authors considered drops consisting of 1000 to 17,576 SPC/E water molecules on a double layer of graphite. The initial configuration of the droplet, motion of the lattice, and spherical truncation radius of the intermolecular potential were all shown to have no significant influence on the binding energy, base radius, or microscopic contact angle.

Fan and Cagin [41] investigated the wetting properties of crystalline polymer surfaces by water and methylene iodide. The simulations were limited to small systems of 216 water molecules since all interactions were computed directly. The substrates were modeled as the (001) faces of polyethylene, poly(tetrafluoroethylene), and poly(ethylene terephthalate). Microscopic contact angles were found to be higher than experimental measurements. The authors suggested that the trend came about as a result of using crystalline surfaces as opposed to amorphous surfaces, which were used in making the experimental measurements. It was also suggested that the disagreement may have resulted by their choice to keep the lattice atoms fixed in space. The free energy of each substrate was determined by using the Owens-Wendt equation.

The wetting behavior of water droplets on superhydrophobic surfaces has been examined at the nanoscale [42]. Lundgren et al. studied the contact angle formed by drops consisting of 1100 TIP-3P water molecules on a pillared surface. The pillars were modeled as finite, stacked layers of graphite. The square cross-section of each pillar had a side of 12 Å and the height was varied from 3.4 to 61.4 Å.

Mar et al. [43] examined the behavior of a sessile drop consisting of 80 hexadecane molecules on a methyl-terminated alkylthiol monolayer. The authors found a contact angle of $60\pm6^\circ$, which is 20% larger than the macroscopic value. Equilibrium averages were found to be independent of initial configuration. The purpose of the

study was to determine whether or not solvent molecules penetrated the monolayer. The simulation showed negligible penetration.

Much can be learned about the wetting of solid substrates by aqueous surfactant solutions by examining bulk solutions. Bandyopadhyay et al. [44] have conducted simulations of the L_α phase of $C_{12}E_2/H_2O$. The workers found an interlamellar spacing that agreed well with the experimental value. The interfacial area per surfactant molecule was also reproduced by the simulation. Examination of the surfactant head group structure revealed that OCCO dihedral angles were more likely to be found in a gauche conformation than CCOC angles. This effect is caused by water molecules forming hydrogen bonds with pairs of oxygen atoms in the glycol chain. The isothermal-isobaric simulation used 512 SPC/E water molecules and 64 surfactant molecules.

Kong et al. investigated the stability of surfactant bilayer systems using Monte Carlo simulations. In the first of two papers, the authors used 286 SPC water molecules to compute density profiles and radial distribution functions for the $C_{12}E_2/H_2O$ system [45]. The surfactant tail groups were modeled as a uniform continuum with an average density. At room temperature, water molecules were found to form hydrogen-bonded bridge structures with the oxygen atoms of the head group. This phenomena shifts the dihedral angle distribution to favor gauche OCCO angles. When the temperature was raised to 90 °C, thermal motion prevented the formation of these bridging structures and the surfactant tail was found to bend sharply and interact with the wall. A second paper considered $C_{12}E_3$ [46]. Similar structuring was seen around the surfactant tail group. The longer surfactant chain was found to have greater rotational freedom.

Kuhn et al. [47] have probed the tilt angles and structural properties of a $C_{12}E_5$

monolayer adsorbed at the air-water interface. The authors report good agreement with experimental data. They found the hydrocarbon tails to form a 43° angle while the surfactant head group formed an 11° angle with the air-water interface. The angular distribution function revealed that 64% of the dihedral bonds in the alkyl chain were trans. The OCCO dihedral angles were 21% gauche compared to 2% for the CCOC angles. The head groups were found to be responsible for anchoring the chain, which was evidenced by the low mean squared displacement. Short- and long-range interactions were computed using the minimum image convention with a spherical truncation radius of 10 Å. The study used 36 surfactant molecules and 1575 SPC water molecules. The temperature was maintained at 298 K using constant-kinetic energy velocity-rescaling.

Shen et al. [48] studied the spreading of surfactant solutions on hydrophobic substrates. All nonbonded interactions were of the Lennard-Jones type. The authors compared a linear eight-atom chain which was held together by a FENE interaction with a T-shaped molecule whose structure was maintained by using bond length and valence angle potentials. Lattice motion was allowed. The investigation revealed that the T-shaped structure gave a larger wetted area than the linear chain for the first set of interaction coefficients. The extent of spreading was found to be similar between the two systems for the second set where the interaction between the solvent and solvophilic groups was reduced. The adsorption isotherms for the linear surfactants are known [49, 50].

Recently, Kim et al. [51] investigated the spreading of Lennard-Jones droplets containing linear surfactants. The authors found that the spreading rate was strongly influenced by the strength of the interaction between the tail group of the surfactant and the substrate. The substrate was modeled as a featureless solid.

Chapter 2

Methodology

Isaac Newton is largely responsible for developing the mathematical equations that are used today to describe the motion of classical bodies. Newton's equations of motion provide an excellent description of the motion of planets, apples, and even grains of sand. In fact, the same laws can be applied with good accuracy to the $O(10^{23})$ atoms that make up of a single grain of sand.

In this chapter we present the molecular dynamics simulation methodology that was used in this work. The chapter begins with Newton's second law of motion written for a system of molecules interacting through intermolecular potential functions. In Section 2.2, the interaction potential functions are specified. The procedure for constant-temperature simulations is discussed in Section 2.3. Next, constraint dynamics routines are considered. This is followed by the derivation of the atom evolution equation for a rigid molecule in Section 2.5. The chapter concludes with a description of parallel molecular dynamics simulations.

2.1 Classical Dynamics

In this work, atoms are modeled as point masses and electron distributions as discrete point charges. Molecules interact through site-site potential energy functions. The motion of a point mass in such a system is governed by Newton's second law of motion:

$$m_i \frac{d^2 \boldsymbol{r}_i}{dt^2} = -\frac{\partial}{\partial \boldsymbol{r}_i} U(\boldsymbol{r}_1, \boldsymbol{r}_2, ..., \boldsymbol{r}_N), \tag{2.1}$$

where m_i is the mass assigned to the site, $\boldsymbol{r}_i$ is the position vector, t is time, and U is the total potential energy of the system.

All nonbonded interactions are pairwise additive and take place between interaction sites on the various molecules. Because three- and higher-body interactions are neglected, it is necessary to make the two-body potential, U_2, an effective pair potential. The parameters for each potential function come from experimental data or *ab initio* calculations. The configurational energy for a system of N interacting atoms may be written as:

$$U(\{\boldsymbol{r}_N\}) = \sum_i \sum_{j \neq i} U_2(r_{ij}) + \sum U_3(\theta_{ijk}) + \sum U_4(\phi_{ijkl}) + \sum_i U_{ext}(r_i). \tag{2.2}$$

The first term in Eqn. 2.2 is a sum over all atom pairs once, the second term accounts for the valence angle energy, and the third term is the dihedral angle potential energy. One-body interactions are given by U_{ext}. The various intermolecular and intramolecular potential functions are given specific forms in Section 2.2.

2.2 Intermolecular Potential Functions

The potential energy between two point charges q_i and q_j separated by a distance r_{ij} in vacuum is

$$U^{(e)}(r_{ij}) = \frac{1}{4\pi\epsilon_0}\frac{q_i q_j}{r_{ij}}, \tag{2.3}$$

where $\epsilon_0 = 8.85 \times 10^{-12}$ F/m is the permittivity constant. This is the Coulomb potential and it is a long-range interaction.

From perturbation theory it is known that the asymptotic form of an intermolecular potential is $U(r) \sim -cr^{-6}$. Combining this result with the fact that atoms repel one another at short separations leads to the Lennard-Jones potential:

$$U^{(lj)}(r_{ij}) = 4\epsilon_{ij}\left[\left(\frac{\sigma_{ij}}{r_{ij}}\right)^{12} - \left(\frac{\sigma_{ij}}{r_{ij}}\right)^{6}\right], \tag{2.4}$$

where ϵ_{ij} and σ_{ij} set the energy and length scales, respectively. The exponent for the repulsive term is taken for historical reasons. Eqn. 2.4 is an empirical potential that accurately describes the interaction between spherical, neutral, polarizable atoms like the noble gases.

The potential energy of a valence angle is assumed to follow a simple harmonic potential:

$$U^{(v)}(\theta_{ijk}) = \frac{k}{2}(\theta_{ijk} - \theta_0)^2. \tag{2.5}$$

In Eqn. 2.5, k is a constant and θ_0 is the equilibrium valence angle.

The dihedral angle potential function is given below:

$$U^{(d)}(\phi_{ijkl}) = c_1[1 + \cos(\phi_{ijkl})] + c_2[1 - \cos(2\phi_{ijkl})] + c_3[1 + \cos(3\phi_{ijkl})], \qquad (2.6)$$

where c_1, c_2, and c_3 are constants and ϕ_{ijkl} is the dihedral angle formed by atoms i, j, k, and l.

The interaction potential between a Lennard-Jones atom and a semi-infinite, continous Lennard-Jones solid of uniform density ρ_S is given by

$$U^{(e)}(z_i) = \frac{2}{3}\pi\rho_S\epsilon_{iS}\left(\frac{2\sigma_{iS}^{12}}{15(z_i - z_0)^9} - \frac{\sigma_{iS}^6}{(z_i - z_0)^3}\right). \qquad (2.7)$$

In Eqn. 2.7, $z_i - z_0$ is the distance between the particle and solid surface and σ_{iS} and ϵ_{iS} are given by Eqns. 2.8. Potential functions like Eqn. 2.7 have been derived for various lattice structures [52].

When two different Lennard-Jones species interact the Lorentz-Berthelot combining rules are used:

$$\begin{aligned} \sigma_{ij} &= (\sigma_i + \sigma_j)/2, \\ \epsilon_{ij} &= \sqrt{\epsilon_i \epsilon_j}. \end{aligned} \qquad (2.8)$$

2.3 Constant-Temperature Simulations

Temperature is defined through the energy equipartition principle. For a system of particles or atoms the temperature is given by

$$T = \frac{1}{(3N - N_c)k}\left\langle \sum_{i=1}^{N} \frac{p_i^2}{m_i} \right\rangle, \qquad (2.9)$$

where N is the number of atoms, k is Boltzmann's constant, and $\langle\ \rangle$ indicates an ensemble average. In Eqn. 2.9, N_c is the number of internal molecular constraints plus global ensemble constraints. Since most benchtop experiments are carried out at constant temperature it is important to be able to conduct simulations isothermally. During the 1980's, several methods were developed to allow for constant-temperature molecular dynamics simulations [53].

The simplest method to constrain the temperature is constant-kinetic energy velocity-rescaling. At the end of each integration time step the velocity of every atom in the system is rescaled by $\sqrt{T/\mathcal{T}}$, where T is the desired temperature and $\mathcal{T}$ is the instantaneous temperature. This crude method gives discontinuous dynamics and should not be used during the production phase of a simulation. A simple algorithm for isothermal and/or isobaric simulations has been put forth by Berendsen et al. [54]. While the method is commonly used is does not generate states in the canonical ensemble. A Gaussian thermostat is an attractive option for the simulation of molecules. Because the method constrains the kinetic energy to a constant, the equilibrium distribution function is canonical in coordinate space, but only of delta-function form in momentum space.

The Nosé-Hoover thermostat is used in this work [55]. A statistical mechanical ensemble of constant number of particles, volume, and temperature corresponds to solving the following equations of motion:

$$\begin{aligned} \dot{\boldsymbol{r}}_i &= \boldsymbol{p}_i/m_i \\ m_i\frac{d^2\boldsymbol{r}_i}{dt^2} &= \boldsymbol{f}_i - \eta(\boldsymbol{r}_i,\boldsymbol{p}_i)\dot{\boldsymbol{r}}_i. \end{aligned} \tag{2.10}$$

According to the Nosé-Hoover method the time evolution of the friction coefficient

η is given by:

$$\frac{d\eta}{dt} = \frac{1}{Q}\left(\sum_i \frac{p_i^2}{m_i} - gkT\right). \tag{2.11}$$

The solution of Eqns. 2.10 through 2.11 generate states in the canonical ensemble with the correct probability distribution function in both position and momentum space. In Eqn. 2.11, $Q = gkT\tau^2$ where g is the total number of degrees of freedom, k is Boltzmann's constant, T is the absolute thermodynamic temperature, and τ is the relaxation time of the heat bath.

The Nosé-Hoover thermostat may be understood intuitively. The additional force in Eqn. 2.10 acts like a velocity-dependent drag force. When the instantaneous kinetic energy is greater than the average kinetic energy, according to Eqn. 2.11, η will increase and eventually become positive. When this occurs the additional force in Eqn. 2.10 causes each particle to decelerate bringing the system toward the preset temperature. The system temperature is also driven toward to the preset temperature if the instantaneous kinetic energy is less than the average energy. The temperature is found to oscillate with time for a system using the Nosé-Hoover thermostat. The period of oscillation is controlled by τ. A typical choice of τ is $O(\Delta t)$. For this work, our implementation of the thermostat was validated by showing excellent agreement between the computed kinetic energy distribution of the molecules and the theoretical distribution.

2.4 Atomic Systems with Molecular Constraints

Bond stretching and bond bending potentials may be used to describe the internal motion of molecules. Since this motion takes places on small time scales, molecules

are often times treated as rigid to allow for a larger integration time step. Also, the force field parameterization becomes simpler since only the value of the constrained length or angle is needed instead of a potential function and potential parameters. Evidence suggest that it is reasonable to fix bond lengths and valence bond angles, but dihedral angles should be allowed to vary freely under the influence of a periodic intramolecular potential function such as Eqn. 2.6.

There are two common approaches to simulating the motion of a system of molecules subject to internal constraints. The first method is to use quaternions or Euler angles to solve the translational and rotational equations of motion. The second and most popular method uses a two-step procedure to satisfy the constraints while evolving the system.

Ryckaert et al. [56] proposed a procedure where in the first step the position of each atom is evolved ignoring the constraints. In the second step the atom positions are corrected by iteratively solving a set simplified constraint equations using the method of Lagrange multipliers (see Section 2.5). The so-called SHAKE algorithm is straightforward to implement and more efficient than quaternion techniques.

Several workers have improved on the original method of Ref. [56]. The RATTLE procedure introduced by Andersen [57] satisfies the constraint equations to within round-off error in addition to the time derivatives of the constraints. The method is of a higher precision than SHAKE and it is easier to combine with constant temperature or constant pressure algorithms. Allen and Tildesley [53] provide SHAKE, RATTLE, and other constraint dynamics routines written in the FORTRAN programming language in their online code library.

Schemes have been developed that avoid linearizing and decoupling the constraint equations. Krautler et al. [58] have put forth M-SHAKE which is a con-

straints dynamics routine that solves the linearized by not decoupled constraint equations by matrix inversion. The method is shown to be more effective than SHAKE for water and other small solvent molecules. An appealing alternative to the aforementioned algorithms for water or other triangular molecules is SETTLE [59]. SETTLE is an analytical version of RATTLE. SETTLE is reported to be faster and of higher accuracy than RATTLE for reasonable tolerances.

In Section 2.5, a particle evolution equation is derived for an atom subject to intermolecular and intramolecular forces, constraint forces, and a thermostat.

2.5 Atom Evolution Equation

The dynamical behavior of a system of interacting molecules is governed by Newton's equations of motion. When these equations are combined with initial positions, initial velocities, and boundary conditions the problem becomes mathematically deterministic. This system of second-order nonlinear differential equations does not permit an analytical solution. Molecular dynamics is the numerical solution to Newton's equations of motion for system of interacting molecules in 3-dimensions. In this section we derive an atom evolution equation.

Newton's second law of motion for a particle subject to external forces, constraint forces, and a thermostat is

$$m_i \ddot{\boldsymbol{r}}_i = \boldsymbol{f}_i - \eta \dot{\boldsymbol{r}}_i + \boldsymbol{g}_i, \tag{2.12}$$

where $\boldsymbol{f}_i$ is the total force on atom i due to nonbonded and intramolecular interactions, η is an effective friction coefficient, and $\boldsymbol{g}_i$ is the total force on atom i due to

constraint forces. The constraint forces may be written as

$$\boldsymbol{g}_i = -\sum_j \lambda_{ij} \frac{\partial}{\partial \boldsymbol{r}_i} \sigma_{ij}. \tag{2.13}$$

In Eqn. 2.13, the sum is taken over all atoms that atom i is involved in a constraint with, λ_{ij} a Lagrange multiplier, and the constraint, σ_{ij}, is $r_{ij}^2 - d_{ij}^2 = 0$, where d_{ij} is the value of the constrained bond length. These equations cannot be solved exactly. Instead, an approximation is made for the constraint force:

$$m_i \ddot{\boldsymbol{r}}_i \approx \boldsymbol{f}_i - \eta \dot{\boldsymbol{r}}_i + \boldsymbol{g}_i^{(r)}. \tag{2.14}$$

The RATTLE procedure ignores the constraint forces during the first or unconstrained step. The unconstrained position at $t + \Delta t$ is

$$\boldsymbol{r}_i'(t + \Delta t) = \boldsymbol{r}_i(t) + \boldsymbol{v}_i(t)\Delta t + \frac{1}{2}\Delta t^2 [\boldsymbol{f}_i(t)/m_i - \eta(t)\boldsymbol{v}_i(t)]. \tag{2.15}$$

And the velocity at the half step is given by

$$\boldsymbol{v}_i'(t + \Delta t/2) = \boldsymbol{v}_i(t) + \frac{1}{2}\Delta t [\boldsymbol{f}_i(t)/m_i - \eta(t)\boldsymbol{v}_i(t)]. \tag{2.16}$$

The friction coefficient may then be updated,

$$\eta(t + \Delta t/2) = \eta(t) + \frac{\Delta t}{2Q}\left(\sum \frac{p_i^2(t)}{m_i} - gkT \right). \tag{2.17}$$

Using an iterative procedure, the Lagrange multipliers λ_{ij} are determined. The

position of each atom and the velocity at the half step are then corrected:

$$\begin{aligned} \boldsymbol{r}_i(t+\Delta t) &= \boldsymbol{r}'_i(t+\Delta t) + \frac{\Delta t^2}{2m_i}\boldsymbol{g}_i^{(r)}(t) \\ \boldsymbol{v}_i(t+\Delta t/2) &= \boldsymbol{v}'_i(t+\Delta t/2) + \frac{\Delta t}{2m_i}\boldsymbol{g}_i^{(r)}(t). \end{aligned} \tag{2.18}$$

Note that the constraining forces act along the bond vectors $\boldsymbol{r}_{ij}(t)$. The friction coefficient may then be updated,

$$\eta(t+\Delta t) = \eta(t+\Delta t/2) + \frac{\Delta t}{2Q}\left(\sum \frac{p_i^2(t+\Delta t/2)}{m_i} - gkT\right). \tag{2.19}$$

The forces using the updated positions, $\boldsymbol{r}_i(t+\Delta t)$, are then calculated. The RATTLE procedure is complete by updating the velocities using $\boldsymbol{f}(t+\Delta t)$. The details of the method can be found [57]. The unconstrained velocity is

$$\boldsymbol{v}'_i(t+\Delta t) = \frac{2}{2+\eta(t+\Delta t)\Delta t}\left[\boldsymbol{v}_i(t+\Delta t/2) - \Delta t\frac{\boldsymbol{f}_i(t+\Delta t)}{2m_i}\right] \tag{2.20}$$

The velocity is then corrected as

$$\boldsymbol{v}_i(t+\Delta t) = \boldsymbol{v}'_i(t+\Delta t) + \frac{\Delta t}{2m_i}\boldsymbol{g}_i^{(v)}(t+\Delta t) \tag{2.21}$$

The velocity is corrected by the constraint forces which act along $\boldsymbol{r}_{ij}(t+\Delta t)$. This ensures that the time derivative of the bond length constraint also satisfied (i.e., $\boldsymbol{r}_{ij}\cdot\boldsymbol{v}_{ij}=0$).

2.6 Parallel Simulations

Computer power has increased dramatically over the last two decades. Despite this fact, the computational demands of molecular simulation are still not met by standard computer workstations. Efficient simulation techniques have been developed to reduce computer code execution times.

The computational complexity of the direct force calculation of a system of N particles is $O(N^2)$. For certain systems, techniques are available to reduce the complexity to $O(N)$. Interactions that decay faster than $1/r^d$, where d is the number of spatial dimensions are short-range interactions. In this case, for simulations of $O(10^2)$ particles a Verlet list may be used to reduce the compute code execution time [53]. When the number of particles reaches $O(10^3)$ the cell method becomes more efficient. The cell method is advantageous for larger systems because neighbors are found by searching over a sub-domain. If Newton's third law of motion is utilized then the amount of computation is $O(27Np/2)$, where p is dependent on the grid resolution. Grest et al. [60] have devised a method that combines the Verlet list and cell method to greatly reduce execution time for large systems with short-range interactions.

To improve execution times beyond the method proposed by Grest et al. [60] parallel processing may be used. Several standard methods to parallelize a molecular dynamics code exist [61]. The spatial decomposition (SD) method assigns particles to computer processors based on particle position. A second technique, particle decompositions (PD), assigns each particle to same computer processor for the duration of the simulation. The PD method has better load balance than the SD method especially for inhomogeneous systems such as sessile drop computer exper-

iments. Less communication is required by the SD approach in comparison to the particle decomposition technique.

Chapter 3

Wetting Behavior of Nanodroplets of Water on Homogeneous and Phase Separated Self-Assembled Monolayers

The wetting behavior of nanodroplets of water on homogeneous and phase separated self-assembled monolayers (SAMs) composed of $CH_3(CH_2)_{10}SH$ and $HOCH_2(CH_2)_{10}SH$ on Au(111) is studied using molecular dynamics simulations. An efficient model is introduced for the SAM where only the top eight or ten atomic layers are considered. For the homogeneous monolayers the CH_3- and $HOCH_2$-terminated chains are uniformly mixed. With χ_p denoting the mole fraction of $HOCH_2$-terminated chains, we report the equilibrium contact angles of water droplets consisting of 4000 molecules on homogeneous monolayers for $\chi_p = 0$, 0.25, 0.5, 0.75, and 1. Good agreement is seen between the simulation results and experimental data. For $\chi_p = 0.5$, the

contact angle and base diameter of the droplet are found to be $51.9 \pm 1.3^\circ$ and 10.2 ± 0.2 nm, respectively. Large deviations from the Cassie model are observed. For the monolayers with $\chi_p = 0$ and 0.25, we estimate the line tension through the drop-size dependence of the contact angle and find good agreement with theoretical predictions. For the phase separated monolayers, the $HOCH_2$-terminated chains are organized into randomly located circular domains which are embedded in a background matrix of CH_3-terminated chains. For $\chi_p = 0.5$, we consider two domain sizes with the diameters of the small and large domains being 1 and 2 nm, respectively. The water contact angle is found to be 63.1° for the monolayer with small domains and 68.1° for the monolayer with large domains. The results for the homogeneous and phase separated monolayers with $\chi_p = 0.5$ indicate that the nanoscale wetting behavior of the SAM is sensitive to its nanostructure.

3.1 Introduction

Self-assembled monolayers (SAMs) of alkanethiols on noble metals have received much attention in recent years because they are simple to prepare and provide well-ordered, dense monolayers [62]. SAMs have been used in a broad range of areas including biocompatibility [63, 64], molecular electronics [65, 66], corrosion [67], and wettability [68, 69, 70, 71, 72]. The wettability of a SAM may be tuned by the choice of terminal functional group or by the mixing ratio of multi-component SAMs. Given the consistency of the monolayer at full coverage, a pure liquid drop on a single-component SAM is expected to follow the Young-Dupré equation:

$$\gamma_{SV} - \gamma_{SL} = \gamma \cos\theta, \tag{3.1}$$

where γ is the liquid-vapor tension, γ_{SL} is the solid-liquid tension, γ_{SV} is the solid-vapor tension, and θ is the equilibrium contact angle.

Many applications require self-assembled monolayers to be patterned at small scales. Microcontact printing [73], photolithography [74, 75] and other methods have been shown to pattern SAMs at the microscale. To chemically pattern surfaces at the nanoscale, techniques such as nanoshaving [76, 77], electrochemical etching, or dip-pen nanolithography [78] may be used. These methods rely on a scanning probe microscope (SPM) and while the designs they produce are intricate they are limited to square-micron sized planar areas. SAMs may also be patterned at the nanoscale by the coadsorption approach where mixed monolayers spontaneously phase separate. Typically, this produces single-component domains of nanometers in size. A second approach is sequential adsorption where one component is allowed to form islands on the substrate before a second component is added to serve as the background matrix. The SPM approaches offer far more control of the pattern in comparison to the latter two techniques. However, mixed and sequential adsorption are easier to employ and may be applied to curved surfaces such as those of micro [79] and nanoparticles [80]. They may also to applied to surfaces of macroscopic dimensions.

The majority of coadsorption studies have used ethanol as the solvent and Au(111) as the metal surface. In their study of mixtures of methyl- and hydroxyl-terminated alkanethiols of similar chain length, Whitesides and coworkers [68] con-

cluded that the chains were not necessarily randomly dispersed and that single-component domains may be present at tens of angstroms in size. Using infrared reflection-absorption spectroscopy (IRAS), Bertilsson and Liedberg [81] concluded that the chains in mixed monolayers of $CH_3(CH_2)_{15}SH$ and $HOCH_2(CH_2)_{15}SH$ showed complete mixing for $\chi_p \leq 0.5$. Stranick et al. [82] using scanning tunneling microscopy (STM) showed that mixed monolayers of $CH_3(CH_2)_{15}SH$ and $CH_3O_2C(CH_2)_{15}SH$ on Au(111) formed nanometer scale molecular domains. The two alkanethiols in this case have similar chain length and are weakly interacting (i.e., they do not hydrogen bond with one another). The size of the domains was reported to be 2 – 10 nm. Nanoscale phase-segregation was later confirmed for mixtures of $HOCH_2(CH_2)_{15}SH$ and $CH_3(CH_2)_{15}SH$ and ruled out for $NCCH_2(CH_2)_{15}SH$ and $HOCH_2(CH_2)_{15}SH$ [83].

The atomic force microscopy (AFM) studies of Tamada et al. [84] also showed single-component domains of size 10 – 20 nm for a specific range of mixing ratios of $CH_3(CH_2)_3SH$ and $CH_3(CH_2)_{17}SH$. Hayes et al. [85] used AFM and lateral force microscopy to investigate SAMs composed of $CH_3(CH_2)_{17}SH$ and 4-aminothiophenol, which differ significantly in chain length and terminal group chemistry. The SAMs were shown to phase separate into domains of 10 – 100 nm in size. This system is an ideal candidate for phase segregation because of the disparate nature of the two chains. Mixtures of $HO_2C(CH_2)_3SH$ and $CH_3(CH_2)_{15}SH$ have been shown to phase separate [86, 87]. Depending on the solution concentration for this system the area of the domains was found to vary from tens to hundreds of square-nanometers. Monolayers formed from $HO_2C(CH_2)_{10}SH$ with either $CH_3(CH_2)_9SH$ [88] or $CH_3(CH_2)_{10}SH$ [87, 89] have been shown to give homogeneous mixtures despite the difference in functional group chemistry. Scanning tunneling microscopy

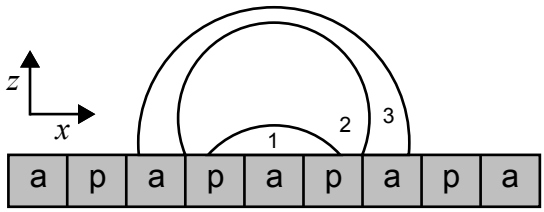

Figure 3.1: The profiles of three water drops of different size are shown on a chemically heterogeneous substrate composed of polar (p) and apolar (a) regions.

studies by Lewis et al. [90] found phase separation for mixtures of $CH_3(CH_2)_9SH$ and two of the three amine-containing alkanethiols considered. An equimolar solution of $CH_3(CH_2)_9SH$ and 3-mercapto-N-nonylpropionamide was found to phase separate with decanethiol forming islands and the amine-containing aklanethiol serving as the background.

Salaita et al. [91] combined dip-pen nanolithography with a phase separating binary solution containing $HO_2C(CH_2)_{15}SH$ to achieve an enhanced degree of patterning resolution. Ternary systems [92] have also been shown to phase separate as well as binary systems on curved substrates [80]. Much less is known about nanoscale phase separation for SAMs composed of alkylsilanes, which are a class of materials that adsorb on hydroxylated surfaces and have structural properties that are similar to those of the alkanethiols.

Brewer and Leggett [93] have conducted chemical force microscopy (CFM) studies on pure and mixed monolayers of $CH_3(CH_2)_{11}SH$ and $HO(CH_2)_{11}SH$. For the pure monolayers the pull-off force measurements are found to follow a Gaussian distribution. However, the mixed monolayers give distributions that are broad and, for certain mixing ratios, have a bimodal appearance. Frictional force microscopy (FFM), which has a larger tip-sample contact area than CFM, suggested that the monolayers were uniformly mixed for all compositions. After comparing the es-

timated contact areas for CFM and FFM to previously reported island sizes for similar SAMs, the authors concluded that single-component domains with areas less than or equal to 15 nm^2 are present in the mixed monolayers. These results and those of Stranick et al. [83] and Bain et al. [68] are particularly important for the present work where nanoscale phase separation for mixtures of $CH_3(CH_2)_{10}SH$ and $HOCH_2(CH_2)_{10}SH$ on Au(111) is assumed.

A number of macroscale experimental studies have examined the effect of phase separation on the wetting behavior of SAMs. Imabayashi et al. [87] examined the water contact angle of homogeneous and artificially phase-separated monolayers of $CH_3(CH_2)_{10}SH$ and $HO_2C(CH_2)_{10}SH$. The domain size for the phase separated monolayers was 5 to 20 nm. The water contact angle of millimeter-size drops was found to be the same for the two monolayers for all surface compositions. The wetting data was shown to agree with the Cassie equation. The Cassie equation [94] is an empirical expression that relates the macroscopic contact angle of a pure fluid on an atomically-smooth solid surface to the area fractions of the materials composing the solid:

$$\cos\theta = f_1 \cos\theta_1 + f_2 \cos\theta_2. \tag{3.2}$$

In Eqn. 3.2, f_i is the area fraction of component i and θ_i is the contact angle of the fluid on a surface of pure i. Fig. 3.1 shows the behavior of water drops of different size on a heterogeneous substrate.

Molecular simulations using interaction potentials for real materials have proven successful in the study of wetting phenomena. Using molecular dynamics simula-

tions, Hautman and Klein [38] showed that a droplet composed of as few as 90 molecules could be used to estimate the water contact angle of either methyl- or hydroxyl-terminated SAMs. The authors point out that such agreement is expected when the bulk region of the droplet is of sufficient size (i.e., the height of the drop is greater than the sum of the liquid-vapor and solid-liquid interfacial thicknesses). While the calculated microscopic contact angles were compared to experimental data for macroscopic systems, the effect of the line tension was not discussed. Other simulation studies have reproduced equilibrium contact angles of real fluids on pure substrates [43, 41, 39, 40].

Recently, Lundgren et al. [95] examined the behavior of nanodroplets of water on chemically and topologically heterogeneous substrates. They used the TIP-3P interaction potential for water while the substrate was modeled as a Lennard-Jones solid. For the flat, chemically heterogeneous substrates, when the ratio of the patch size to drop size was small, the Cassie model was found to hold over the entire range of compositions. However, significant deviations were seen as this ratio became large. This behavior was also found by studies using simple interaction potentials. Adão et al. [96] studied the spreading of a Lennard-Jones droplet on an atomistic solid composed of two materials with different surface energies. The Cassie equation was found to hold for regular and random distributions of the patches, which were no larger than seven atomic diameters. Samsonov et al. [97] examined a similar system with a simpler substrate model and found the agreement between the simulation results and Cassie's law increased as the size of the patches became small relative to the size of the drop.

Brandon et al. [98, 99] have performed numerical calculations to find droplet shapes on substrates where the surface energy varies periodically in one and two

dimensions. The surface of the droplet is approximated as a collection of triangles. When the ratio of the drop size to the wavelength of the imposed contact angle becomes large the shape of the drops approaches that of a spherical cap and there is evidence that Cassie's law holds. The equilibrium surfaces are found to have a constant mean curvature and Eqn. 3.1 is satisfied along the contact line.

Mixtures of alkanethiols have been shown to form dense monolayers on gold lattices. Many experimental studies have shown that for certain binary systems, due to a difference in chain length or terminal group chemistry, the two species will spontaneously phase separate to form a monolayer with nanometer-size single-component domains embedded in a background matrix of the second component. This has specifically been demonstrated for mixtures of CH_3- and HO-terminated chains of similar chain length. To understand how the nanoscale wetting behavior is affected by the degree of mixing of the chains, we have conducted molecular dynamics simulations to investigate this relationship (through the water contact angle) for homogeneous and phase-separated binary SAMs.

3.2 SAM Model

Computer simulation has proven be a useful tool in investigating the structural properties of self-assembled monolayers. Hautman and Klein [100] conducted molecular dynamics simulations of $CH_3(CH_2)_{15}SH$ on Au(111) at room temperature. The methyl and methylene groups were modeled as united atoms while the gold lattice was modeled as a half space (through a 12-3 potential). For both treatments of the Au-S-C valence angle the authors found good agreement with experimental data. The effects of temperature were later studied [101]. Several phases and the tran-

sition temperatures between them were identified. Experimental data at the time suggested a $(\sqrt{3} \times \sqrt{3})$R30° overlayer with the sulfur atoms in the triple-hollow sites [102].

Evidence from low temperature helium diffraction experiments [103] and X-ray diffraction (XRD) data [104] suggested that the monolayer formed a $(4\sqrt{3} \times 2\sqrt{3})$R30° lattice or c$(4 \times 2)$ superlattice. Mar and Klein [105] conducted MD simulations in an attempt to identify the specific structure of the chains forming the c(4×2) superlattice. Using an all-atom model for $CH_3(CH_2)_{15}SH$ on Au(111) with the sulfur atoms subject to a lateral corrugation potential, the most stable structure found was the two chains per unit cell herringbone arrangement. Three structures with four chains per unit cell were identified that had comparable potential energy to that of the herringbone arrangement. However, each was incompatiable with the XRD data. Many of the SAM models to follow are in some way based on the early works described in Refs. [100, 105]. SAMs with OH and NH_2 terminal groups have also been studied by computer simulation [106].

Pertsin and Grunze [107] carried out molecular mechanics calculations where the minimum energy structures for the different chemisorption modes of $CH_3(CH_2)_{17}SH$ on Au(111) were determined. Using a model with explicit hydrogen atoms, the most stable structures were found to have either one or two chains per unit cell.

STM studies confirmed the c(4×2) superlattice [108, 109, 110] and produced multiple contrasts. Bhatia and Garrison [111] used a united atom model based on Ref. [100] in their molecular dynamics study of short and long chain alkanethiols on gold. Eight layers of the metal lattice were explicitly treated with the top three layers obeying Newton's equations of motion. For the short chains the investigation identified one structure that had four chains per unit cell while three structures were

found for the long chain thiols. All structures were consistent with the XRD data of Fenter et al. [104]. The effects of temperature on the structure of a monolayer composed of $CH_3(CH_2)_{17}SH$ on Au(111) was determined [112]. An orientational transition was observed below room temperature where the direction of tilt changes from nearest neighbor to next-nearest neighbor at higher temperatures. At higher temperatures the chains untilt and the structure transforms to a disordered phase with orientational freedom. The order-order and order-disorder transformations have both been observed experimentally.

Li et al. [113] conducted molecular mechanics calculations and MD simulations of $CH_3(CH_2)_{15}SH$ and $CH_3(CH_2)_{16}SH$ on Au(111). The stability of different strucutures was examined for different choices of the hybridization mode of the sulfur atoms. The lowest potential energy structures were found to have one chain per unit cell. The authors found a similar result for monolayers composed of 4′-alkoxybiphenyl-4-thiols.

Using a united atom model, Rai et al. [114] performed MD simulations of $CH_3(CH_2)_{14}SH$ on Au(111) where five layers of the gold lattice were treated explicitly. The role of the Au−S−C valence angle was examined as well as temperature effects. Large-scale all-atom molecular dynamics simulations were conducted by Vemparala et al. [115] to study the effects of chain length, lattice spacing, and temperature on SAMs. Alexiadis et al. conducted quantum, first-principles calculations of methanethiolate on the (111) planes of gold, silver, and plantinum to determined the preferred positions of the sulfur atoms [116]. This data was then used to parameterize a classical force field where methyl and methylene groups were represented by united atoms. The force field was used for Monte Carlo simulations of $CH_3(CH_2)_nSH$ for $n = 9$, 15, and 21 on Au, Ag, and Pt.

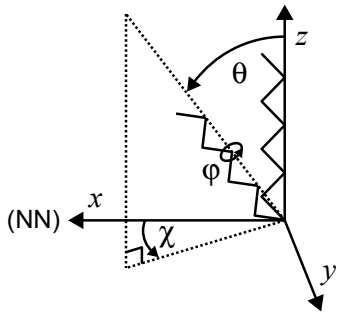

Figure 3.2: The orientation of each chain in the monolayer is described by a tilt angle (θ), a direction of tilt (χ), and a twist angle about the molecular axis (φ). This diagram is shown for a methyl-terminated chain with its eight atomic units. The x-direction corresponds to a nearest-neighbor (NN) direction.

The homogeneous and phase separated monolayers used in this work are composed of 50 chains in the x-direction and 58 chains in the y-direction. We adopt the model for Phase B of Ref. [117] where the monolayer forms a $(4\sqrt{3} \times 2\sqrt{3})$R30° lattice or c(4×2) superlattice. The sulfur atoms are located in the triple-hollow sites where they form a triangular lattice with nearest-neighbor spacing $a = 4.97$ Å. Each of the four chains per unit cell have the same tilt angle ($\theta = 30°$) and direction of tilt ($\chi = 15°$). The individual twist angles are different. Figs. 3.2 and 3.3 show the structural model used in our work.

The wetting properties of SAMs composed of alkanethiols become independent of chain length when the number of methylene groups in the chain becomes large. Specifically, this has been shown for mixed monolayers of $CH_3(CH_2)_nSH$ and $HOCH_2(CH_2)_nSH$ for $n = 10$ and 18 [68] and $CH_3(CH_2)_nSH$ and $HO_2C(CH_2)_nSH$ for $n = 10$ and 15 [68, 118]. To reduce computation time we therefore only consider the top eight or ten atomic layers of the monolayer and ignore the remaining methylene groups, sulfur atoms, and gold lattice. Methyl and methylene groups are treated as united atoms while the oxygen and hydrogen atoms of the hydroxyl

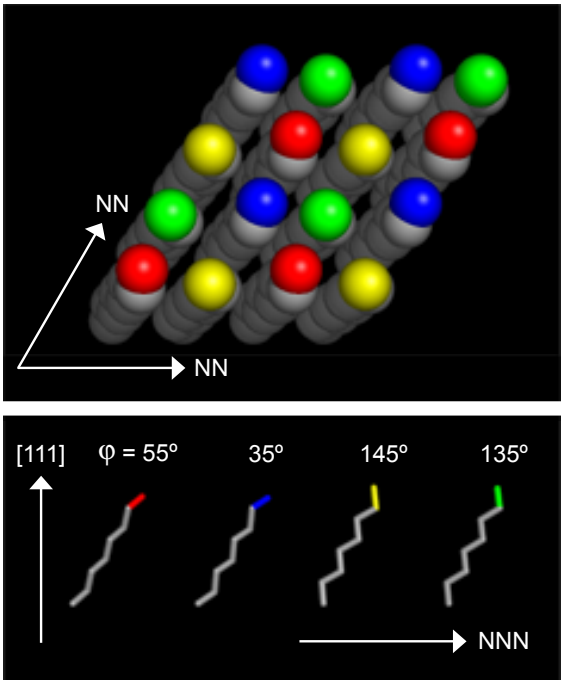

Figure 3.3: The top image shows the top view of a region of a monolayer with methyl-terminated chains. The twist angles are indicated by color in the bottom image. The next-nearest neighbor (NNN) direction corresponds to $\chi = 30°$ in Fig. 3.2.

group are treated atomically. This means that methyl-terminated chains are composed of eight atomic units or $-(CH_2)_7CH_3$ while hydroxyl-terminated chains are composed of ten or $-(CH_2)_7CH_2OH$. The positions of the bottom two atomic layers (or three for one run) of each chain are fixed throughout the simulation. This keeps the self-assembled monolayer in place and helps to impose the proper structure on the chains.

While the model of Riposan and Liu [117] was proposed for 1-undecanethiol, evidence exists to suggest that it will also apply to 11-mercapto-1-undecanol. Dannenberger et al. [119] have shown that the overall structure of pure methyl- and hydroxyl-terminated SAMs are similar for chains of the same length. For instance, they find $CH_3(CH_2)_{21}SH$ and $HOCH_2(CH_2)_{21}SH$ on Au(111) to have a thickness of 25.4 Å and 25.9 Å, respectively. When the number of methylene groups is reduced by six both monolayers give a height of 18.9 Å. The tilt angles for these monolayers as determined by XPS and near edge X-ray absorption fine structure spectroscopy (NEXAFS) are also very similar. Sprik et al. conducted molecular dynamics simulations to investigate the structure of pure SAMs with OH or NH_2 terminal groups [106]. Their results showed a similar overall structure when compared to SAMs with CH_3 termination.

The starting point for the construction of the mixed monolayers was a methyl-terminated monolayer (i.e., $\chi_p = 0$). Alcohol-terminated chains were introduced by randomly selecting a methyl-terminated chain and replacing its CH_3 group with a $HOCH_2$ group. This process was repeated until the desired value of χ_p was achieved.

The phase separated monolayers were constructed in a similar manner. A single chain was selected at random. If this chain and the six closest chains to it (or eighteen in the case of the large domains) were methyl-terminated then a domain

was created by changing the termination of each chain to a $HOCH_2$ group. If the criteria was not satisfied then the process was repeated. These rules for creating the phase separated monolayers allow for domains to be adjacent to each other but non-overlapping. In the case where an integral number of domains did not give the desired overall composition, single chains were converted at random to account for the difference.

3.3 Simulation Methodology

The wetting behavior of water droplets composed of 4000 molecules was examined on binary self-assembled monolayers. A droplet was constructed by extracting a hemispherical cluster from a large simple cubic lattice of randomly-orientated water molecules arranged at ambient liquid density. The droplet was placed in the vicinity of the monolayer. The chains in the monolayer were initialized with $\theta = 30°$, $\chi = 15°$, and the twist angles indicated in Fig. 3.3. Conjugate gradient energy minimization was performed for 10,000 steps.

The parallel molecular dynamics (MD) simulations [120] were carried out at constant number of molecules, system volume, and temperature using the third-party code NAMD [121]. The temperature was maintained at 298.15 K by applying a Langevin thermostat, with a damping coefficient of 0.5 ps^{-1}, to non-hydrogen atoms. The Verlet method was used to perform the numerical integration of the equations of motion for the monolayer while SETTLE [59] was used for water. A timestep of 1 fs was used. All bonds in the monolayer were kept fixed using SHAKE [56]. The SPC/E interaction potential [54] was used for water while the OPLS-UA force field [122, 123] was used for the monolayer (see Table 3.1). The OPLS combining rules

were used for water-monolayer interactions. The interaction between any pair of atoms in the same chain which are separated by three or fewer bonds was excluded. Short-range interactions were cutoff at 12 Å with a switching function applied for separations greater than 10 Å. The dimensions of the simulation cell were L_x = 258.50 Å, L_y = 249.64 Å, and L_z = 250.00 Å. Periodic boundary conditions in three dimensions were used. The PME technique [124, 125] was used to account for long-range interactions with the smallest number of grid points per direction being 0.92 $Å^{-1}$. The simulations were run on DataStar at the San Diego Supercomputer Center. Using twenty-four IBM p655 nodes or 192 processors the simulations ran at roughly 30 ms/step. The atomic coordinates were written to file every 2 ps.

One run was carried out for each of the five homogeneous monolayers. Because the spreading rate varies with monolayer composition the total simulation time was different for each run with the $\chi_p = 0$ case needing only 4 ns and the $\chi_p = 1$ case requiring 13 ns. For the phase separated monolayers, seven runs of 4 ns each were carried out for both the small and large domain cases for the only choice of $\chi_p = 0.5$.

Several checks were performed using a homogeneous monolayer with $\chi_p = 0.5$ to ensure that the chosen simulation parameters were not introducing artifacts. In two separate simulations the transverse area and height of the simulation cell were doubled keeping the number of grid points per direction constant in the PME calculation. The contact angles and wetting dynamics were found to be very similar to the original case suggesting that image droplets were not influencing the results. The effect of different droplet shapes at initialization was also studied. With each case having the same number of total water molecules, we considered a rectangular drop, a spherical drop, and two spherical drops separated by a few angstroms. In all cases the average contact angle was found to be within one degree of θ for the

Bond	Length (Å)
O–H[a]	1.000
O–H	0.945
CH_2–O	1.430
CH_2–CH_2	1.530
CH_2–CH_3	1.530

Valence	k_θ	θ_0 (°)
H–O–H[a]	–	109.47
H–O–CH_2	110.02	108.5
O–CH_2–CH_2	100.09	108.0
CH_2–CH_2–CH_2	124.20	112.0
CH_2–CH_2–CH_3	124.20	112.0

Dihedral	V_1	V_2	V_3
H–O–CH_2–CH_2	0.417	0.058	0.374
O–CH_2–CH_2–CH_2	0.351	0.106	1.530
CH_2–CH_2–CH_2–CH_2	0.7055	0.136	1.573
CH_2–CH_2–CH_2–CH_3	0.7055	0.136	1.573

Nonbonded i–i	σ_{ii} (Å)	ϵ_{ii}	q_i (e)
H–H[a]	0.0	0.0	0.4238
O–O[a]	3.166	650.2	−0.8476
H–H	0.0	0.0	0.265
O–O	3.070	711.8	−0.700
CH_2–CH_2[b]	3.905	493.9	0.435
CH_2–CH_2[b]	3.905	493.9	0.0
CH_3–CH_3	3.905	732.5	0.0

Table 3.1: Force field for the MD simulations. [a]These parameters apply to SPC/E water while all others apply to the binary SAM. [b]A CH_2 united atom is neutral except when directly bonded to an alcohol group where it has a partial charge of $0.435e$. The OPLS combining rules are $\sigma_{ij} = \sqrt{\sigma_{ii}\sigma_{jj}}$ and $\epsilon_{ij} = \sqrt{\epsilon_{ii}\epsilon_{jj}}$.

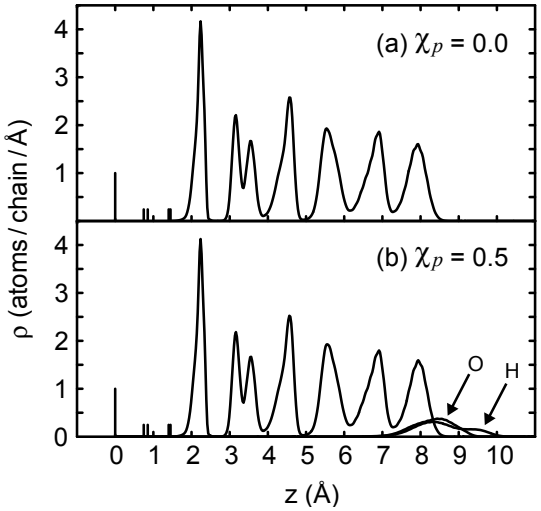

Figure 3.4: Atomic density profiles normal to the surface for two choices of χ_p.

reference case. A similar result for water on graphite was found by Werder et al. [40]. The fact that the contact angle is independent of the initial shape of the drop is not surprising because thermal fluctuations at this scale are sufficiently large to quickly drive the system out of metastable states. Because of this, for the monolayers considered in this work the contact angles we report are the equilibrium values.

3.4 Results and Discussion

3.4.1 SAM Structural Properties

Simulations of the monolayer in the absence of a water droplet have been conducted to determine its structural properties. Two different choices of χ_p were considered. Each simulation was performed for 400 ps with average values computed over the final 200 ps.

The atomic density profiles normal to the surface are shown in Fig. 3.4 for $\chi_p = 0$ and 0.5. In Fig. 3.4a, the distributions of methyl and methylene groups

have been combined into a single curve. The atomic density of these groups is seen to vary sharply with position indicating that the atoms are largely constrained to equilibrium sites. The distribution of carbon-containing groups are very similar between the two monolayers (Figs. 3.4a,b). This suggests that the addition of $HOCH_2$ groups to half of the chains has little impact on the underlying structure. For $\chi_p = 0.5$, the oxygen and hydrogen atoms are found be broadly distributed in comparison to any methylene group in the chain. This behavior is due to lateral hydrogen bonding between adjacent chains with $HOCH_2$ terminal groups.

With the bottom two atoms of each chain being fixed, the four different twist angles lead to five planes where the methylene density is constant. These planes correspond to the vertical lines in Fig. 3.4. There are four times as many atoms in the $z = 0$ plane as in the planes at $z = 0.75$, 0.85, 1.40, and 1.45 Å. While the atomic densities at each of these locations are mathematically infinite, in Fig. 3.4 they have been drawn with a magnitude equal to the contribution they make to the integral $\int_{-\infty}^{\infty} \rho_C(z)dz$, where $\rho_C(z)$ is the density of carbon-containing groups at z. That is, the distribution at $z = 0$ contributes 1 atom/chain while the others each contribution 1/4 atoms/chain.

In the model used here CH_3- and $HOCH_2$-terminated chains have five and seven dihedral angles, respectively. The percentage of gauche defects as a function of dihedral angle number for the two monolayers is shown in Fig. 3.5. For both monolayers there are few gauche defects for dihedral angles 1 through 5. For $\chi_p = 0.5$, angles 6 and 7 show a high percentage of defects. This is attributed to lateral hydrogen bonding. It can be seen from the force field parameters in Table 3.1 that based on the dihedral potential alone the energy barrier between the trans and gauche states is much less in the case of the CH_2-CH_2-O-H angle than the

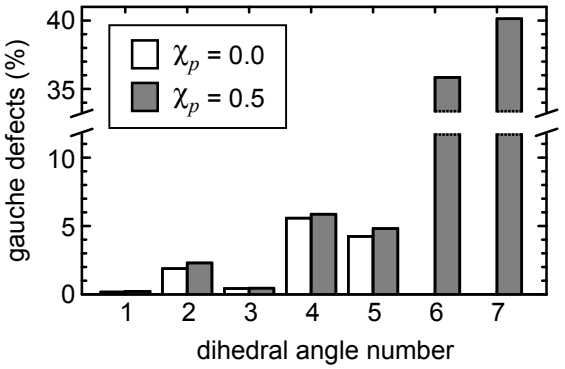

Figure 3.5: Percentage of gauche defects as a function of dihedral angle number for two choices of χ_p. The numbering scheme begins with angle 1 which involves the two fixed atoms. Note that the ordinate is interrupted.

CH_2-CH_2-CH_2-CH_2 angle.

The distribution function for the chain tilt angle is shown in Fig. 3.6. The tilt angle is the angle between a unit normal surface vector, $\boldsymbol{n}$, and the vector formed by the average position of the fixed atoms and the average position of the free atoms per chain, $\boldsymbol{r}$. The model suggested by Riposan and Liu [117] has a tilt angle of 30° for all chains. Our simulations for $\chi_p = 0$ and 0.5 give average tilt angles of 26.0° and 25.4°, respectively. The double peak for the methyl-terminated monolayer is due to the rigidity of the bottom atomic layers and the two pairs of similar twist angles. When $HOCH_2$ groups are present, as with the $\chi_p = 0.5$ case, hydrogen bonding disrupts the tilt angle distribution in such a way that the two peaks are replaced by a single peak with a shoulder.

Fig. 3.7 shows the distribution function for the direction of tilt. The angle χ is formed by a unit vector pointing in the x-direction (or NN direction) and $\langle r_x, r_y, 0\rangle$. At initialization, the tilt direction of each chain is set to $\chi = 15°$ (or the NNNN direction) as prescribed by the model in Ref. [117]. The monolayer was found to relax during the early stages of the simulation. The equilibrium distributions for

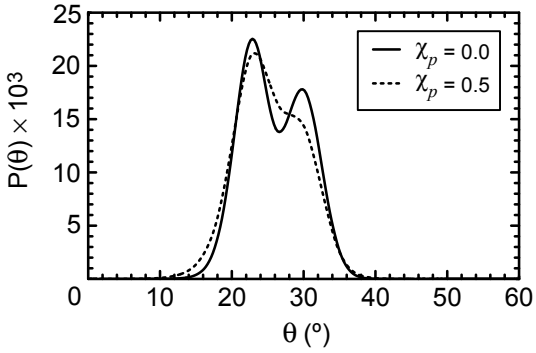

Figure 3.6: Probability distribution function for the tilt angle for two choices of χ_p.

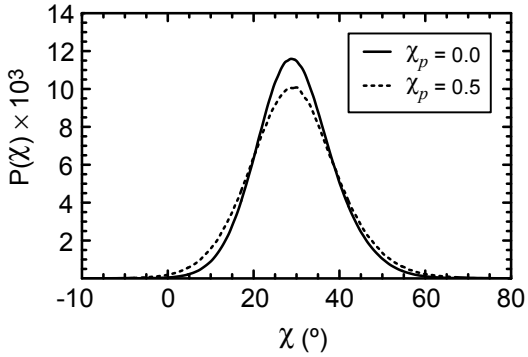

Figure 3.7: Probability distribution function for the direction of tilt for two choices of χ_p. Nearest-neighbor directions correspond to $\chi = 0°$ and 60° while the next-nearest neighbor direction corresponds to $\chi = 30°$.

both monolayers are found to be centered about $\chi = 29°$ or the NNN direction. This shift is allowed to take place because only the bottom two atomic layers are fixed so reorientation of the chain backbones is possible.

An additional simulation was performed for the $\chi_p = 0$ monolayer with the bottom three atomic layers kept fixed instead of only two. This resulted in a tilt angle distribution that was very similar to the original case. With three fixed atoms the chain backbone becomes far more inflexible, which is due to the strong preference for the all-trans conformation. The distribution of the direction of tilt was found to be centered about $\chi = 21°$, which is closer to the target value of 15°. As the number

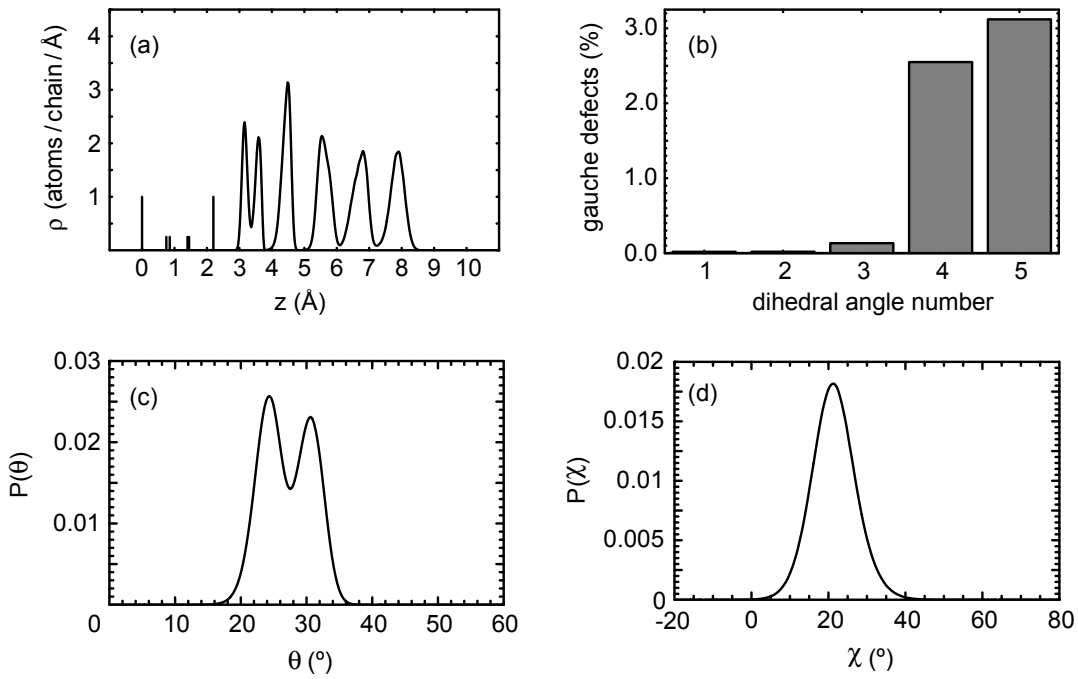

Figure 3.8: Structural results for three fixed atoms: (a) Methyl and methylene density, (b) gauche defects, (c) tilt angle distribution and (d) direction of tilt distribution.

of fixed atoms per chain increases the model becomes less realistic, but given the improvement in the structure it is recommended that this choice be made for future studies.

We have also conducted simulations to investigate the effect of the number of fixed atoms per chain on the water contact angle. For these simulations the monolayer was composed of $-(CH_2)_7CH_3$ and $-(CH_2)_6OH$ with the chains arranged in the $(\sqrt{3} \times \sqrt{3})$R30° structure. For $\chi_p = 0.5$, when the number of fixed atoms per chain was 8, 6, and 2, θ was found to be 83.2°, 80.1°, and 77.6°, respectively. Because hydrogen bonding is highly directional, as the number of fixed atoms per chain increases the average number of hydrogen bonds formed between the monolayer and the droplet decreases. This explains why the contact angle increases with

the number of fixed atoms per chain.

3.4.2 Homogeneous Monolayers

The wetting behavior of droplets of water composed of 4000 molecules was examined on uniformly mixed self-assembled monolayers. Five monolayers were considered with $\chi_p = 0$, 0.25, 0.5, 0.75, and 1. At $t = 0$, the hemispherical droplet is placed in the vicinity of the substrate with its center-of-mass aligned with the origin in the xy-plane. The system was then evolved in time according the MD method.

The normal component of the center-of-mass position of the droplet versus time is shown in Fig. 3.9 for five choices of χ_p. As χ_p increases, the surface energy of the monolayer increases and the droplet is found to spread more. For $\chi_p = 0$ or the methyl-terminated monolayer, z_{CM} is seen to increase during the first 200 ps of the simulation and then fluctuate about its equilibrium value of 30.8 Å. Over the last 1.5 ns of the simulation the instantaneous value of z_{CM} never deviates from the average value by more than ± 2 Å. For the $\chi_p \geq 0.75$ cases, the center-of-mass position is seen to decrease with time before fluctuating about an equilibrium value. Once equilibrium has been established deviations from the average value of z_{CM} are less than ± 1 Å for each of these cases. The simulation with $\chi_p = 1$ was run for 13 ns to ensure that spreading had stopped.

The transverse components of the center-of-mass position of each droplet for all time are shown in Fig. 3.10. The center-of-mass of each droplet begins at the origin and with time it changes due to thermal fluctuations and local gradients in the substrate surface energy. The final position of the droplet is indicated by the open circle in each plot. In general, the displacement from the origin decreases with increasing χ_p. That is, the droplets on the monolayers with $\chi_p = 0$ and 0.25 (Fig.

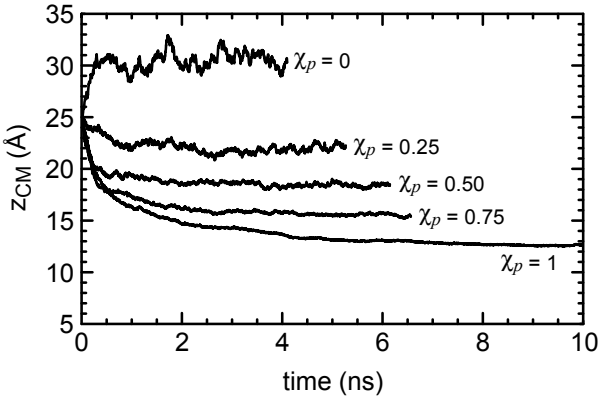

Figure 3.9: The normal component of the center-of-mass position of a water droplet on a homogeneous SAM as a function of time for different values of χ_p. The bottom layer of fixed atoms is located at $z = 0$.

3.10a,b) exhibit much more mobility than the $\chi_p = 0.75$ and 1 cases (Fig. 3.10d,e) which move only a few angstroms.

Side views of the final configurations for $\chi_p = 0$, 0.5, and 1 are shown in Fig. 3.11. The water droplet on the CH_3-terminated monolayer in Fig. 3.11a is seen to have a contact angle larger than 90°. As χ_p increases the droplet spreads more. Fig. 3.11c shows that the droplet on the $HOCH_2$-terminated monolayer has spread to a thickness of a few molecules. No bulk region is present in this case. The tilt of the chains is clearly seen as well as gauche defects near the top of each monolayer. The top view of the $\chi_p = 0.5$ case is shown in Fig. 3.12. Occasionally, one or two water molecules will detach from the droplet and act as a vapor. An example of this is seen in Fig. 3.11a. This behavior has been reported by other authors for similar systems [38, 39] and it expected based on the saturation properties of water.

The procedure of de Ruijter et al. [126] was adopted to determine the equilibrium shape of each droplet. In short, the time-averaged fluid density field is found about the center-of-mass axis of the droplet by assigning molecules to cylindrical bins of

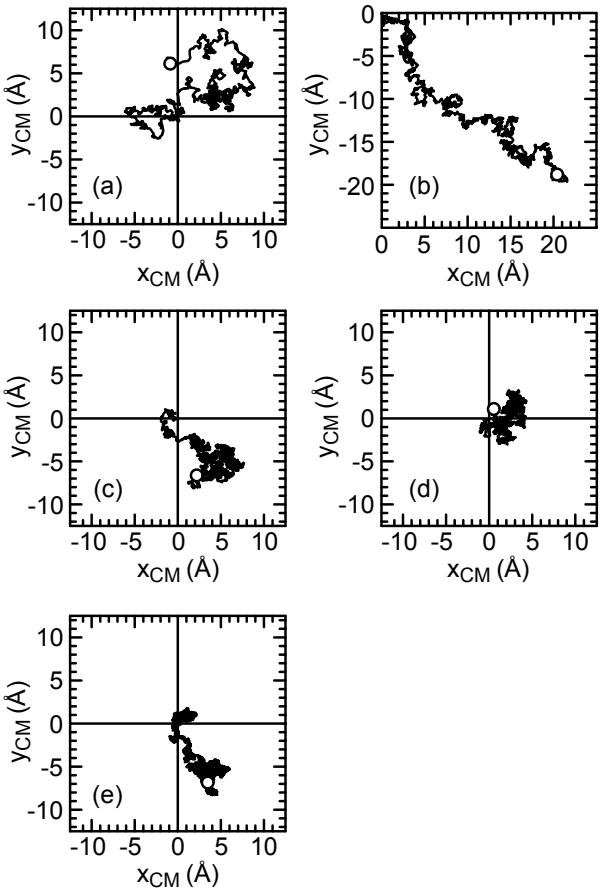

Figure 3.10: The transverse components of the center-of-mass position of the droplet are shown for all time on a homogeneous monolayer: (a) $\chi_p = 0$, (b) $\chi_p = 0.25$, (c) $\chi_p = 0.5$, (d) $\chi_p = 0.75$, and (e) $\chi_p = 1$. The open circle in each plot indicates the final position of the droplet.

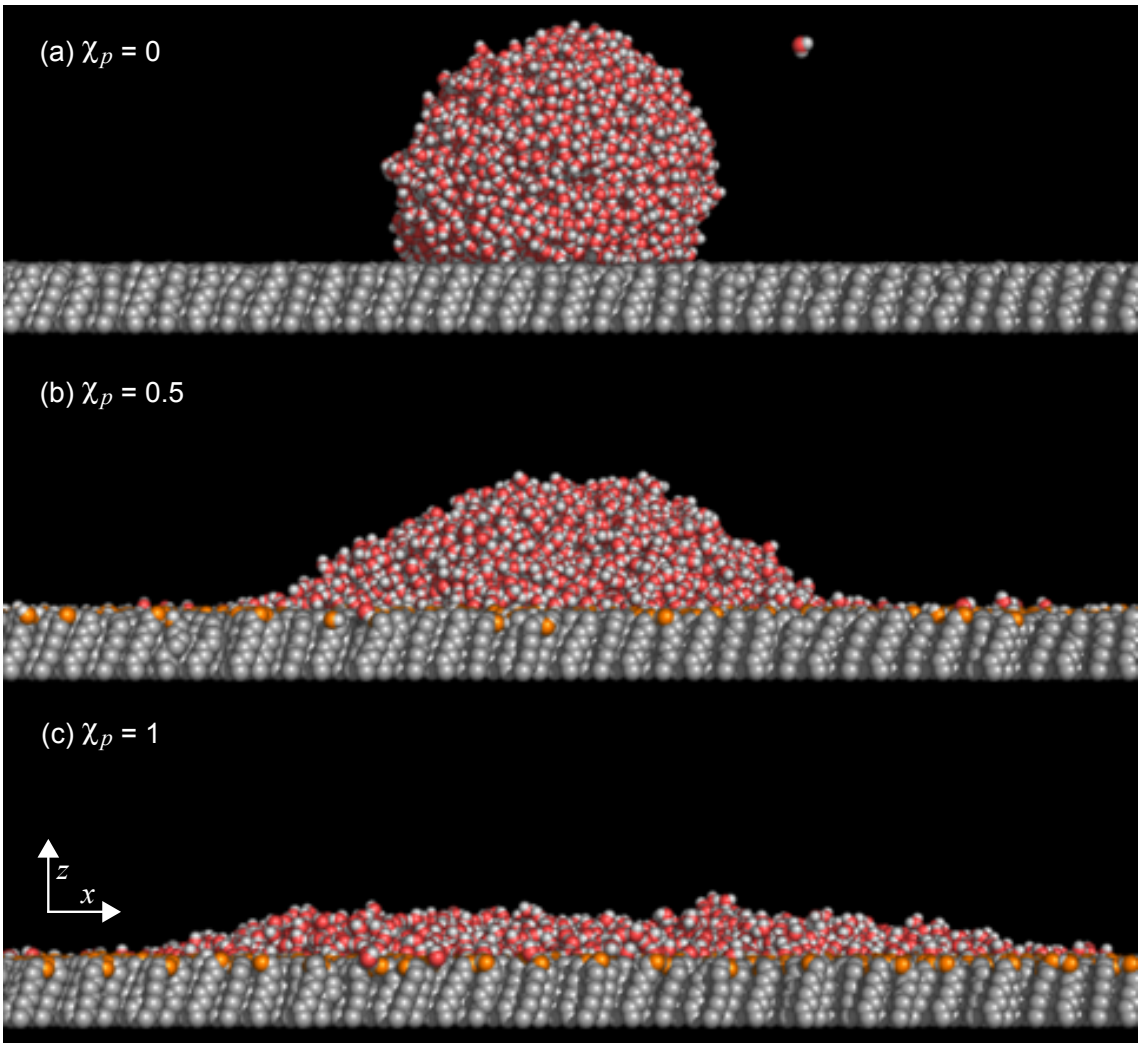

Figure 3.11: Side view of the final configuration of a water droplet composed of 4000 molecules on a homogeneous SAM for three choices of χ_p. The width of the simulation cell is roughly 50 Å larger than shown. The water molecules are shown with oxygen colored red and hydrogen in white, while the substrate is shown with methyl and methylene groups as gray, oxygen as orange, and hydrogen as white.

volume $\pi\Delta z(r_i^2 - r_{i-1}^2)$, where $r_i = \sqrt{i\Delta A/\pi}$ for $i = 1, 2, ..., n$. Here we use the same parameters as Ref. [40] (i.e., $\Delta z = 0.5$ Å and $\Delta A = 95$ Å^2). When the averaging is complete, for each z-slab the smallest value of r_i is determined where the liquid density falls below one half its bulk value. Data points within 5 Å of the top of the monolayer are ignored because the liquid density varies over this region. Similarly, data points a few angstroms from the apex of the droplet are also discarded. The best-fit circle is found for the set of points $\{r_j, z_j\}$ using a nonlinear fitting routine. The contact angle and other properties are determined with knowledge of the height of the monolayer. The best-fit circle, liquid-vapor boundary profile data points, and tangent line at the droplet edge are shown in Fig. 3.13 for the $\chi_p = 0.5$ case. The empty circles in this figure were ignored when the best-fit circle was determined.

The equilibrium contact angle, height, base radius, and average value of z_{CM} for each droplet on the homogeneous SAMs are given in Table 3.2. The root-mean-square error, E, is used as a measure of the fit between the best-fit circle and the time-averaged liquid-vapor boundary profile. The value of E is fairly constant with the exception of the $\chi_p = 1$ case. For this case, since the shape of the droplet is not that of a spherical cap the contact angle and other properties can only be taken as estimates.

In Fig. 3.14, the simulation results for the cosine of the water contact angle are compared with the experimental data of Bain et al. (Fig. 4 of Ref. [68]). Good agreement is seen between the two data sets. The two lines are Cassie's law based on the simulation results and the experimental data. Poor agreement is seen between the Cassie equation and the actual measurements. For instance, if the Cassie equation were based on the simulation results it would predict a contact angle of 77.0° for $\chi_p = 0.5$ while the simulation value is 51.9°. In Fig. 3.14,

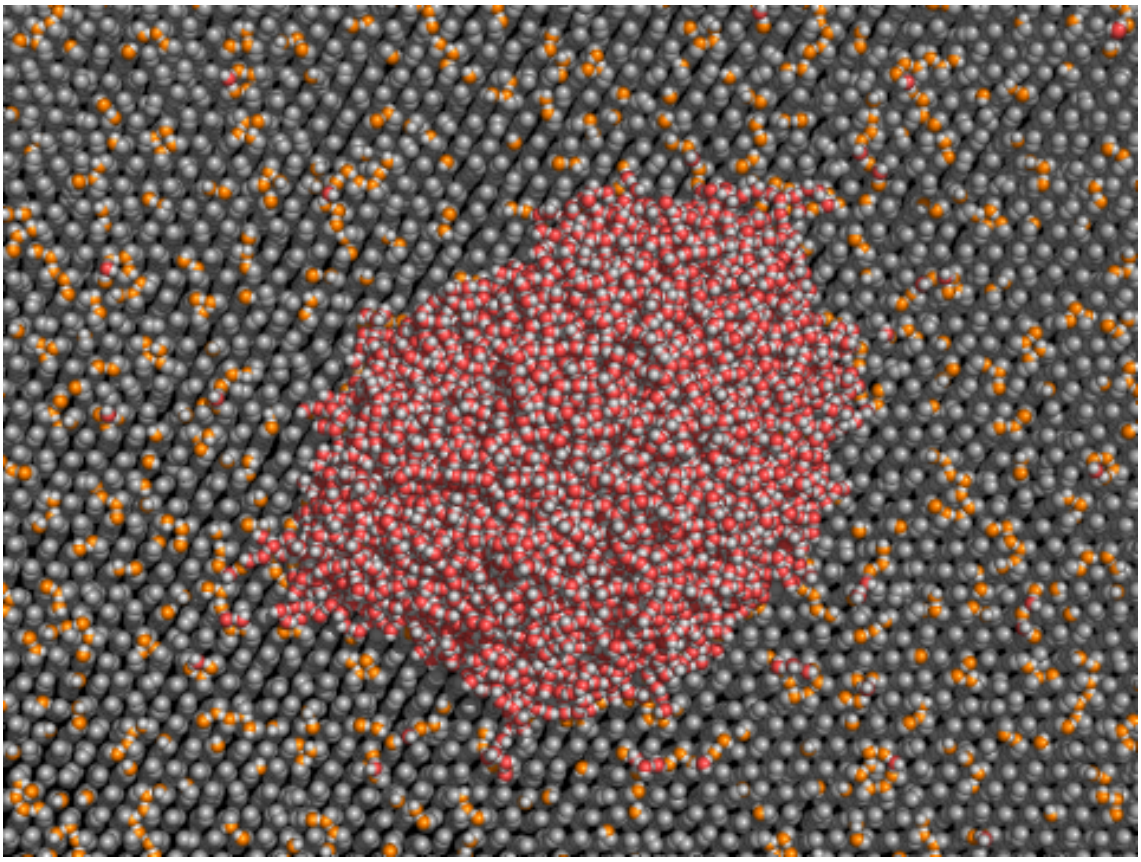

Figure 3.12: Top view of the final configuration of a water droplet composed of 4000 molecules on a homogeneous SAM with $\chi_p = 0.5$. The base area of the simulation cell is roughly twice as large as that shown. Same color scheme as Fig. 3.11.

we have compared macroscopic contact angles that were measured for millimeter-size drops with microscopic values that were measured for nanometer-size drops. For nanometer-size drops the line tension may be important. We will address this concern in Section 3.4.4.

Several other authors have reported the water contact angle for mixed monolayers of CH_3- and HO-terminated chains on Au(111) formed from ethanolic solutions. Arima and Iwata [127] have shown qualitative agreement with Bain et al. [68] for the solution versus surface composition as well as the water contact angle versus

surface composition for mixed monolayers of $CH_3(CH_2)_{11}SH$ and $HO(CH_2)_{11}SH$. For mixed monolayers of $CH_3(CH_2)_{10}SH$ and $HOCH_2(CH_2)_{10}SH$, Semal et al. [128] find different results from those of Bain and coworkers. The authors find a linear relationship between the surface and solution compositions as well as the cosine of the water contact angle and the surface composition. Ethanol was used as the solvent. The authors seem to be unaware of the results in Ref. [68]. Preuss and Butt [79] report that their contact angle data is in agreement with Bain et al. However, the authors assume that the surface composition of the monolayer is equal to the solution composition. And while Bain found contact angle hysteresis to be 10°-20° in Ref [79] it was found to be 25°-30°. The alkanethiols were the same between the two works (i.e., $CH_3(CH_2)_{10}SH$ and $HOCH_2(CH_2)_{10}SH$). Ederth and Liedberg [129] measured the water contact angle over a narrow range of solution compositions for mixtures of $CH_3(CH_2)_{15}SH$ and $HOCH_2(CH_2)_{15}SH$. Bertilsson and Liedberg [81] investigated the relationship between the surface and solution compositions for mixtures of $CH_3(CH_2)_{15}SH$ and $HOCH_2(CH_2)_{15}SH$. The water contact angle was not measured in this study. Lastly, Evans et al. [130] investigated the water contact angle and the stability of mixed monolayers formed from $CH_3(CH_2)_{11}SH$ and $HO(CH_2)_{11}SH$ on Au(111) from tetrahydrofuran solutions. For this case where the alkanethiols and solvent are different from Bain's work, the solution concentration was found to be roughly equal to the surface concentration.

The height of the monolayer was computed using an approach similar to that of Hautman and Klein [38]. The height is taken as the average z-coordinate of the methyl and oxygen atomic centers, $\langle z \rangle$, plus terms to account for the size of the atoms, h_0:

χ_p	θ (°)	h	r_B	z_{CM}	E
0.00	121.9	49.1	27.3	30.8	0.20
0.25	75.9	33.4	42.8	22.1	0.27
0.50	51.9	24.9	51.2	18.5	0.28
0.75	30.5	16.9	62.2	15.6	0.32
1.00	11.6	8.8	86.1	12.7	0.66

Table 3.2: Wetting behavior of a nanodroplet of water on a homogeneous SAM for different choices of χ_p. The microscopic contact angle is θ, the droplet height is h, the base radius of the droplet is r_B, the z-component of the average center-of-mass position is z_{CM}, and E is the root-mean-square error of the best-fit circle to the boundary profile data. h, r_B, z_{CM}, and E are in units of Å.

$$h = \langle z \rangle + (1 - \chi_p)\frac{2^{1/6}\sigma_{\mathrm{CC}}}{2} + \chi_p \frac{2^{1/6}\sigma_{\mathrm{OO}}}{2}, \tag{3.3}$$

where σ_{CC} is the Lennard-Jones parameter for CH_3 appearing in Table 3.1. The wet height, h_W, is computed using only chains that are beneath the droplet whereas the dry height, h_D, is based on chains away from the droplet. Table 3.3 reports the wet and dry heights for each choice of χ_p. The two heights are found to be very similar with the largest difference being 0.44 Å for the $\chi_p = 1$ case. The difference comes about by chains beneath the droplet extending their hydroxyl groups upward to hydrogen bond with water. The dry chains can only hydrogen bond with other chains, which takes place in the plane of the monolayer. All contact angles were calculated using h_W.

The volume of a spherical cap with height h and base radius r_B is $\pi h(3r_B^2+h^2)/6$. While the total number of molecules is the same for each of the five cases in Table 3.2, the data suggests that the droplet volume is decreasing with increasing χ_p. For instance, the volume decreases from 119.5 to 102.8 nm^3 in going from $\chi_p = 0$ to

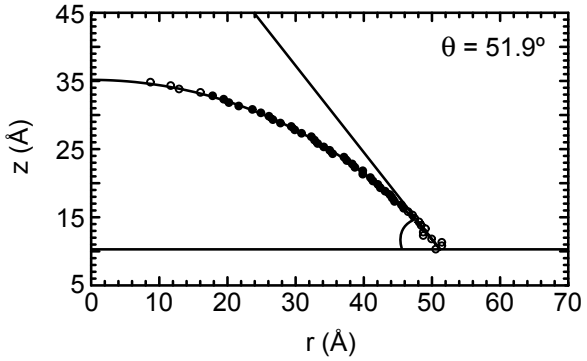

Figure 3.13: The best-fit circle and liquid-vapor boundary profile data points are shown for a water nanodroplet on a homogeneous SAM with $\chi_p = 0.5$. The tangent line at the droplet edge is also shown. The height of the monolayer, h_W, is indicated by the horizontal line. The bottom layer of fixed atoms is located at $z = 0$.

χ_p	$\langle z_W \rangle$	$\langle z_D \rangle$	h_0	h_W	h_D
0.00	7.84	7.89	2.19	10.03	10.08
0.25	8.11	8.03	2.07	10.18	10.10
0.50	8.33	8.13	1.96	10.29	10.09
0.75	8.53	8.19	1.84	10.37	10.03
1.00	8.69	8.25	1.72	10.41	9.97

Table 3.3: The wet and dry heights of the homogeneous monolayers. All values are given in units of Å. h_0 is the sum of the second and third terms in Eqn. 3.3 (i.e., $h_{W/D} = \langle z_{W/D} \rangle + h_0$).

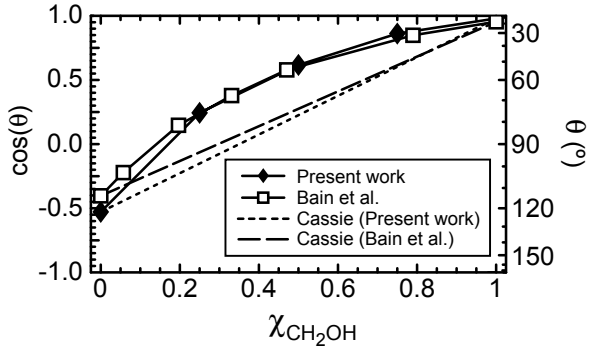

Figure 3.14: Comparison of the wetting data between simulation and experiment. Error bars for the simulation data points are smaller than the size of the symbols.

1. This apparent loss of volume is explained by the fact that as the SAM becomes more hydrophilic, water molecules begin to penetrate the monolayer. This behavior is seen in Fig. 3.11. The contact angle is unaffected by this behavior since it is based on the liquid-vapor boundary profile.

The SPC/E model [54] does better than most simple models at reproducing the bulk and interfacial properties of water. However, its smaller value for the potential energy of bulk water implies a larger water-water interaction strength. Because of this it predicts higher contact angles in comparison to the other models. For instance, Werder et al. [40] find for a water droplet on graphite that the SPC/E and TIP-3P models with the same water-graphite interaction give 65.4° and 48.0°, respectively. The SPC/E model may be the best choice for the current work we simply point out here that if another model were used it would be expected to give smaller values of θ.

Given the regular structure of the monolayer one might expect the droplets to diffuse in certain directions. This may be happening but not enough data was collected to determine if this is so. Simulated AFM measurements have shown that the friction of a methyl-terminated SAM is different depending on whether the

chains have an even or odd number of methylene groups [131].

The chains of the monolayer for $\chi_p = 1$ are found to have a striped appearance away from the droplet. This arises from the formation of a long-ranged hydrogen-bonding network at the surface of the monolayer. The stripes are found to run parallel to nearest-neighbor directions ($\chi = 60°$ and $120°$) with a spacing between stripes of $d = \sqrt{3}a \approx 8.6$ Å (structure II of Fig. 4 of Ref. [106]). Sprik et al. [106] previously reported such an observation in their combined STM and computer simulation study of SAMs with OH termination. Their MD simulations predicted a similar structure but with more disorder. However, their STM images suggested a different structure where the stripe spacing was 4.2 Å. Evidence suggested that a residual ethanol overlayer may contribute to the STM findings.

3.4.3 Phase Separated Monolayers

For the study of phase separated monolayers the overall composition was fixed at $\chi_p = 0.5$. The $HOCH_2$-terminated chains were arranged into circular, single-component domains while the CH_3-terminated chains served as the background. Two domain sizes were considered. The small and large domains were composed of 7 and 19 chains, respectively. With reference to the structure at initialization, a small domain consists of a central chain and its six nearest neighbors at $r = a = 4.97$ Å. A large domain is a small domain with the addition of six next-nearest neighbor chains at $r = \sqrt{3}a \approx 8.6$ Å and six chains at $r = 2a = 9.94$ Å.

The oxygen-oxygen radial distribution function (RDF) is shown in Fig. 3.15 for the homogeneous and phase separated monolayers with $\chi_p = 0.5$. The RDF for the homogeneous monolayer shows a peak of 5.8 at $r = 2.7$ Å. Since the nearest-neighbor separation distance between chains in the monolayer is 4.97 Å this peak

comes about by nearest-neighbor chains tilting towards one another to maximize the van der Waals interaction and form hydrogen bonds. The second peak of 1.1 occurs at $r = 4.8$ Å. Little structure is seen in the homogeneous monolayer for separations greater than 7.5 Å. The radial distribution functions for the phase-separated monolayers are shown in Fig. 3.15b,c. As with the homogeneous case, the phase separated monolayers show a first peak at $r = 2.7$ Å with magnitudes of 7.8 and 8.1 for the small and large domains, respectively. The heterogeneous monolayers have similar second peaks, which occur at $r = 4.9$ Å with a magnitude of 2.0. Beyond this distance the behavior of the phase separated monolayers differ. For the small domains case the RDF is seen to drop below unity after a small third peak while the RDF for the monolayer with large domains remains above unity until separations of 15.2 Å are reached. The crystallinity of the monolayers gives rise to slight features for large separations. In computing these distribution functions the oxygen atoms were assumed to lie in the same plane (which is a reasonable assumption given the narrow distribution of the oxygen atoms in Fig. 3.4b) and the averaging was performed over all $HOCH_2$-terminated chains including those beneath the water droplet. The effect of the water droplet is negligible since the base area of the droplet is approximately one-tenth the area of the monolayer.

The same simulation protocol was followed for the phase separated monolayers as for the homogeneous cases. However, because the substrate is now heterogeneous seven runs were carried out for both the small and large domain cases to ensure that the results were not biased by a droplet spending a disproportionate amount of time in a local free energy minima. The locations of the domains were randomly assigned for each of the seven runs. Each simulation was performed for 4 ns with average values computed over the last 1.5 ns.

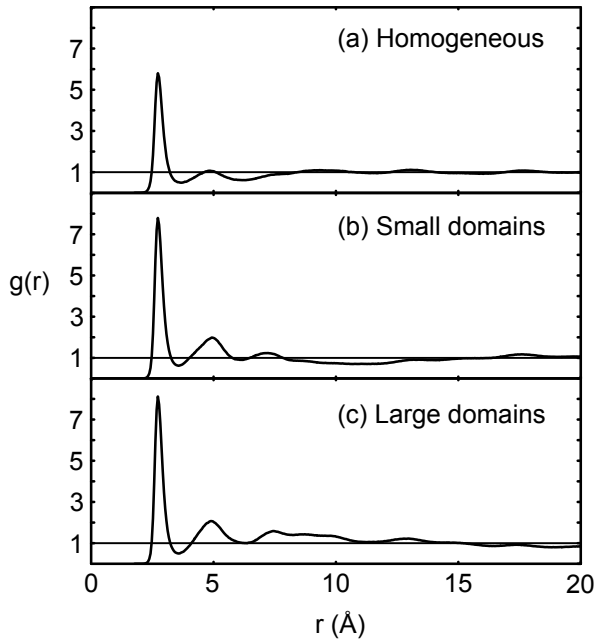

Figure 3.15: The oxygen-oxygen radial distribution functions for three monolayers with different degrees of phase-separation and $\chi_p = 0.5$.

A representative snapshot from one of the runs with small domains is shown in Fig. 3.17. It can be seen that the droplet has an instantaneous shape that deviates from that of a spherical cap. This comes about by the droplet contorting its contact line in an attempt to cover hydrophilic domains while avoiding the hydrophobic background. Because of this the droplet is mostly surrounded by methyl-terminated chains. In Fig. 3.17, the more isolated domains are seen to form circular hydrogen-bonding chains while adjacent domains form linear hydrogen-bonding chains involving twenty or more thiolates. The $HOCH_2$-terminated chains beneath the droplet may form hydrogen bonds with each other and also with water molecules in the droplet.

The time-averaged droplet shapes for each of the seven wetting simulations for the phase separated monolayer with small domains are shown in Table 3.4. The

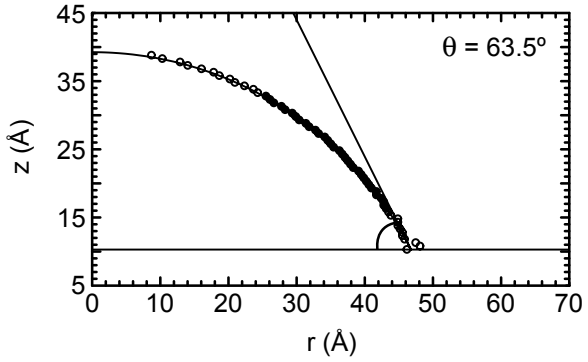

Figure 3.16: Same as Fig. 3.13 except for a phase-separated SAM with small domains.

average contact angle is $63.6 \pm 4.3°$. The values of E indicate that the boundary profile data points are fit by a circle quite well. This emphasizes the notion that while droplet snapshots (e.g., Fig. 3.17) may show large deviations from the spherical cap shape when time-averaged they indeed follow the expected form.

The water contact angle for the phase separated monolayer with small domains was also computed by forming a single boundary profile using all of the configurations over the last 1.5 ns of each of the seven runs. When this was done the contact angle was found to be 63.5°, which is very similar to the result of the previous approach. The contact angle computed in this manner is shown in Fig. 3.16.

A representative snapshot from one of the runs with large domains is shown in Fig. 3.18. Once again the instantaneous droplet shape is found to deviate from a spherical cap. The droplet is found to be surrounded by methyl-terminated chains while on top of a number of hydrophilic domains. As with the small domains, the $HOCH_2$-terminated chains of the large domains are found to form hydrogen-bonding rings or linear chains depending on the spacing between domains.

The time-averaged droplet shapes for the monolayers with large domains are

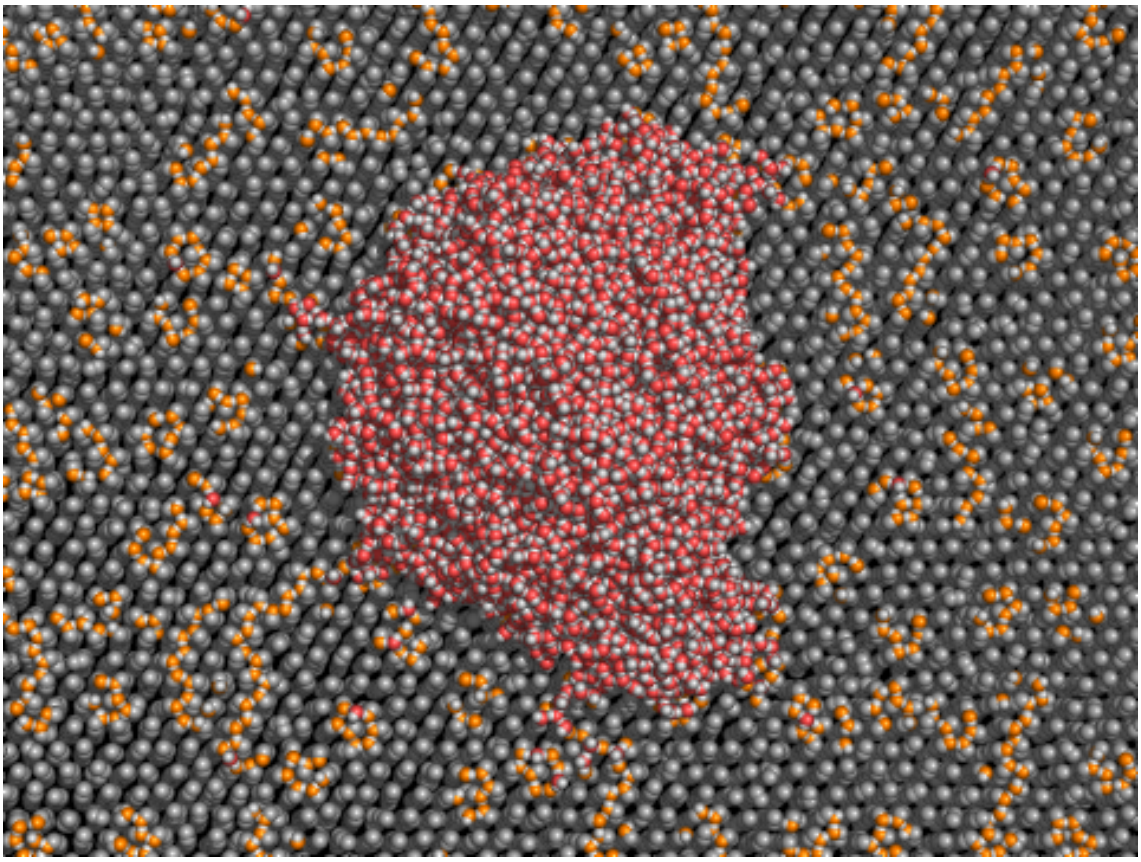

Figure 3.17: Same as Fig. 3.12 except for a phase separated monolayer with small domains (Run 3 of Table 3.4).

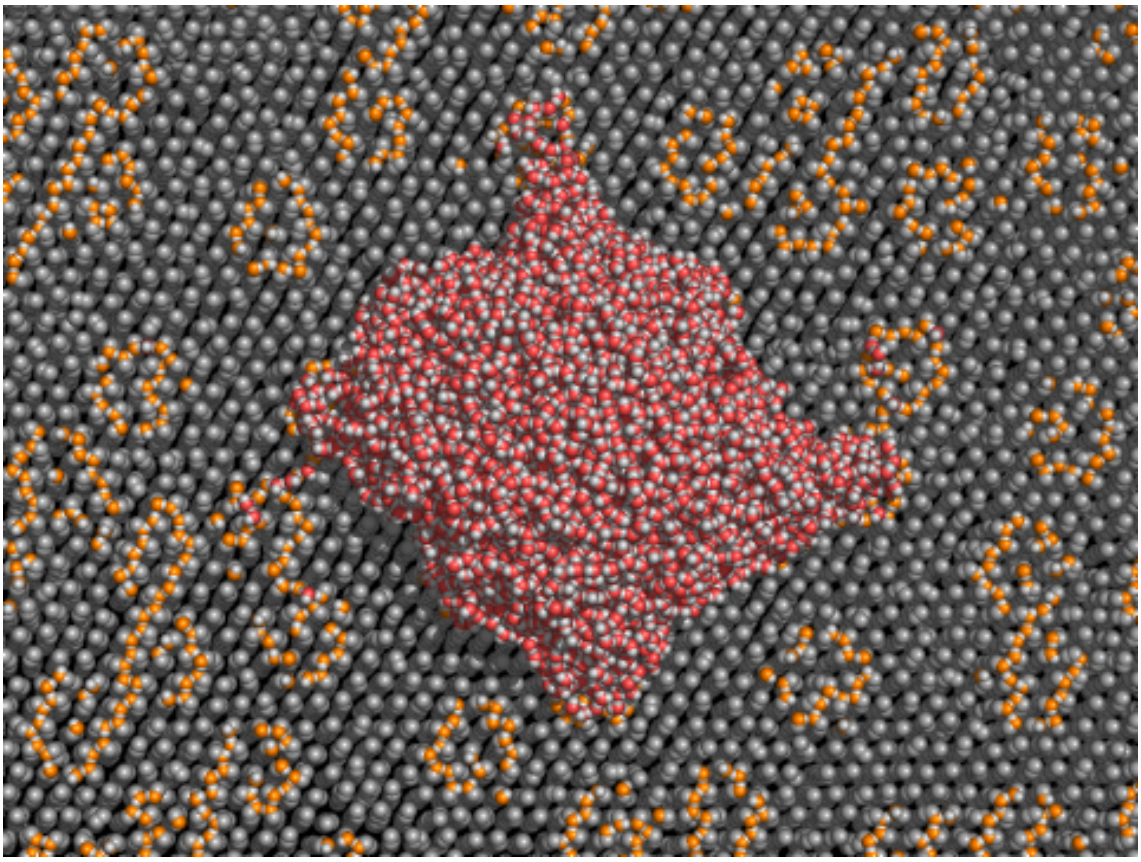

Figure 3.18: Same as Fig. 3.12 except for a phase separated monolayer with large domains (Run 5 of Table 3.5).

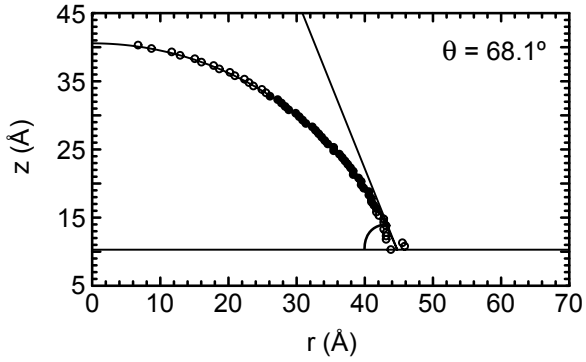

Figure 3.19: Same as Fig. 3.13 except for a phase-separated SAM with large domains.

Run	θ (°)	h	r_B	z_{CM}	E
1	62.7	28.7	47.1	20.0	0.22
2	56.4	26.7	49.7	19.2	0.23
3	63.7	28.8	46.4	19.9	0.23
4	64.8	29.5	46.5	20.3	0.24
5	63.0	28.9	47.2	20.1	0.17
6	71.0	31.6	44.3	21.2	0.21
7	63.5	28.9	46.7	20.1	0.28

Table 3.4: Same as Table 3.2 except for seven runs on a phase separated SAM with small domains and $\chi_p = 0.5$.

reported in Table 3.5. The average contact angle is found to be $66.5 \pm 6.7°$. The average E is larger in this case than for the small domains. The ratio of the average contact angle to its standard deviation is also larger. This indicates that the droplets are more distorted on the monolayer with larger domains. When the configurations from all the productions runs are used in forming a single boundary profile the contact angle is found to be 68.1°. The best-fit circle and boundary profile data points for this latter approach are shown in Fig. 3.19.

The transverse components of the center-of-mass position of selected droplets are shown for the monolayer with small domains in Fig. 3.20 and for the large

Run	θ (°)	h	r_B	z_{CM}	E
1	64.5	28.0	44.5	19.4	0.45
2	71.3	31.7	44.2	21.2	0.20
3	75.0	32.1	41.8	21.0	0.28
4	62.9	28.7	46.9	20.0	0.22
5	70.8	31.3	44.0	21.0	0.14
6	65.9	29.4	45.4	20.2	0.28
7	54.8	25.7	49.6	19.3	0.79

Table 3.5: Same as Table 3.2 except for seven runs on a phase separated SAM with large domains and $\chi_p = 0.5$.

domains in Fig. 3.21. Using the results from all seven runs, the average center-of-mass displacement from the origin is found to be 14.0 ± 9.4 Å on the monolayer with small domains and 8.8 ± 6.6 Å on the monolayer with large domains. This difference comes about by the effective non-uniformity of the locations of the domains in the two cases. That is, from Figs. 3.17 and 3.18 it can be seen that the droplet on the monolayer with small domains is surrounded by fewer methyl-terminated chains than the droplet on the monolayer with large domains. In order for either droplet to move to a new position it must cross this hydrophobic region. Because the hydrophobic region is smaller in the case of the droplet on the monolayer with small domains it is more likely that thermal fluctuations will drive the droplet to a new position in less time.

For the same overall composition of $\chi_p = 0.5$, the water drops on the phase separated monolayers are found to give higher contact angles than the homogeneous monolayer by 12° and 19° for the small and large domain cases, respectively. An explanation for this behavior has been offered by Lundgren et al. [95] and it is illustrated in Fig. 3.1. We imagine slowly increasing the volume of drop 1 while monitoring its profile. At early times, as fluid is added the base area of the droplet

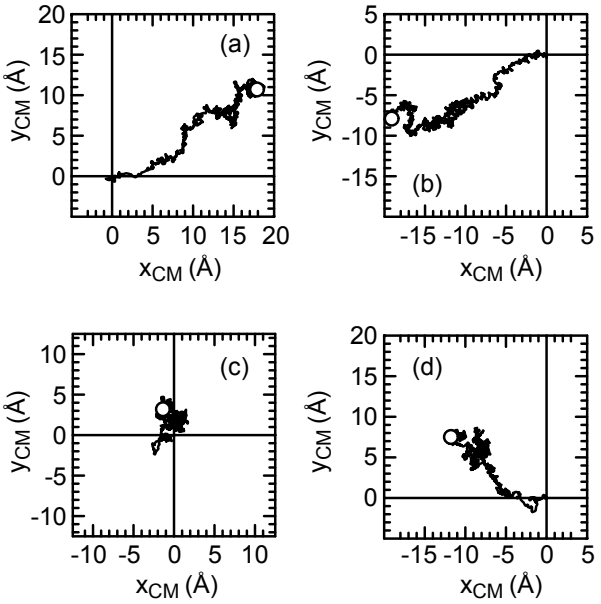

Figure 3.20: The transverse components of the center-of-mass position for all time on a phase separated monolayer with small domains and $\chi_p = 0.5$. The open circle in each plot indicates the final position of the droplet. The four representative runs from Table 3.4 are (a) Run 1, (b) Run 2, (c) Run 3, and (d) Run 6.

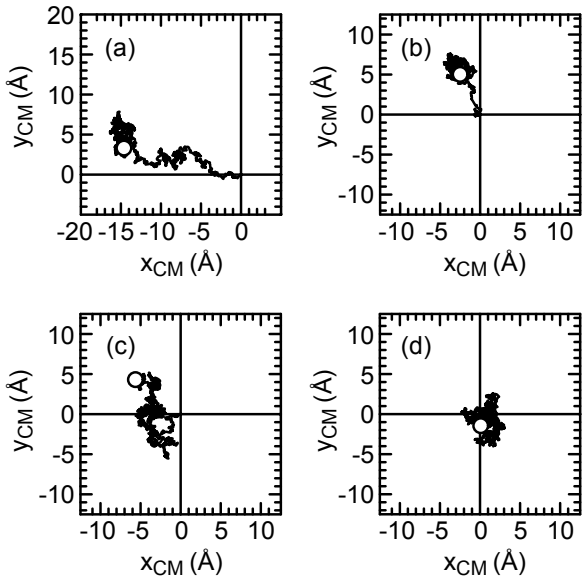

Figure 3.21: Same as Fig. 3.20 except for a phase separated monolayer with large domains. The four representative runs from Table 3.5 are (a) Run 1, (b) Run 2, (c) Run 3, and (d) Run 7.

increases while the contact angle remains the same. This continues until the edges of the drop encounter the interface between the polar and apolar regions. At this point the edges of droplet become pinned and as more fluid is added the base area remains the same while the contact angle increases (drop 2). Eventually the area of the liquid-vapor interface becomes so large that the free energy of the system is minimized when the edges of the droplet are located on the apolar area (drop 3). If the surface is ideal then this transition will be smooth.

A similar behavior is seen in the simulations where it is the volume of the drop that is constant and the size of the domains that is changing. Table 3.6 indicates that as the domain size increases the contact angle increases until the domain size becomes larger than the droplet size. This initial increase in θ comes about by the droplet decreasing its base area in order to cover hydrophilic domains while avoiding the hydrophobic background. This decrease in base area is accompanied by an increase in both the liquid-vapor interfacial area and the contact angle. Just as the free energy of the system was minimized by higher contact angles for the droplets in Fig. 3.1, the same is found here. As the domain size becomes larger than the droplet size the droplet simply moves to a hydrophilic domain where it assumes the contact angle that it would have were it on the pure surface.

Lundgren et al. [95] found a similar behavior to that in Table 3.6 for water droplets on surfaces composed of two materials. With the area fractions of the two materials being equal, the water contact angles was found to initially increase with the ratio of domain size to droplet size and then decrease when this ratio became large. This was found in all cases for square array patterns as well as stripes (Figs. 3 and 6 of Ref. [95]).

χ_p	Nanostructure	θ (°)
0.5	homogeneous	51.9
0.5	small domains	63.5
0.5	large domains	68.1
0.5	very large domains[a]	11.6

Table 3.6: A summary of the water contact angle on SAMs with the same overall composition but different degrees of mixing of the chains. [a]When the domain size is much larger than the droplet size the droplet is assumed to reside entirely on a hydrophilic domain.

3.4.4 Effect of Line Tension

When the size of a sessile drop approaches the microscale the Young equation must be modified to account for the line tension operating at the contact circle [132]. The modified Young equation is

$$\gamma_{SV} - \gamma_{SL} = \gamma \cos\theta + \frac{\tau}{r_B}, \tag{3.4}$$

where τ is the line tension. The line tension may be positive or negative and while theoretical calculations have estimated its order of magnitude to be 10^{-12} to 10^{-10} N, experimental values have ranged from 10^{-12} to 10^{-5} N [133]. A common experimental approach to estimate the line tension for solid-liquid-vapor systems is through the drop-size dependence of the contact angle as determined by goniometry or AFM measurements. Rearranging Eqn. 3.4 with the help of Eqn. 3.1 gives

$$\cos\theta = \cos\theta_\infty - \frac{\tau}{\gamma}\frac{1}{r_B}. \tag{3.5}$$

In Eqn. 3.5, θ_∞ is the macroscopic contact angle. According to Eqn. 3.5, a plot of $\cos\theta$ versus $1/r_B$ yields a line with a slope of $-\tau/\gamma$. If the line tension is taken as 10^{-11} N, $2r_B = 10$ nm, and $\gamma = 72$ mN/m then for $25^\circ \leq \theta_\infty \leq 150^\circ$ the difference between the microscopic and macroscopic contact angles is less than 3.6°. However, for the allowed values of θ_∞ outside of this interval, $\theta - \theta_\infty$ is as large as 13.5°. And this difference can become tens of degrees when τ is 10^{-10} N.

Preuss and Butt [79, 134] used the drop-size dependence of the contact angle to estimate the line tension of a water drop on a SAM composed of $CH_3(CH_2)_{10}SH$ and $HOCH_2(CH_2)_{10}SH$ to be 10^{-8} to 10^{-7} N. The quality of the SAMs used in these studies has been questioned [133]. Amirfazli et al. [135] found the line tension for heptane, octane, and nonane on a SAM composed on $CH_3(CH_2)_{15}SH$ and $HO_2C(CH2)_{15}SH$ to be positive and having an order of magnitude of 10^{-7} N. The two surface compositions considered were $\chi_c = 0$ and 0.12, where χ_c is the mole fraction of HO_2C-terminated chains in the monolayer. The authors also conducted AFM studies where it was shown that phase separation did not occur.

The line tension has proven to be a difficult quantity to calculate because it only manifests itself at small length scales. The conditions surrounding the experimental measurement of τ must satisfy several requirements in order for the data to be connected with theory. For instance, Eqns. 3.1 and 3.5 are only valid for a pure fluid in equilibrium with a solid that is atomically-smooth, rigid, homogeneous, and flat [132]. Furthermore, the effect of gravity must be negligible and the system must be free of contaminants such as surfactants. While such conditions are difficult to realize experimentally they are easily satisfied by molecular simulations. The downside of using a computer experiment is that they are limited to nanometer length scales and nanosecond time scales [120].

To estimate the line tension through the drop-size dependence of the contact angle, additional simulations for each homogeneous monolayer with $\chi_p \leq 0.75$ were carried out using 1000, 1500, 2000, 2500, and 3000 water molecules per drop. The monolayer with $\chi_p = 1$ was ignored because for the droplet sizes considered here the final heights of the droplets would be too small to reliably determine θ. To reliably determine the contact angle the droplet must have a bulk region of sufficient size. That is, the height of the droplet must be several angstroms larger than the sum of the liquid-vapor and solid-liquid interfacial thicknesses, which for water are roughly 3 Å [38] and 10 Å [40], respectively.

Many of the droplets for the simulations with $\chi_p = 0.5$ and 0.75 did not satisfy the criteria of height being larger than the interfacial thicknesses. For instance, the height of the droplet composed on 2500 molecules on the $\chi_p = 0.5$ monolayer was 18.4 Å. When the cosine of the contact angle was plotted versus $1/r_B$ for these cases the data was found to be scattered. For $\chi_p = 0.5$ and 0.75, the correlation coefficients were -0.16 and 0.42, respectively. The data for the monolayers with $\chi_p = 0$ and 0.25 are plotted in Fig. 3.22 along with the previous results for the water droplets composed of 4000 molecules and the best-fit line for each case. All droplets in these data sets had a bulk region of sufficient size with the droplet composed of 1000 molecules on the $\chi_p = 0.25$ monolayer having a height of 22.2 Å. The line tension, macroscopic and microscopic contact angles, and correlation coefficients, r, for the two monolayers are given in Table 7. The macroscopic contact angle is found by evaluating the best-fit line in the limit $1/r_B \to 0$. For both cases the order of magnitude of τ is consistent with theoretical predictions [133].

A block-averaging procedure was applied to compute a value of the contact angle for each 500 ps time interval over the last 1.5 ns of the simulation. The standard

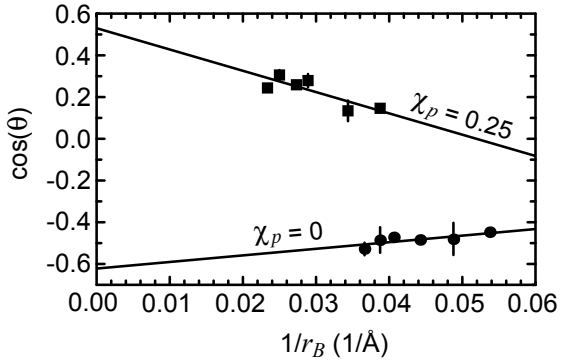

Figure 3.22: Cosine of the water contact angle versus inverse base radius for two choices of χ_p.

χ_p	τ (10^{-11} N)	θ_∞ (°)	θ (°)	r
0.00	-2.3	128.5	121.9	0.78
0.25	7.4	58.0	75.9	-0.84

Table 3.7: The line tension, macroscopic and microscopic water contact angles, and the correlation coefficient for homogeneous monolayers. θ is taken as the value for the water droplet composed of 4000 molecules.

deviation of the contact angle, $\sigma(\theta)$, was computed based on these values. We noted earlier that once equilibrium is reached the instantaneous value of z_{CM} deviates from its average by less than 1 or 2 Å. This is an indication that θ also changes very little with time. In fact, it can be seen from Figs. 3.14 and 3.22 that the values of $\sigma(\theta)$ are mostly smaller than the size of the symbols.

The radius of curvature of a sessile cylindrical droplet in the plane of the substrate is infinite. For this special case the line tension makes no contribution to the droplet profile, so the droplet assumes its macroscopic contact angle. For the methyl-terminated monolayer we conducted an additional simulation of a cylindrical droplet composed of 3000 molecules. The same simulation methodology for the spherical droplets was employed with the one difference being the value of L_y which was reduced to 34.43 Å to enforce the cylindrical shape. The contact angle for this case was found to be $117.7 \pm 5.7°$. This result differs from the value of 128.5° which was gotten by evaluating the best-fit line in the limit $1/r_B \to 0$.

Other molecular simulation studies of sessile droplets have computed the line tension [40, 136]. Using molecular dynamics simulations with the same interaction potential for water as the present study, Werder et al. [40] determined the line tension of water on graphite through the drop-size dependence of the contact angle. Different choices of the water-graphite interaction strength resulted in three different data sets. The authors computed the line tension for each set but the values they reported were a factor of ten larger than the correct values. This was apparently caused by confusion regarding the units of r_B in Table 2 of their work. The correct values are 0.7×10^{-11} N, 2.4×10^{-11} N, and 2.7×10^{-11} N. Using their data we have computed the correlation coefficients to be -0.81, -0.92, and -0.99, respectively. From this we see that our values of r for $\chi_p = 0$ and 0.25 are within the low end of

this range.

The correlation coefficients in Ref. [40] are higher than those in the present work for several reasons. First, Werder and coworkers used larger drop sizes with the number of molecules per drop varying from 1000 to 8379 (and 17,576 for one simulation). This ensures that the droplet height is much larger than the interfacial thicknesses and it leads to smaller values of $\sigma(\theta)$. Secondly, the atoms in the graphite substrate were kept fixed throughout the simulation whereas the chains composing our SAM, while anchored in place by the bottom two atoms, were free to move. Lastly, with a carbon-carbon bond length of 1.42 Å, the graphite lattice is more dense than the SAM which makes it smoother. The water-graphite system obeys more of the assumptions leading to Eqn. 3.4. This is why it gives nearly colinear data when the cosine of the contact angle is plotted against the inverse base radius.

Because of the uncertainty in our line tension data the microscopic contact angles from Table 3.2 have been reported in Fig. 3.14 in place of the macroscopic values. It is believed that reliable line tension data may be obtained for our water-SAM system if much larger drop sizes are considered. However, such simulations are computationally expensive because the required CPU time scales strongly with the base radius of the droplet.

3.5 Conclusions

Molecular dynamics simulations were conducted to investigate the wetting behavior of nanodroplets of water on binary self-assembled monolayers. The model introduced for the monolayer was found to give better agreement with experimental results when the bottom three atoms of the chains were kept fixed instead of only two. For the

homogeneous monolayers the water contact angle was found to agree with the experimental data for all compositions. The line tensions for the homogeneous monolayers with $\chi_p = 0$ and 0.25 were found to have an order of magnitude of 10^{-11} N. For the phase separated monolayers with an equimolar composition of CH_3- and $HOCH_2$-terminated chains, the water contact angle was found to depend of the domain size with the small and large domains yielding values of 63.5° and 68.1°, respectively. In both cases θ was found to be larger than that for the homogeneous monolayer at the same overall composition. Thus, the wetting behavior is influenced by the degree of mixing of the chains. This has important consequences for technological applications that depend on wetting behavior of SAMs at the nanoscale.

Chapter 4

Motion of a Nanodroplet of Pure Liquid on a Wetting Gradient

The dynamic behavior of a nanodroplet of a pure liquid on a wetting gradient was studied using molecular dynamics simulation. The spontaneous motion of the droplet is induced by a force imbalance at the contact line. We considered a Lennard-Jones system as well as water on a self-assembled monolayer (SAM). The motion of the droplet for the Lennard-Jones case was found to be steady with a simple power law describing its center-of-mass position with time. The behavior of the water droplet was found to depend on the uniformity of the wetting gradient, which was composed of methyl- and hydroxyl-terminated alkylthiolate chains on Au(111). When the gradient was non-uniform the droplet was found to become pinned at an intermediate position. However, a uniform gradient with the same overall strength was found to drive a droplet consisting of 2000 water molecules a distance of 25 nm or nearly ten times its initial base radius in tens of nanoseconds. A similar result was obtained for a droplet that was twice as large. Despite the many differences

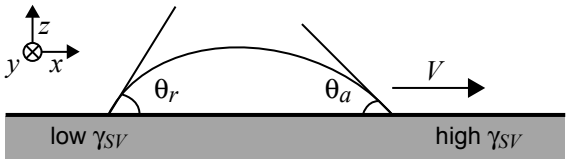

Figure 4.1: Side view of a liquid drop on a wetting gradient with $\theta_a < \theta_r$, where θ_a and θ_r are the advancing and receding contact angles, respectively. On a surface where contact angle hysteresis is negligible a drop of any size will move in the direction of increasing γ_{SV}.

between the Lennard-Jones and water-SAM systems, the two show a similar overall behavior for the motion. Fair agreement was seen between the simulation results for the water droplet speed and the theoretical predictions. When the driving force was corrected for contact angle hysteresis the agreement was seen to improve.

J. Koplik is responsible for the Lennard-Jones results and the corresponding discussion in this chapter.

4.1 Introduction

Pressure gradients or gravity are commonly used to drive liquids through pipes and tubes at human length scales, but the driving force required increases very rapidly when the size is reduced. Current interest in micro and nanofluidic devices motivates research into alternatives. As illustrated in Fig. 4.1, one alternative for the transport of fluids at the nanoscale is a gradient in substrate surface energy, whereby intermolecular interactions draw the liquid molecules along the solid.

The motion of a liquid drop on a wetting gradient was first studied by Greenspan [137]. Later, the theoretical description was independently worked on by Brochard [138] who also considered motion due to a temperature gradient. Chaudhury and

Whitesides [139] were the first to realize the phenomenon in the laboratory. The gradient in this case was formed by following a procedure introduced by Elwing et al. [140] where a silk thread saturated with decyltrichlorosilane is suspended in the vicinity of a silicon wafer. With the substrate tilted by 15° to the horizontal it was shown that a 1 to 2 μL water droplet would migrate up the inclined solid against gravity with a velocity of 1 to 2 mm/s. Ford and Nadim [141] provided a theoretical study of the motion of a cylindrical ridge of arbitrary shape due to a temperature gradient. Marangoni forces, which do not play a role in the motion of a drop on a wetting gradient, do become important when a thermal gradient is present. As experiments have shown the droplet moves towards the cooler end of the gradient. In this work we consider isothermal systems only.

Daniel et al. allowed droplets from saturated steam to condense on a radial wetting gradient [142]. Small water droplets were found to migrate in the direction of increasing wettability with velocities that were two to three orders of magnitude larger than previously reported in Marangoni flows. When the steam was replaced with air, droplets 1 to 2 mm in size were found to give speeds of 2 to 3 mm/s, which is similar to previous findings [138, 139, 143].

Given sufficient time a drop of any size should move on a wetting gradient. However, this is not observed for a surface which exhibits contact angle hysteresis. Experimentally it has been shown that a drop must be greater than some critical size before it will move. Daniel and Chaudhury [144] worked out an expression for the force due to contact angle hysteresis based on the work of Brochard [138]. Their experiments with ethylene glycol on an alkylsilane substrate prepared in the same manner as previous experimental efforts showed that droplets no longer move when their base radius falls below a threshold value. It is demonstrated that in-plane

vibration can help overcome the force due to hysteresis. Drop velocities increase from 1–2 mm/s to 5–10 mm/s when a speaker is attached to the substrate. The enhanced velocities due to in-plane vibration were examined further for five different liquids including water [145].

Suda and Yamada [146] calculated the unbalanced Young force acting on the drop by extracting the advancing and receding contact angles from video frames. The same force was determined by a second method where a glass microneedle was inserted into the droplet and the force was related to the deflection of the needle. The two were found to be in good agreement. Based on their findings a new expression for the hydrodynamic drag force was proposed.

Early works relied on the vapor-diffusion controlled procedure of Elwing et al. [140] to prepare the wetting gradient. Later, Ito et al. [147] used photodegradation of an alkylsilane SAM to achieve the gradient. Gradients of different strength were prepared by varying the intensity and time of photoirradiation. For the various gradient strengths considered, 2 μL water droplets were found to migrate with average velocities of 1–7 mm/s. Photoirradiation was also used by Ichimura et al. [143] on a photoisomerizable monolayer. This allowed for the direction and strength of the gradient to be changed reversibly. Contact angle hysteresis prevented water and other materials from moving on the gradient. Olive oil and liquid crystal systems were shown to traverse the gradient, however.

Subramanian et al. [148] derived two expressions for the hydrodynamic drag force experienced by a spherical-cap droplet on a gradient of wettability. The first is based on a simplified result of Cox [149] where it is assumed that the drop may be treated as a collection of wedges. The second uses lubrication theory while retaining the spherical-cap shape of the drop in the integration of the shear stress over the contact

area. The two expressions for the force give similar results for small contact angles and small values of the ratio of the slip length to base radius of the drop. These expressions were then used to describe the velocity of the drop which was compared to experimental data for tetraethylene glycol. In the experiments [150], droplets of several sizes were considered on the 1 cm gradient. The two expressions were found to overestimate the quasi-steady velocity. When contact angle hysteresis was taken into account the agreement was much better. This was the first experimental work to report results on the speed of the drop as a function of position along the gradient.

Aqueous droplets containing amphiphilic species may be driven on hydrophilic tracks embedded in a hydrophobic background by the covalent [151] or noncovalent [152] adsorption of the amphiphiles at the rear edge of the droplet. Here velocities of mm/s are observed on tracks that are typically a few millimeters wide. The noncovalent approach or reactive wetting has been studied by the lattice Boltzmann technique [153].

Zhang and Han [154] induced the motion of a pure fluid by using a strip of hydrophilic material of spatially uniform surface energy embedded in a background of hydrophobic material. The shape of the strip was tailored to optimize the speed of the spreading front. Using mica embedded in low-density polyethylene the average spreading velocity was found to be 6.8 cm/s when the substrate was arranged horizontally.

The wetting gradients in this work are composed of self-assembled monolayers with mixed terminal functionality. SAMs have received much attention in recent years because they are simple to prepare and provide well-ordered, dense monolayers at full coverage, which allows for the control of surface properties [155, 156, 62, 157].

The most studied case is the adsorption of alkanethiols on Au(111). The reported structure of such systems has changed many times over the years [102, 103, 158] and is still being refined [159]. Recently, Riposan and Liu [117], based on their scanning tunneling microscopy results and the computer simulation results of Li et al. [113], have proposed a structural model for undecanethiol on Au(111). A modified version of this new model is used for the present study.

There have been a number of recent simulation studies of pure fluids on heterogeneous substrates. Adão et al. [96] looked at the spreading of a Lennard-Jones droplet on a regular square array of alternating solvophobic and solvophilic patches. Lundgren et al. [95] examined a similar substrate pattern but with nanodroplets of water. Ultrahydrophobic surfaces were also investigated in this study. Dupuis and Yeomans [160] have conducted lattice Boltzmann simulations to study the wetting of patterned surfaces. Grest et al. [161] have simulated the spreading of short chain polymer droplets on substrates with alternating strips of wetting and non-wetting material. And Halverson et al. [162] have studied the wetting behavior of water droplets on phase separated SAMs.

4.1.1 Theory

The driving force for the motion of a droplet on a wetting gradient is the unbalance of surface forces at the contact line or the Young force. In this work we consider either a highly distorted spherical droplet placed atop a wetting strip or a cylindrical cap droplet whose shape is maintained by periodicity in the tranverse direction. In the latter case, with reference to Fig. 4.1, the driving force on a ridge in the x-direction per unit length in the y-direction is

$$F^{(Y)} = \gamma[\cos\theta_e(x_a) - \cos\theta_e(x_r)], \tag{4.1}$$

where $\theta_e(x_a)$ and $\theta_e(x_r)$ are the equilibrium contact angles at the advancing and receding edges, respectively, and γ is the liquid-vapor interfacial tension. This expression ignores contact angle hysteresis.

The driving force is opposed by the hydrodynamic resistance acting on the fluid due to the solid substrate. This force has been derived using various simplifying assumptions and for different droplet geometries. For a ridge, Brochard [138] using lubrication theory has found an expression for the drag force in the x-direction per unit length in the y-direction (Eqn. 21 of the original work):

$$F^{(h)} = 6\mu\frac{V}{\theta_0}\ln\left(\frac{x_{max}}{x_{min}}\right), \tag{4.2}$$

where μ is the fluid viscosity, V is the velocity, x_{max} is half the base radius of the ridge, and x_{min} is a molecular size (which enters as a cutoff in the calculation). In Eqn. 4.2, θ_0 is an average dynamic contact angle given by

$$2\cos\theta_0 = \cos\theta_e(x_a) + \cos\theta_e(x_r). \tag{4.3}$$

Eqns. 4.1 through 4.3 lead to the quasi-steady velocity of the drop. Inertial effects will be shown to be negligible.

4.2 Simulation Methodology

We consider two different cases involving droplet motion on a wetting gradient, first a generic Lennard-Jones system with simple short-ranged interactions, and second an aqueous system based on realistic interactions and experimentally realizable materials. The first case in addition involves a somewhat complicated drop configuration (and in fact was originally carried out for another purpose), while the geometry of the aqueous system allows us to focus cleanly on the effects of the wetting gradient. The reason both simulations are presented here is that we observe strong similarities in their behavior, suggesting that our results have broad applicability beyond the particular materials considered.

4.2.1 Lennard-Jones System

The wetting gradient here is applied to a linear strip of wetting atoms extending down the middle of a non-wetting background on a periodic planar substrate. The substrate is a single layer of fcc unit cells (two atomic layers) of density $0.9\sigma^{-3}$ and dimensions $80.56\sigma \times 499.8\sigma$, and the wetting region is half as wide, and extends along the full length. A liquid drop of 16,704 molecules in the form of four-atom flexible chains is placed atop the wetting strip and allowed to move. All atoms interact via a Lennard-Jones potential,

$$U_{\mathrm{LJ}}(r) = 4\epsilon\left[\left(\frac{\sigma}{r}\right)^{12} - \left(\frac{\sigma}{r}\right)^{6}\right], \tag{4.4}$$

with a cut off at 2.5σ and shifted by a linear term adjusted so that the force vanishes at the cutoff. The coefficient c_{ij} varies the attractive interaction between atomic species i and j, and has the standard unit value for the fluid-fluid and solid-solid

cases. The interaction between non-wetting solid and fluid has c=0, and for wetting solid and fluid c varies linearly between 0.75 and 2.0 along the length of the substrate. In addition, a FENE interaction acts between adjacent atoms in a chain to bind them into molecules. The motivation for a molecular rather than a monatomic liquid is to sharpen the liquid-vapor interface, which would be rather diffuse in the latter case. The same molecular model has been used in an earlier study of pearling instabilities in nanoscale flow on patterned surfaces and further details may be found in [163].

In the simulations, the atoms composing the drop are initially placed on solid lattice sites within a rectangular box sitting atop the low-c end of the wetting strip, and the temperature is ramped up from 0.1 to $1.0\epsilon/k_B$ over a 500τ interval, using velocity rescaling. (Here, $\tau = \sigma(m/\epsilon)^{1/2}$, where m is the atomic mass, is the natural time unit for the simulations.) At this stage, the drop has melted into a rounded box shape (Fig. 4.4a). The temperature is subsequently fixed at 1.0 for the remainder of the simulation by a Nosé-Hoover thermostat.

4.2.2 Water-SAM System

The wetting gradient is composed of 90 chains in the axial or x-direction and 8 chains in the transverse or y-direction. Two different gradients are considered and while both are composed of the same number of CH_3- and $HOCH_2$-terminated chains one is more uniform than the other.

The details of our SAM model and its predictions have been described in Ref. [162] and will only be discussed briefly. The structure of the chains is based on the model proposed by Riposan and Liu [117]. We adopt the model for Phase B of their work where the monolayer forms a $(4\sqrt{3} \times 2\sqrt{3})$R30° lattice or c(4×2) superlattice. The sulfur atoms are located in the triple-hollow sites where they form a triangular

lattice with a nearest-neighbor spacing of 4.97 Å. With reference to Fig. 4.2, each of the four chains per unit cell have the same tilt angle ($\theta = 30°$) and direction of tilt ($\chi = 15°$). The individual twist angles are different.

The wetting properties of SAMs composed of alkanethiols become independent of chain length when the number of methylene groups in the chain becomes large [68, 118]. Because of this and to reduce computation time, we only consider eight or ten atomic layers (depending on the terminal group of the chain) and ignore the remaining methylene groups, sulfur atoms, and gold lattice. Since the overall structure of pure SAMs composed of alkanethiols with either CH_3 or OH terminal groups have been shown to be similar [106, 119] we assume our model holds for both chains. Methyl and methylene groups are treated as united atoms while the oxygen and hydrogen atoms of the hydroxyl group are treated atomically. This means that methyl-terminated chains are composed of eight atomic units or $CH_3(CH_2)_7-$ while $HOCH_2$-terminated chains or $HOCH_2(CH_2)_7-$ are composed of ten. The bottom two atomic layers of each chain are fixed throughout the simulation. This keeps the self-assembled monolayer in place and helps impose the proper structure on the chains. A one-dimensional wetting gradient is created by varying the surface concentration of hydroxyl-terminated chains in the x-direction. The hydroxyl surface concentration varies linearly with position over a distance of roughly 35 nm. The magnitude of the gradient is 1.4×10^{-4} OH/Å or, based on our measurements of the water contact angle, 3.2°/nm.

The motion of water droplets consisting of 2000 and 4000 molecules was examined on the two different wetting gradients. The droplets were constructed by extracting hemicylindrical shapes from a large simple cubic lattice of randomly-orientated water molecules arranged at ambient liquid density. The hemicylindrical droplets

were placed on the hydrophobic end of the wetting gradient at initialization. Conjugate gradient energy minimization was performed for 10,000 steps. The molecular dynamics simulations [120] were carried out with the number of molecules, the system volume, and the temperature held constant using the third-party code NAMD [121]. The temperature was maintained at 298.15 K by applying a Langevin thermostat, with a damping coefficient of 0.5 ps^{-1}, to non-hydrogen atoms. The Verlet method was used to perform the numerical integration of the equations of motion for the monolayer while SETTLE [59] was used for water. A timestep of 1 fs was used. All bond lengths in the monolayer were kept fixed using SHAKE [56]. The SPC/E interaction potential [54] was used for water while the OPLS-UA force field [122, 123] was used for the monolayer (see Table 3.1). The OPLS combining rules were used for water-monolayer interactions. The interactions between atoms in the same monolayer chain separated by three or fewer bonds were excluded. Short-range interactions were cutoff at 12 Å with a switching function applied for separations greater than 10 Å. The dimensions of the simulation cell were L_x = 447.30 Å, L_y = 34.43 Å, and L_z = 173.49 Å. Periodic boundary conditions in three dimensions were used. The PME technique [124, 125] was used to account for long-range interactions with the smallest number of grid points per direction being 0.90 $Å^{-1}$. The simulations were carried out on DataStar at the San Diego Supercomputer Center. Using eighteen IBM p655 nodes or 144 processors the simulations ran at roughly 14 ms/step.

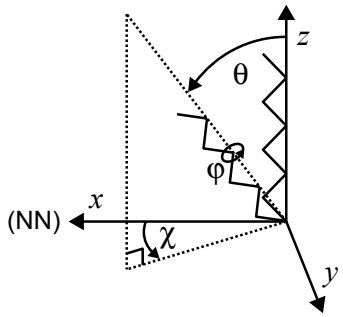

Figure 4.2: The orientation of each chain in the monolayer is described by a tilt angle (θ), a direction of tilt (χ), and a twist angle about the molecular axis (φ). This diagram shows a methyl-terminated chain with its eight atomic units. The x-direction corresponds to a nearest-neighbor (NN) direction.

4.3 Results and Discussion

4.3.1 Lennard-Jones System

The Lennard-Jones droplet began as a rectangular arrangement of atoms at the low-c end of the wetting gradient. During the first 600τ of the simulation the droplet is found to rearrange itself into a spherical cap form (Fig. 4.4a,b) with little change in the center-of-mass position. Afterwards the drop moves continuously towards the high-c end of the strip, and its shape becomes increasingly asymmetric (Figs. 4.4c,d), reflecting the decrease in equilibrium contact angle along the gradient. The variation of center-of-mass position with time, shown in Fig. 4.3, is a simple power law after rearrangement, $x_{\mathrm{CM}}(t) \sim t^n$ with $n = 0.42 \pm 0.01$. After $12.5 \times 10^4\tau$ the center-of-mass of the droplet has moved 110σ in the x-direction. The simulation was terminated at this point since there were no qualitative changes in the drop's behavior.

The shape of the droplet is neither spherical nor cylindrical. It has a shape similar to the drops found in the molecular adsorption studies [151, 152], which were

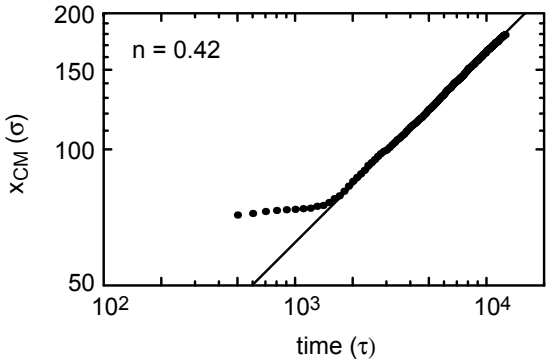

Figure 4.3: A log-log plot of the axial component of the center-of-mass position versus time for a Lennard-Jones droplet on a wetting gradient. The coefficient and exponent of the power law fit are $c_{LJ} = 3.37\sigma\tau^{-0.42}$ and $n_{LJ} = 0.42$, respectively.

carried out on rectilinear tracks embedded in a non-wetting background. Because of its irregular shape the droplet does not lend itself to a simple theoretical analysis, which we therefore postpone to the second case below.

For comparison to the water drop results below, we estimate the relevant dimensionless hydrodynamic parameters describing the flow. At time 2500τ when the drop shape is very roughly a spherical cap, the radius $R \approx 40\sigma$ and the velocity $V \approx 0.015\sigma/\tau$. From [33], the fluid's density, viscosity and surface tension are $\rho = 0.79\sigma^{-3}$, $\mu = 3.6m/(\sigma\tau)$ and $\gamma = 0.46\epsilon/\sigma^2$, respectively, where all quantities are given in units derived from the Lenanrd-Jones potential. The resulting Reynolds number is $Re = \rho VR/\mu \approx 2.7$, the capillary number is $Ca = \mu V/\gamma \approx 0.12$ and the Bond number is $Bo = \rho R^2 g/\sigma \approx 2 \times 10^{-10}$. The first two numbers decrease as $t^{-0.58}$ as the simulation proceeds and the drop slows.

4.3.2 Water-SAM System

The motion of water nanodroplets of different size (2000 and 4000 molecules) was investigated on a non-uniform and uniform wetting gradient. The hydroxyl number

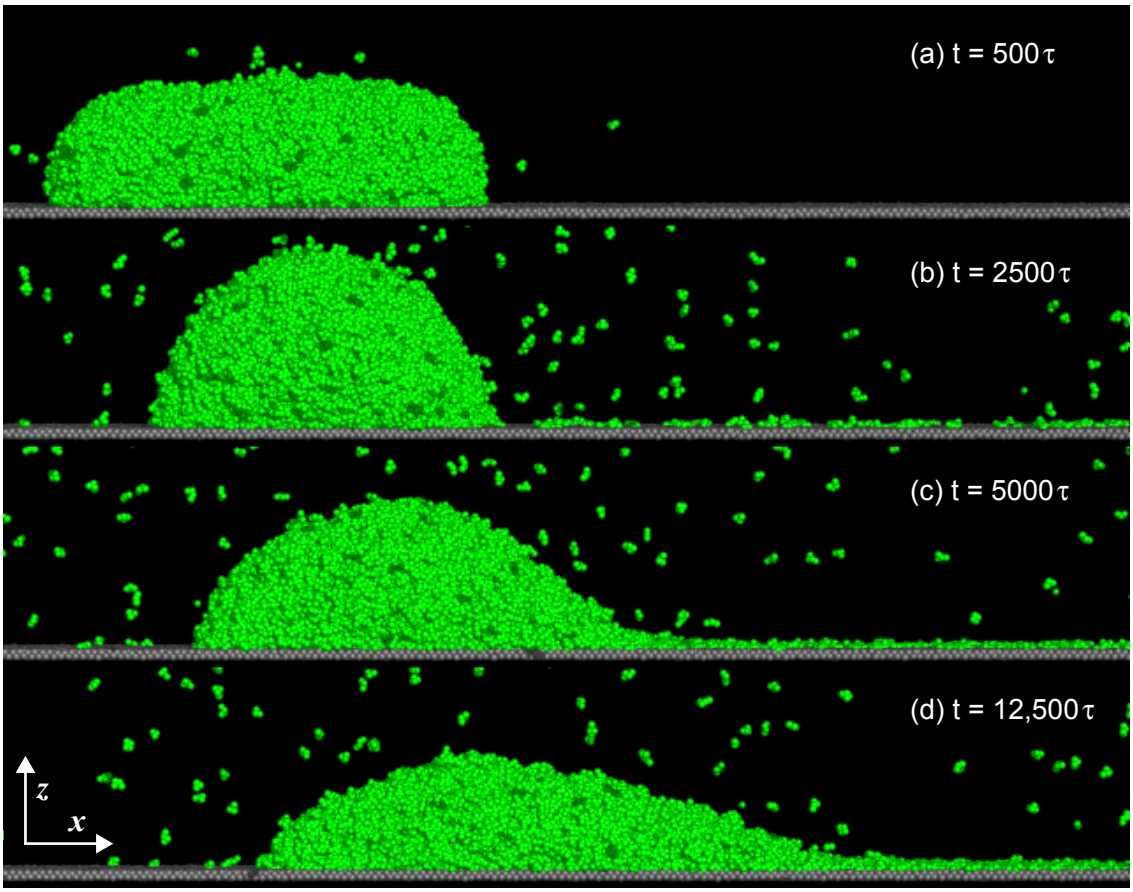

Figure 4.4: Side views of a Lennard-Jones droplet at different times on a wetting gradient.

density along each gradient is shown in Fig. 4.5. The magnitude of each gradient is the same.

Non-Uniform Gradient

For the non-uniform case, a droplet consisting of 2000 water molecules was found to proceed along the gradient for 50 Å until the advancing edge of the droplet encountered a large patch of methyl-terminated chains at $x = 160$ Å. This patch corresponds to a sharp decrease in the OH number density in Fig. 4.5(a). The center-of-mass of the nanodroplet is plotted as a function of time in Fig. 4.6(a). The center-of-mass and base length of the drop at this point were $x_{CM} = 120$ Å and $l_b = 60$ Å, respectively. After becoming pinned the simulation was continued for an additional 4 ns. In that time the droplet did not pass the hydrophobic barrier. A second interpretation of the droplet becoming pinned is that due to the non-uniformity of the gradient the local γ_{SV} at the advancing and receding edges of the droplet were approximately the same. In such a case the droplet would have similar θ_a and θ_r and this would give a zero driving force as suggested by Eqn. 4.1.

The droplet consisting of 4000 water molecules showed a similar behavior on the same non-uniform gradient. Its center-of-mass increased during the first 8 ns of the simulation before reaching a constant value of 160 Å for the final 4 ns. The hydrophobic patch that the droplet could not pass is located just beyond $x = 200$ Å. The base length of the droplet was approximately 85 Å. In general, a larger droplet will experience a larger driving force as can be seen from Eqn. 4.1. This might explain why the larger droplet was able to pass the hydrophobic patch at $x = 160$ Å while the smaller droplet could not.

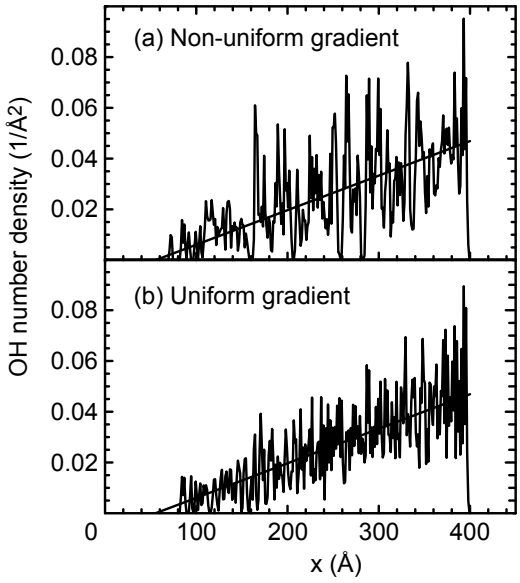

Figure 4.5: The number density of hydroxyl groups as a function of position along the gradient is shown for the (a) non-uniform gradient and (b) uniform gradient. The line running through the data in both plots is the ideal or target gradient.

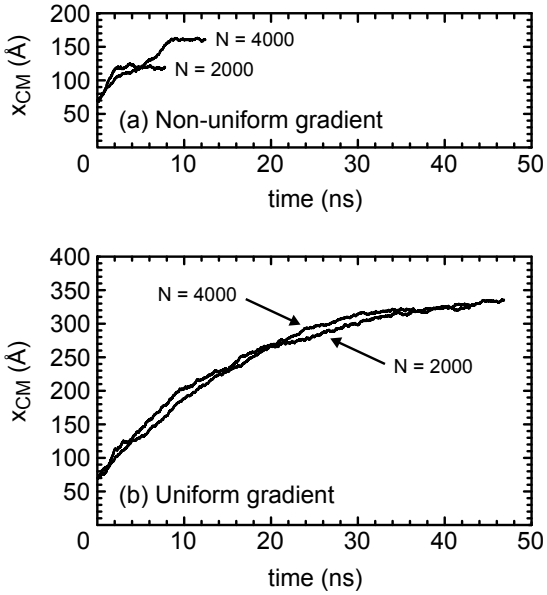

Figure 4.6: The axial component of the center-of-mass position is shown for two different size water droplets on the (a) non-uniform gradient and (b) uniform gradient.

Uniform Gradient

A second set of simulations was conducted on a uniform gradient with the same overall strength as the non-uniform gradient. Fig. 4.5 shows that the OH number density varies more smoothly in this case. On the uniform gradient the small and large water droplets were found to move all the way from the hydrophobic to the hydrophilic end. The axial component of the center-of-mass position is shown as function of time in Fig. 4.6(b) for the two droplet sizes. It can be seen that both size droplets move with approximately the same speed. While the average center-of-mass motion of the drops is continuous, thermal fluctuations give rise to slight positive and negative local displacements.

A time sequence of configurations for the $N = 2000$ water droplet on the uniform gradient is shown in Fig. 4.7. At $t = 0$ the droplet is placed at the hydrophobic end of the gradient where the advancing and receding contact angles are both greater than 90°. At $t = 7.5$ ns the droplet has advanced about 100 Å and θ_a and θ_r have both decreased. Fig. 4.7(c) shows a snapshot at $t = 15.0$ ns where the advancing contact angle is less than the receding contact angle. This behavior is not seen in every snapshot because thermal fluctuations are large and the droplet shape is often distorted as in Fig. 4.7(b). However, a time-average of the liquid-vapor profile as shown in Fig. 4.9(a) reveals that θ_a is indeed less than θ_r in 4.7(b). It can also be seen that the base length of the ridge broadens with time. The droplet traverses the gradient in roughly 45 ns. The number density of hydroxyl groups goes abruptly to zero at the end of the hydrophilic region. This explains why the droplet has a larger contact angle at the front rather than the rear in the last snapshot of the sequence.

It can be seen from Fig. 4.7(d) that a small number of molecules have detached from the droplet and assumed positions in the intermediate region of the gradient.

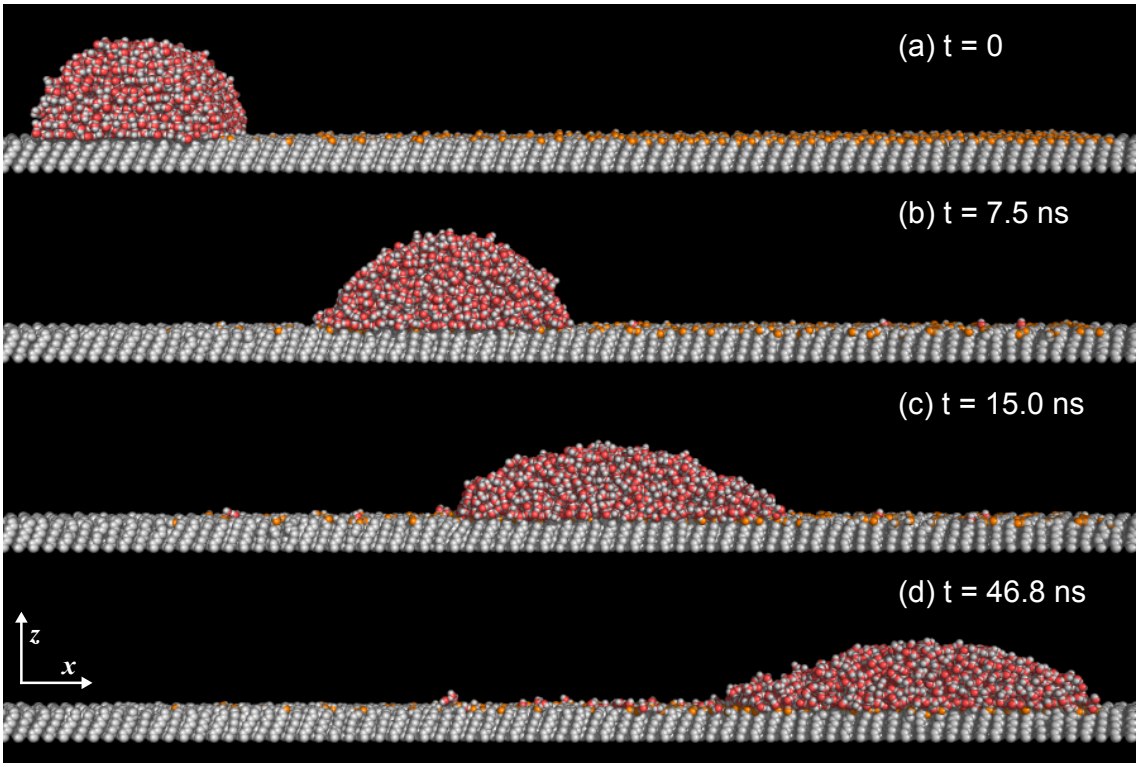

Figure 4.7: Side views of the $N = 2000$ water nanodroplet at different times on a uniform wetting gradient. (a) The droplet is initialized with a hemicylindrical shape at the hydrophobic end. Intermediate configurations are shown in (b) and (c) with the final configuration in (d). The water molecules are shown with oxygen colored red and hydrogen in white, while the substrate is shown with methyl and methylene groups as gray, oxygen as orange, and hydrogen as white.

These water molecules are hydrogen-bonding with each other and the hydroxyl-terminated chains in the monolayer. Since these molecules have fewer hydrogen bonds on average than the molecules in the main droplet it is expected that many will recombine with the main droplet at later times. A smaller number of satellite molecules was observed in the case of the larger droplet.

To evaluate the relative importance of different forces we compute various dimensionless groups using the following values: $\gamma = 72$ mN/m, $\mu = 1$ mPa s, $\rho = 10^3$ kg/m^3, $g = 9.8$ m/s^2, $V = 1$ m/s, and $R = 10^{-8}$ m. The capillary number is $\mathrm{Ca} = \mu V/\gamma \approx 10^{-2}$. The Bond number is $\mathrm{Bo} = \rho g R^2/\gamma \approx 10^{-11}$. The small values of the Ca and Bo number suggest that gravity is unimportant and that the droplet shape is dominated by surface forces and not the motion. This analysis does not account for the role of thermal fluctuations. The Reynolds number is $\mathrm{Re} = \rho V R/\mu \approx 10^{-2}$. The small value of Re justifies the use of the Stokes equations as the starting point for the derivation of the drag force.

As was done for the Lennard-Jones case, we fit the center-of-mass position data to a simple power law, $x_{CM} = ct^n$, for the uniform gradient cases. This data is shown on a log-log plot in Fig. 4.8. The values of n have been determined to be 0.39 and 0.48 for the small and large droplets, respectively, with the coefficients being $c = 81.6$ Å ns$^{-0.39}$ and 61.6 Å ns$^{-0.48}$. For the Lennard-Jones simulation we found $n = 0.42$ (see Fig. 4.3). Despite the many differences between the Lennard-Jones and water-SAM systems such as the presence of long-range forces and hydrogen-bonding in the water-SAM case, the two systems exhibit a similar overall behavior for the motion.

To determine the shape of the droplet at time t the time-averaged fluid density field is found. Space is divided into non-overlapping rectangular slabs with dimensions $\Delta x = 3.0$ Å, $\Delta y = L_y$, and $\Delta z = 0.5$ Å. Water molecules from each

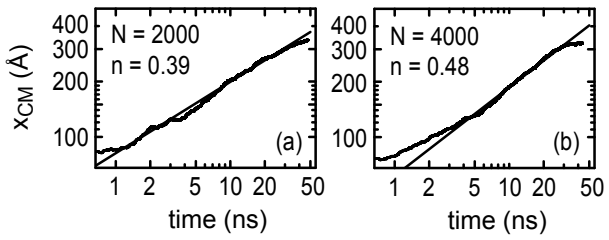

Figure 4.8: The center-of-mass position versus time on a log-log plot for water droplets on a uniform wetting gradient with (a) $N = 2000$ and (b) $N = 4000$ molecules per drop. The lines are the power law fits to the data between 5 and 35 ns.

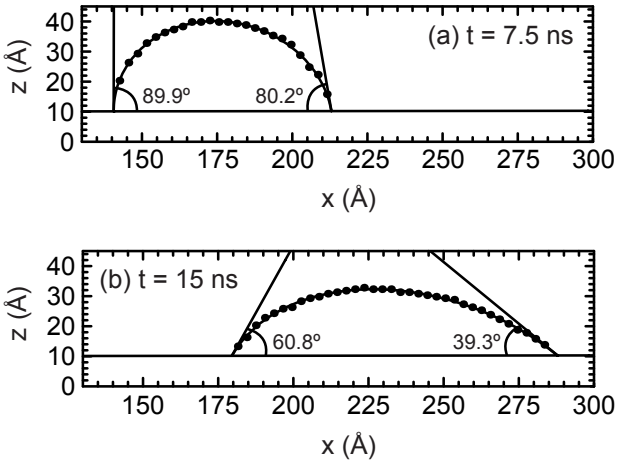

Figure 4.9: Best-fit ellipses to the liquid-vapor boundary profile data at (a) $t = 7.5$ ns and (b) $t = 15.0$ for the $N = 2000$ water droplet on a uniform wetting gradient. The horizontal line at approximately $z = 10$ Å is the total height of the monolayer which increases gently in the positive x-direction. The bottom layer of fixed atoms is at $z = 0$. The tangent lines at the advancing and receding edges of the drop are shown. The best-fit parameters are (a) $x_0 = 177.0$ Å, $z_0 = 7.7$ Å, $a = 36.8$ Å, $b = 32.0$ Å, and $\psi = 0.291$ and (b) $x_0 = 243.3$ Å, $z_0 = -18.8$ Å, $a = 70.2$ Å, $b = 47.9$ Å, and $\psi = 0.353$.

configuration are individually assigned to a slab based on their center-of-mass positions. Once the density field has been calculated for a given time interval, the vapor-liquid boundary is found by determining the position of the first bin in the z-direction for each x-slab where the water density falls to one-half of its bulk value. The data points $\{x_i, z_i\}$ are then fit to an ellipse using a nonlinear fitting routine (see Appendix B for details). The contact angles, positions of the edges, and base length are then straightforwardly determined. Fig. 4.9 shows the profile data points and the best-fit ellipse at $t = 7.5$ ns and 15 ns for the small droplet.

Because the droplet is constantly moving down the gradient care must be taken in performing the time-average. Fig. 4.6b suggests that the maximum velocity of either size droplet is roughly 50 Å/ns or 0.05 Å/ps. In finding the profile at time t we consider configurations from $t \pm 100$ ps in the averaging. This gives a worst case scenario difference in x_{CM} of (100 ps)(0.05 Å/ps) = 5 Å in each direction. For most profiles the difference is closer to 1 Å. In an attempt to remove the small effect of droplet translation from the average, the center-of-mass of each configuration is shifted to that at time t. Since configurations are stored every 5 ps a total of forty-one configurations are considered per profile.

The height of the monolayer increases slightly in the direction of increasing hydroxyl concentration. Methyl-terminated chains are found to give a total monolayer height of 10.03 Å while alcohol-terminated chains give 10.41 Å. Because the determination of the contact angle is a sensitive measurement the change in height is taken into account by assuming that it varies linearly between the two ends.

Fig. 4.10 shows the base length of the droplets as a function of time. The base length is defined as the difference between the positions of the advancing and receding edges. The base length increases with time because at greater axial positions

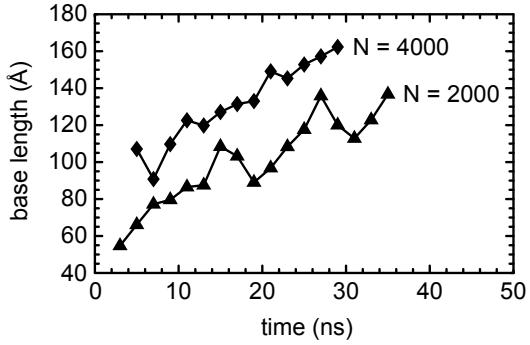

Figure 4.10: The base length of a cylindrical-cap water droplet on a uniform wetting gradient as a function of time. The lines are drawn to guide the eye.

the droplet interacts with a substrate having an effectively higher γ_{SV}. Greater variability is seen for the $N = 2000$ water droplet. Its base length undergoes two contractions with the first terminating at $t = 19$ ns and the second at $t = 31$ ns. The contraction between 15 and 19 ns is due to the advancing edge becoming slowed by a region of elevated hydrophobicity at $x = 305$ Å. During this time period the receding edge increases by 40.6 Å while the advancing edge by only 21.2 Å. Fig. 4.11 shows the advancing and receding contact angles as a function of time for both droplet sizes. The difference between θ_a and θ_r at $t = 19$ ns is only 6.2° whereas at $t = 15$ ns it is 21.5°. The second dramatic reduction of the base length is due to a series of events occurring between 19 and 31 ns. From 19 to 27 ns the receding edge of the droplet is pinned at $x = 222$ Å. During this period the advancing edge increases by 50.3 Å which leads to a rapid increase in the base length. The advancing edge then becomes pinned from 27 to 31 ns at $x = 365$ Å while the receding edge passes the hydrophobic barrier at $x = 222$ Å and increases by 27.7 Å. This explanation is consistent with the behavior of the dynamic contact angles shown in Fig. 4.11. The receding edge then becomes pinned at $x = 250$ Å between 31 and 35 ns. The base

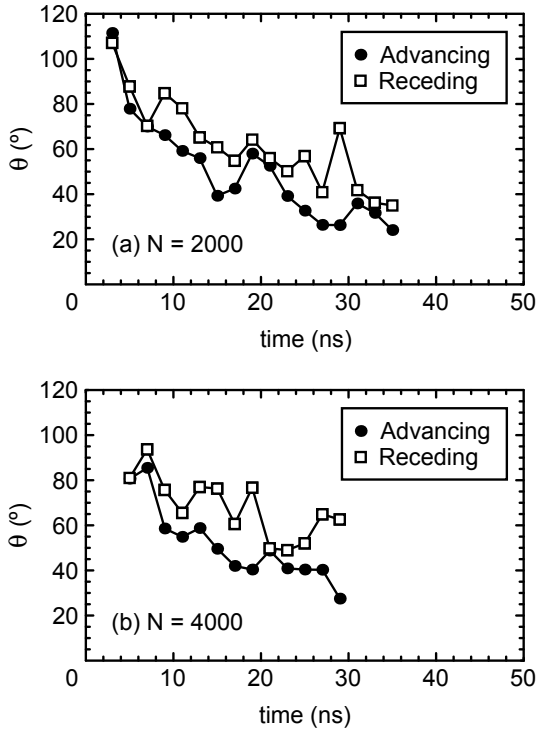

Figure 4.11: Advancing and receding contact angles as a function of time for (a) $N = 2000$ and (b) $N = 4000$ water molecules per drop. The lines are drawn to guide the eye.

length of the larger droplet is seen to increase much more steadily. This might be explained by the increased driving force.

The measurements of the advancing and receding contact angles were made every 2 ns. Fig. 4.11 indicates that, in general, θ_a is less than θ_r at t. The average difference between the cosine of the advancing and receding angles (i.e., $\cos\theta_a - \cos\theta_r$) is 0.18 for the smaller droplet and 0.24 for the larger droplet. This is expected since the larger droplet has a larger base length and therefore its leading and rear edges experience a greater difference in the hydroxyl surface concentration.

Several authors have shown that contact angle hysteresis plays an important role in determining the motion of the droplet [139, 142, 144, 150]. Hysteresis in

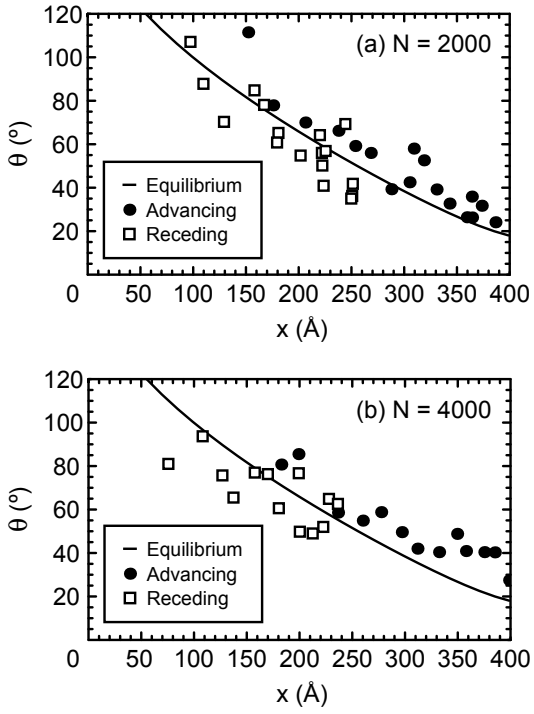

Figure 4.12: Advancing and receding contact angles as a function of position along the gradient for the (a) $N = 2000$ and (b) $N = 4000$ water molecule droplet. The angles were measured by fitting each time-averaged droplet profile to an ellipse. The data were calculated for the smaller droplet every 2 ns from 3 to 35 ns and for the larger droplet every 2 ns from 5 to 29 ns. $\theta_e(x)$ is given by the solid curve.

the contact angle may be probed by examining θ_a and θ_r as a function of position along the gradient. On an ideal surface the advancing and receding contact angles are the same at all locations. Fig. 4.12 shows θ_a and θ_r as a function of position for the two droplet sizes. The solid curve in the figure gives the equilibrium contact angle θ_e, which was taken from our previous work [162]. In general, we find $\theta_r(x) < \theta_e(x) < \theta_a(x)$, which indicates the presence of contact angle hysteresis. It is difficult to be precise about the extent of hysteresis because of the scatter in the data. Since the measurements were made uniformly in time, clusters of overlapping symbols are indicative of pinning. For θ_r this occurs at $x = 222$ Å and 250 Å and for θ_a this occurs at $x = 365$ Å. These observations are consistent with the data in Figs. 4.10 and 4.11.

For macroscopic systems hysteresis in the contact angle is commonly caused by contaminants, substrate roughness, or a substrate that is chemically heterogeneous. Since contaminants are not present in the molecular systems considered here the origin of hysteresis must be related to the fluid-substrate interaction. The nearest-neighbor separation distance in the monolayer is 4.97 Å while the length of an OH bond in water is only 1 Å. The droplet edge which is composed of only tens of water molecules sees the self-assembled monolayer as chemically and topologically heterogeneous. As Fig. 4.5 indicates, the surface concentration of the hydroxyl-terminated chains (which are arranged non-uniformly in both the x- and y-directions) only appears to follow the target value of the gradient when averaged over several nanometers. This has important consequences when the advancing and receding contact angles are measured at the same location on the gradient. With reference to Fig. 4.1, when θ_a is measured at position x_0 the droplet is at lesser x while for the measurement of θ_r at the same position the droplet is at greater x.

Because of this the droplet edges at x_0 see different regions of the substrate and this leads to a different balance of forces at the contact line or a different contact angle. If the simulations were conducted with the substrate modeled as a continuum (using a Steele potential) it is expected that the extent of hysteresis would be greatly reduced if not eliminated. Lastly, since Ca is small the hysteresis is more of a result of the heterogeneous nature of the substrate than the motion of the droplet.

Comparison to Theory

The simulations give the center-of-mass position of the droplet as a function of time or the velocity. We now compare the velocity gotten by simulation with that predicted by theory.

The data in Fig. 4.6(b) have been fit to a power law or $x_{CM} = ct^n$. The velocity is then $V = nct^{n-1}$ or

$$V = nc^{1/n} x_{CM}^{1-1/n}. \tag{4.5}$$

The quasi-steady velocity of a ridge on a wetting gradient has been estimated by Brochard [138]. By equating the driving force (Eqn. 4.1) and the drag force (Eqn. 4.2) the velocity is found to be

$$V = \frac{\gamma[\cos\theta_e(x_a) - \cos\theta_e(x_r)]\theta_0}{6\mu \ln(x_{max}/x_{min})}. \tag{4.6}$$

The value of x_{min} must be estimated before Eqn. 4.6 can be evaluated. The results of non-equilibrium molecular dynamics simulations by Thompson et al. [164]

suggests that $x_{min} \approx 1.8\sigma$ for simple fluid-solid systems. Using this recommendation with $\sigma = \sigma_{OO}$ we find $x_{min} \approx 5.7$ Å. The values of x_{max} can be estimated from Fig. 4.10. For the $N = 2000$ droplet, one-half the base length varies from 27.4 to 64.4 Å. This means that the ratio x_{max}/x_{min} varies from roughly 5 to 11. For the larger droplet the slip length is taken to be the same and this leads to the ratio varying from 8 to 14.

One concern in applying Eqn. 4.1 to describe the driving force is that it does not account for contact angle hysteresis. The expression was derived for ideal surfaces and when applied to real surfaces it over predicts the force. If knowledge of the advancing and receding contact angles is available then those values can be used in place of the equilibrium angles appearing in Eqn. 4.1. Approaches to modify the driving force for spherical droplets have been described [144, 150]. Secondly, given that the driving force depends on $\theta_e(x)$ one must question how well contact angles are reproduced by molecular droplets. This concern has been addressed by Hautman and Klein [38] who point out that the contact angle of a sessile drop may be calculated accurately as long as the bulk region of the droplet is sufficiently large (i.e., the height of the drop is greater than the sum of the liquid-vapor and solid-liquid interfacial thicknesses). This criteria is satisfied for droplets of water on SAMs consisting of as few as 90 molecules. Additional studies have also found good agreement between the microscopic and macroscopic contact angles [39, 41, 162]. Since the curvature of a cylindrical cap in the plane of the substrate is infinite the line tension makes no contribution to the force balance at the three-phase contact line. This is not true for small spherical-cap droplets where the line tension may play a significant role in determining the droplet profile. Lastly, the liquid-vapor tension appears in Eqn. 4.1. The SPC/E model of water at 300 K has been reported to

have a surface tension of 55.4 ± 3 mN/m, which is 23% lower than the experimental value of 71.7 mN/m [165]. If the value of 55.4 mN/m holds for the droplets in our simulations then this would have the effect of lowering the driving force.

The derivation of the hydrodynamic drag force $F^{(h)}$ is based on lubrication theory which assumes that the height of the droplet is much less than the base length or, equivalently, that the contact angle is small. At the beginning of the simulations both the advancing and receding contact angles are greater than 90° suggesting immediately that the derivation makes assumptions that are violated. When Moumen et al. [150] use their expression for the hydrodynamic force, which is based on lubrication theory, to compare the droplet velocity to experimental data they find increasing agreement with increasing position along the gradient where the contact angle is smaller. Additional simplifications in the derivation of Eqn. 4.2 include the expansion of trigonometric functions of the contact angle to first order and the assumption that the droplet profile may be treated as a pair of wedges with equal wedge angles. This latter approximation is valid for small gradient strengths but droplet profiles from the simulations are seen to be asymmetric (Fig. 4.9) indicating a relatively strong gradient in the present work. The fluid property appearing in Eqn. 4.2 is the viscosity. At 301 K, the viscosity of the SPC/E model is reported to be 0.91 mPa s [166], which agrees well with the experimental value of 0.85 mPa s.

Before plotting Eqn. 4.6, the best-fit line to the simulation results of the base length versus center-of-mass position was found for each drop size. Using this least squares approximation the value of x_{max} for a given x was found as one-half the base length. The advancing/receding edge position of the droplet was assumed to be found by adding/subtracting half the base length from the center-of-mass position. The cosine of the equilibrium water contact angle at the advancing and

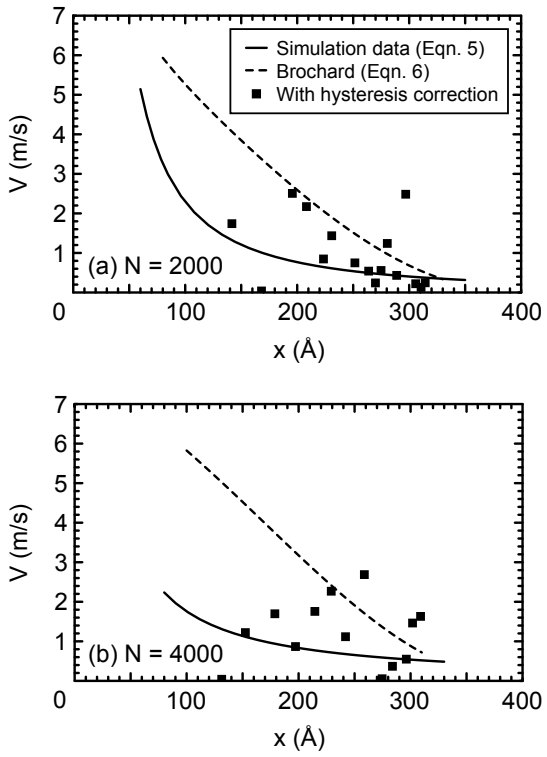

Figure 4.13: Droplet velocity as a function of position along the gradient as gotten by simulation and theory for (a) $N = 2000$ and (b) $N = 4000$ water molecules per drop. Edge effects are taken into account by only considering velocities on the intermediate region of the gradient.

receding edges were gotten by evaluating a second-order interpolating polynomial: $a_2\chi_p^2 + a_1\chi_p + a_0$ with $a_2 = -1.64$, $a_1 = 3.10$, and $a_0 = -0.497$, where χ_p is the local mole fraction of $HOCH_2$-terminated chains. The interpolating polynomial is based on simulation data from a previous study of uniformly mixed monolayers (see Table 2 of Ref. [162]).

Fig. 4.13 compares the simulation results with the theoretical predictions for the quasi-steady velocity of the droplet. The simulation results (Eqn. 4.5) are given by the solid curve while Brochard's solution (Eqn. 4.6) is drawn as a dashed curve. The predicted velocity is found to overestimate the measured values at all positions and for both droplet sizes. Better agreement is seen for the smaller droplet. Brochard's prediction is nearly linear with a slight change in slope towards the end of the gradient. The simulations show the velocity to decrease rapidly for small and intermediate values of the axial coordinate and then only slightly for large values. Moumen et al. [150] have experimentally measured the droplet velocity as a function of position along the gradient. Because the water contact angle in their case is approximately constant over the first 2.5 mm of the gradient a maximum is seen in the velocity as a function of position. However, beyond the position where the maximum occurs the experimental results appear to follow a power law. In the present work, the water contact angle varies smoothly with position (see Fig. 4.12) so no maximum is seen. This suggests that the qualitative difference between the two curves in Fig. 4.13 arises from simplification made in the derivation of Eqn. 4.6. Note that for both droplet sizes the agreement becomes better as the dynamic contact angle decreases, which is when the lubrication approximation becomes more justified.

Despite the many assumptions in the derivation of Eqn. 4.6 the agreement be-

tween the simulation results and the theoretical predictions is fair. Because contact angle hysteresis is ignored in Eqn. 4.6 the theory gives higher velocities than those found by simulation. One simple way to account for the effect of hysteresis is to use the advancing and receding contact angles instead of the equilibrium values. With this modification the driving force becomes

$$F^{(Y)} = \gamma[\cos\theta_a(x_a) - \cos\theta_r(x_r)]. \tag{4.7}$$

The square symbols in Fig. 4.13 give the velocity of the droplet when the driving force is based on the measured values of $\theta_a(x_a)$ and $\theta_r(x_r)$. While the data with the hysteresis correction are scattered, in general, better agreement is seen.

The small and large droplets were found to move with approximately the same speed. For the same center-of-mass position, the ratio of the base length of the larger droplet to that of the smaller droplet decreases from 1.6 to 1.3 as x_{CM} increases. According to Eqn. 4.6, if we assume that the cosine of the equilibrium contact angle varies linearly with position and the droplet profile is circular then

$$V \sim \frac{l_b}{\ln(l_b/s)}, \tag{4.8}$$

where $s = 2x_{min}$. Using the base length data from the simulations, Eqn. 4.8 suggests that the speed of the larger droplet should be 1.2 to 1.3 times faster than the smaller droplet. This factor is not very large and might be offset by the effect of contact angle hysteresis. For a spherical-cap droplet on a wetting gradient the speed is found to be proportional to the base radius of the droplet.

Fig. 4.13 indicates that the water nanodroplets move with speeds of meters per second. The numerous millimeter-scale experimental studies on spherical-cap droplets typically report velocities of millimeters per second. Thus, an increase in speed of three orders of magnitude is found in going from the millimeter to the nanometer scale.

A cylindrical fluid droplet is unstable and will break up into spherical-cap droplets with time [167]. Our simulations enforce stability by the small choice of the width of the simulation cell. Spherical nanodroplets were not considered in this work because even on a one-dimensional gradient the droplet would spread significantly in two dimensions. Because of this the simulation cell would have to be increased in the y-direction to ensure that image droplets do not influence the results. A significant amount of CPU time above that for the cylindrical droplet case would be needed to simulate spherical droplets.

4.4 Conclusions

Molecular dynamics simulations of Lennard-Jones and water nanodroplets were conducted to investigate the motion of a liquid droplet on a wetting gradient. The two different systems exhibited a similar overall behavior for the motion with a simple power law describing the center-of-mass position with time. For the water nanodroplets the uniformity of the gradient was found to be an important factor in determining whether the droplet traversed the entire gradient or became pinned at an intermediate position. These simulations have demonstrated the ability of wetting gradients to move nanodroplets of water over distances of tens of nanometers or nearly ten times the initial base radius of the droplet. Fair agreement was seen

between the simulation results for the droplet velocity and the theoretical predictions. When contact angle hysteresis was accounted for by basing the driving force on the measured advancing and receding contact angles instead of the equilibrium values the agreement was found to improve.

Chapter 5

Wetting of Hydrophobic Substrates by Nanodroplets of Aqueous Superspreading and Alkyl Polyethoxylate Surfactant Solutions

In Chapter 3, the water contact angles for SAMs of varying surface energy were computed. These values for the more hydrophobic monolayers were of course large. In this chapter we simulate the wetting of aqueous droplets containing surfactant on hydrophobic surfaces. The goal is to gain a deeper understanding of how surfactants enhance wetting with special attention paid to the superwetting surfactants.

5.1 Introduction

Aqueous trisiloxane solutions at low concentrations have been shown to wet-out on highly hydrophobic substrates such as polyethylene [8]. This behavior has not been demonstrated by any other surfactant. Many explanations have been proposed to explain this phenomena and they have been discussed in Chapter 1. While many aspects of the proposed mechanisms can not be probed by molecular simulations some can be. For instance, evidence from neat [28, 29] and aqueous [31] trisiloxane droplets suggests the formation of a bilayer at the spreading front. Because the bilayer is a small structure (two molecules in the vertical direction) it is something that can be reproduced by a simulation.

A number of authors have conducted Lennard-Jones simulations to study the wetting of solid substrates by surfactant-laden droplets. McNamara et al. [168] considered cylindrical droplets and showed that surfactants could enhance wetting when the solvophobic tail group embedded itself into the solid substrate. While such a behavior may be possible for some substrates, surfaces formed from self-assembled monolayers and rigid, atomically-smooth solids like graphite do not. Shen et al. [48] carried out a comparative study of linear and T-shaped surfactants. Results for two sets of interaction coefficients were reported. For the reference set the authors found that the droplet with T-shaped surfactants spread significantly more than the linear case. When the interaction between the solvent and the solvophilic groups was reduced the extent of spreading was found to be similar for both systems with more surfactant found at the solid-liquid interface for the T-shaped case. The effect of droplet size was not explored in this work and it is likely that much of the reported behavior would change if larger droplets were considered. Kim et al. [51]

considered linear surfactants only. The authors found that the spreading rate was strongly influenced by the strength of the interaction between the tail group of the surfactant and the substrate.

Molecular simulations with potential functions for real materials have been used to compute static contact angles of sessile droplets on pure substrates [43, 41, 39, 40, 162]. Lundgren et al. [39] determined the equilibrium contact angle for water and water with ethanol on graphite. The spreading dynamics were not reported.

Molecular simulations are limited to nanometer length scales and nanosecond times scales. Because of this it is not possible to simulate a drop that is large enough to contain vesicles. Nor can the Marangoni effect be seen for nanoscopic systems. However, a few of the elements that have been proposed to explain superspreading can be studied. Specifically, by studying the behavior of trisiloxane and alkyl polyethoxylate surfactant-laden droplets we can learn about how the wetting behavior is affected by the orientation of the surfactant at the spreading edge, the affinity of each surfactant for the substrate, and whether or not the spreading edge forms a structure like a reverse bilayer.

5.2 Simulation Methodology

Molecular dynamics simulations are conducted to study of the wetting of hydrophobic substrates by droplets of aqueous superspreading and alkyl polyethoxylate surfactants solutions. Both spherical and cylindrical droplets are considered.

5.2.1 Wetting of Graphite by Aqueous Surfactant Droplets

The drops for these simulations were constructed by extracting a spherical cluster from a large simple cubic lattice of randomly-orientated water molecules arranged at ambient liquid density. Surfactant molecules, either M(D′E_4OH)M or $C_{12}E_4$, were arranged at the liquid-vapor interface with their hydrophiles inserted into the drop and their hydrophobes in air.

A spherical water droplet composed of 9997 molecules has a radius of roughly 4 nm. The inverse surface concentration at maximum packing for M(D′E_4OH)M is 53.4 Å^2/molecule. At this concentration there would be 377 surfactant molecules on the surface of the droplet. To keep the interfacial tensions low the surface concentrations must remain high as the droplet spreads. To ensure that his happens an additional 98 molecules were added. The critical aggregate concentration for M(D′E_4OH)M is 0.11 mole/m^3. If the bulk concentration of the droplet were at the CAC the number of surfactant molecules in the droplet would be CAC $\times$ V $\times$ N_A =(0.11 mole/m^3)$(4/3\pi R^3)N_A$ = 0.02 molecules, where V is the volume of the droplet and N_A is Avogadro's number. There were no surfactant molecules in the bulk of the droplets for the initial simulations. For the trisiloxane system the solution concentration is 54.6 wt%, which is much larger than the typical 1 wt% used in experimental superspreading studies. The $C_{12}E_4/H_2O$ droplet was constructed in a similar manner. With the CAC for $C_{12}E_4$ being 0.05 mole/m^3 the number of molecules in bulk should be 0.01. In order to compare the two simulations 475 surfactants molecules were placed on the liquid-vapor interface of the droplet.

The substrate was composed of two layers of graphite. Water and surfactant interacted with graphite through a Lennard-Jones interaction with the parameters of Ref. [40], which specifically considered the SPC/E model for water. The separation

distance between the layers is 3.41 Å. The carbon-carbon bond length is 1.421 Å.

The simulations were carried out at constant number of molecules, system volume, and temperature using a self-written research code in the Fortran 90 programming language. The code was parallelized using MPI. The velocity Verlet method was used to perform the numerical integration of the equations of motion. All bond lengths were kept fixed using RATTLE [57]. The temperature was maintained at 298.15 K using a Nosé-Hoover thermostat with a relaxation time of 15 fs. The timestep was 2 fs. The SPC/E interaction potential [54] was used for water while the OPLS-UA force field [122, 123] and a force field for polydimethylsiloxane [169] were used for the surfactants. The OPLS combining rules were used. The interaction between any pair of atoms in the same molecule which are separated by three or fewer bonds was excluded. Short-range interactions were cutoff at 10 Å. Open boundary conditions were used. An external potential was used to contain vapor molecules. The simulations were run on DataStar at the San Diego Supercomputer Center. The atomic coordinates were written to file every 2 ps.

The fast multipole algorithm [170, 171, 172] was used to compute long-range interactions. The number of terms retained in the multipole expansion, p, was 5. A multiple time stepping scheme was used where the far field multipole coefficients were only updated once every ten time steps. The neighbor lists were updated with the same frequency. These choices were shown to give a root-mean-square error in the force of less than 1% on average. Similar parameters have been used elsewhere [173].

A spatial decomposition scheme based on that of Plimpton [61] was employed. Loading balancing was done manually by choosing a domain shape that minimized the void space. During early times when the droplet is approximately spherical a

cubic volume was considered. As the droplet spread the number of spatial subdomains in the direction normal to the substrate was reduced while those in the transverse directions were increased.

5.2.2 Wetting of SAMs by Aqueous Surfactant Droplets

A second set of simulations were conducted using cylindrical instead of spherical droplets. Cylindrical droplet wetting simulations were carried out for three surfactant solutions: $M(D'E_4OH)M/H_2O$, $MDM'E_4OH/H_2O$, and $C_{12}E_4/H_2O$. The number of water molecules and surfactant molecules in each case was 12,000 and 245, respectively. Only differences in simulation methodologies between the spherical and cylindrical droplet wetting runs are described here.

The parallel molecular dynamics simulations [120] were carried out at constant number of molecules, system volume, and temperature using the third-party code NAMD [121]. The Verlet method was used to perform the numerical integration of the equations of motion for the surfactant molecules and chains of the monolayer while SETTLE [59] was used for water. All bond lengths in the surfactant and monolayer were kept fixed using SHAKE [56]. Periodic boundary conditions in three dimensions were used. The box dimensions were $L_x = 34.43$ Å, $L_y = 397.60$ Å, and $L_z = 250.00$ Å. The PME technique [124, 125] was used to account for long-range interactions with the smallest number of grid points per direction being 0.88 $Å^{-1}$. The timestep was 2 fs. The temperature was maintained at 298.15 K by applying a Langevin thermostat, with a damping coefficient of 0.5 ps^{-1}, to non-hydrogen atoms.

The substrate was composed of a self-assembled monolayer with 80 chains in the x-direction and 8 chains in the y-direction (see Section 3.2 for details). The

mole fraction of $HOCH_2$-terminated chains was 0.25. This corresponds to a water contact angle of 75.9° making the substrate for these simulations less hydrophobic than graphite. Stoebe et al. [15] showed that the maximum spreading rate for $M(D'E_4OH)M/H_2O$ occurred at a concentration of 2 wt% on a SAM with a water contact angle of 66°.

5.3 Results and Discussion

5.3.1 Spherical Droplets

Werder et al. [40] reported a water contact angle for graphite of 95.3°. Since we have used the same water-graphite interaction, as a check of our code we have conducted a similar simulation of a pure water droplet composed of 1000 molecules. We find a value of 89° which agrees with that of Ref. [40].

The initial configuration for the trisiloxane droplet is shown in Fig. 5.1. Because the liquid-vapor interface is densely packed with surfactant molecules very few water molecules are seen. The droplet is allowed to spread freely on the substrate at 298.15 K. A cross-sectional view of the final configuration of the simulation is shown in Fig. 5.2. The simulation was stopped after 1.1 ns because very little spreading was seen. The figure reveals that the interfaces are densely packed with surfactant. The inverse surface concentrations at the solid-liquid and liquid-vapor interfaces are 75 and 57 $Å^2$/molecule, respectively. None of the molecules were seen to leave the interface and enter the bulk of the droplet. The polyethoxylate chains are seen to be interacting with water while the trisiloxane hydrophobes are in air. The equilibrium contact angle of the droplet is larger than ninety degrees. Clearly, the droplet did not superspread. We will discuss why the droplet do not spread below.

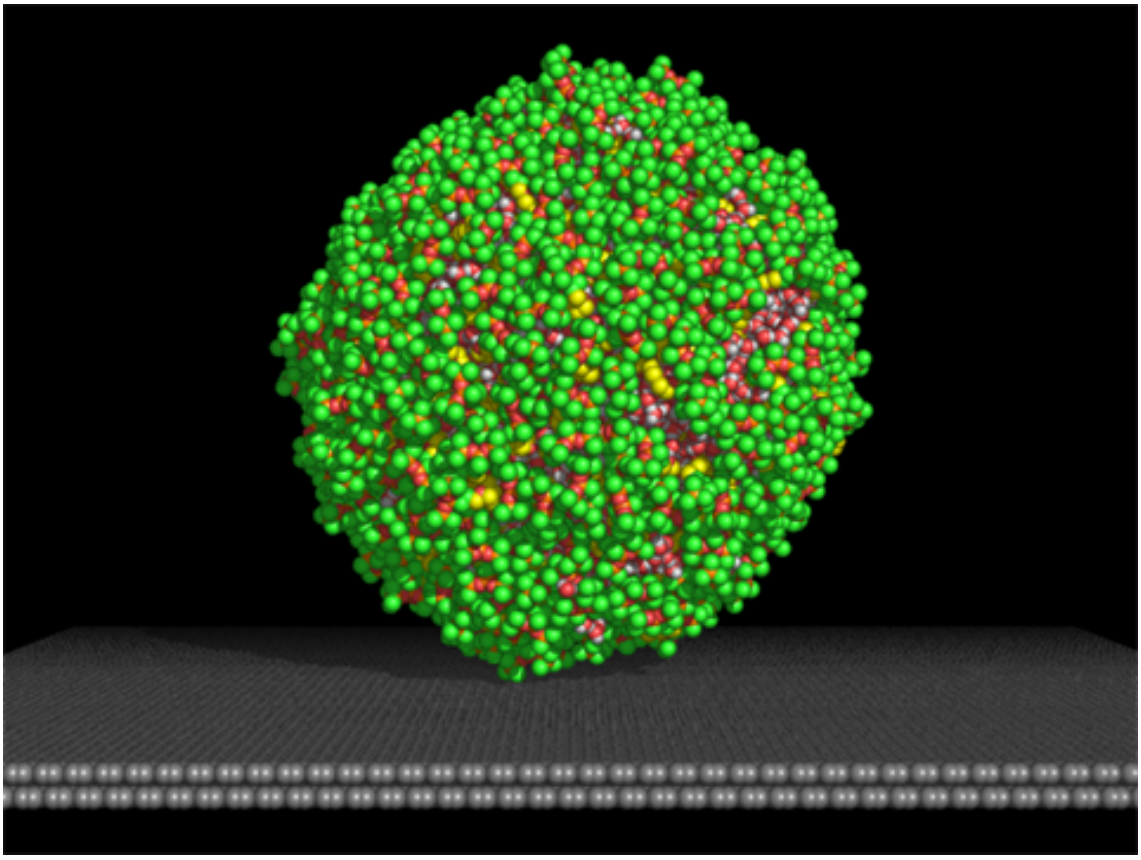

Figure 5.1: At $t = 0$, a spherical nanodroplet consisting of 9997 water molecules and 475 trisiloxane molecules is placed in the vicinity of a graphite substrate.

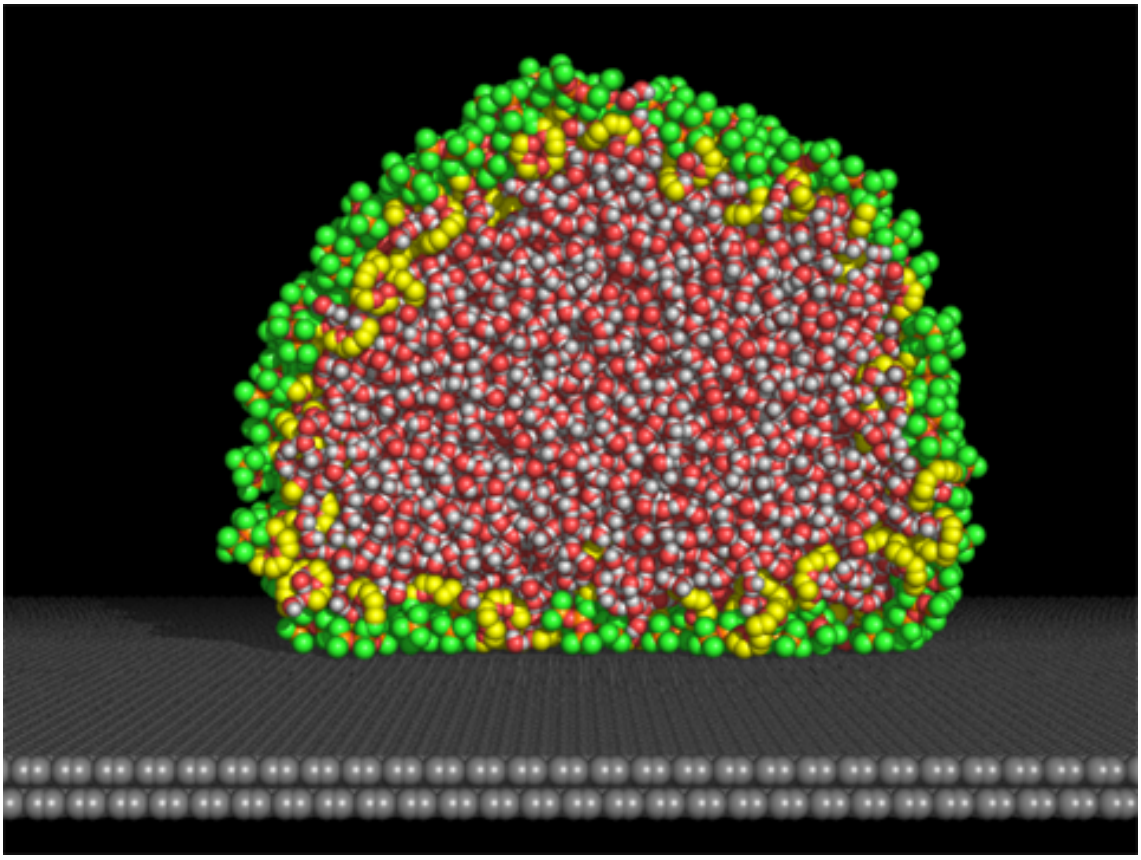

Figure 5.2: Cross-sectional view of the final configuration of the M(D′E_4OH)M/H_2O droplet at 1.1 ns.

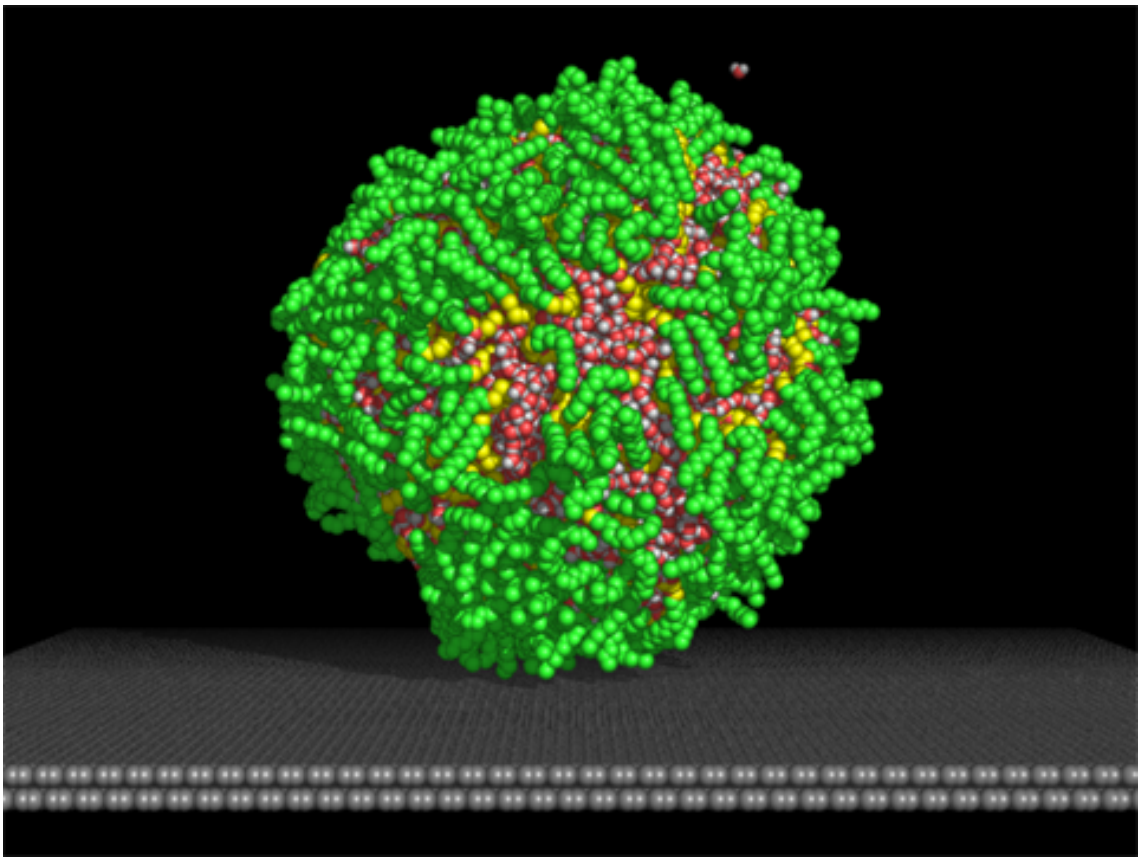

Figure 5.3: Same as Fig. 5.1 except for a $C_{12}E_4/H_2O$ droplet.

The $C_{12}E_4/H_2O$ droplet is shown at $t = 0$ in Fig. 5.3 and at the final time step in Fig. 5.4. The droplet is found to spread more than the trisiloxane case. The inverse surface concentrations at the solid-liquid and liquid-vapor interfaces are 134 and 63 Å^2/molecule, respectively. The equilibrium contact angle is approximately 55°.

An approach similar to that of Kim et al. [51] is used to determine the shape of the droplet. The base radius, r_B, is taken as the radius of a cylinder, which is aligned with the center-of-mass axis of the droplet, that contains 85% of the atoms that are within 10 Å of the substrate. The height, h, is taken as the height of a cylinder with a radius of 10 Å, which is aligned with the center-of-mass axis of the droplet, that

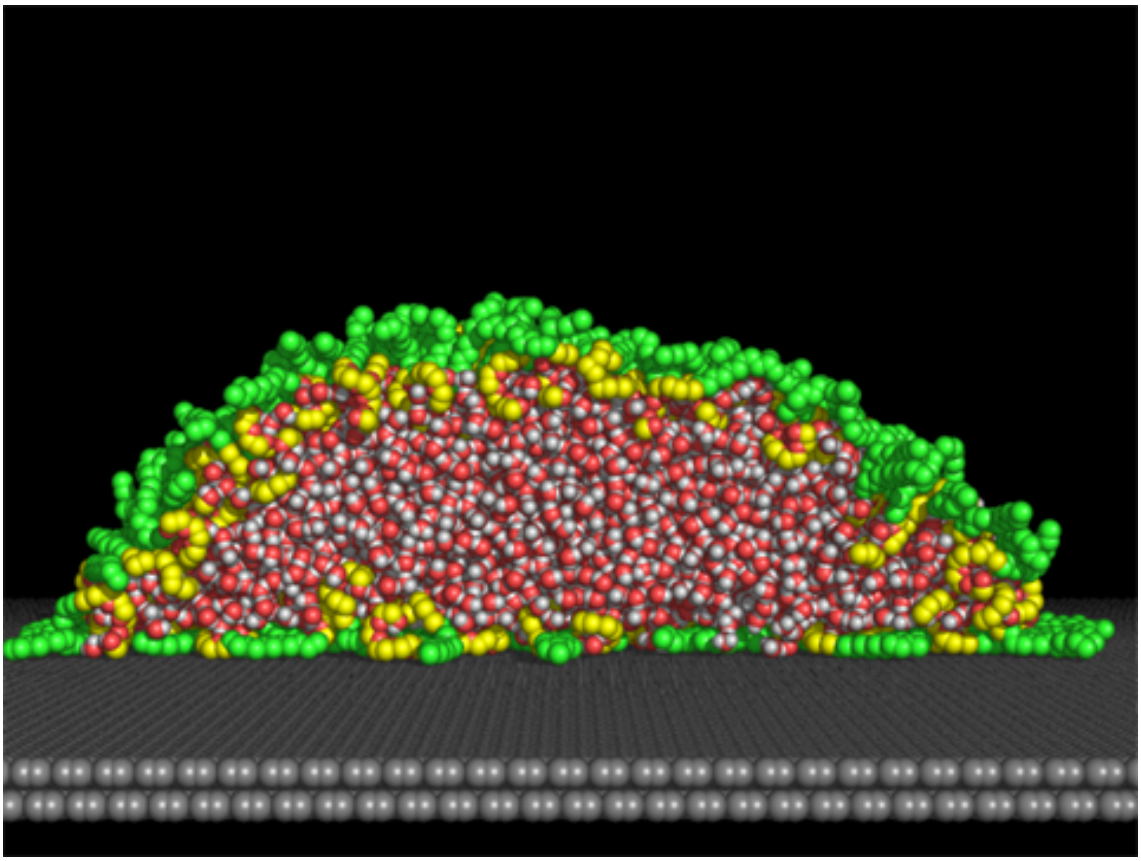

Figure 5.4: Cross-sectional view of the final configuration of the $C_{12}E_4/H_2O$ droplet at 1.3 ns.

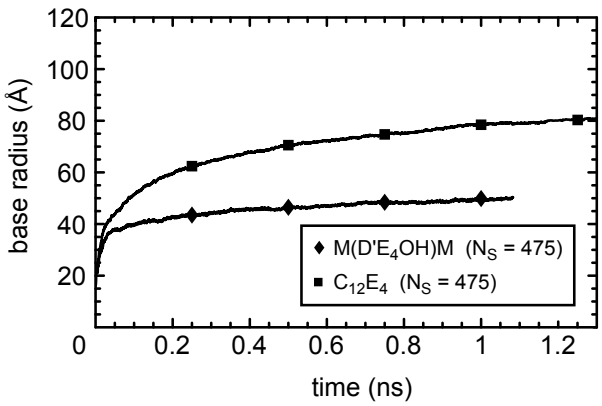

Figure 5.5: Base radius versus time for the M(D′E_4OH)M/H_2O and $C_{12}E_4$/H_2O droplets.

contains 85% of the atoms that are between the substrate and h. The contact angle is determined by r_B and h through $\cos\theta = 1 - h/R$ and $(R-h)^2 = R^2 - r_B^2$, where R is the radius of the truncated sphere.

The extent of spreading of the two droplets is characterized by the change in base radius (Fig. 5.5). The base radius of the trisiloxane droplet changes very little with time after the first 100 ps of the simulation. The $C_{12}E_4$/H_2O droplet, which also begins as a sphere with a radius of 4 nm, is found to have a final base radius of 8 nm.

The water density in the normal direction is shown in Fig. 5.6. The edges of the droplets were ignored in calculating these profiles. For the pure water droplet, peaks are seen at $z = 3.1$ and 6.1 Å. These arise from water molecules adopting configurations at the solid-liquid interface that maximize the number of hydrogen bonds. The curve is in agreement with Ref. [40]. The trisiloxane surfactants are found to exclude water from the interface. This is largely due to the high initial surface concentration and the lack of spreading. The projected area of the trisiloxane group is approximately equivalent to that of the hydrophilic moiety. The bulk density of

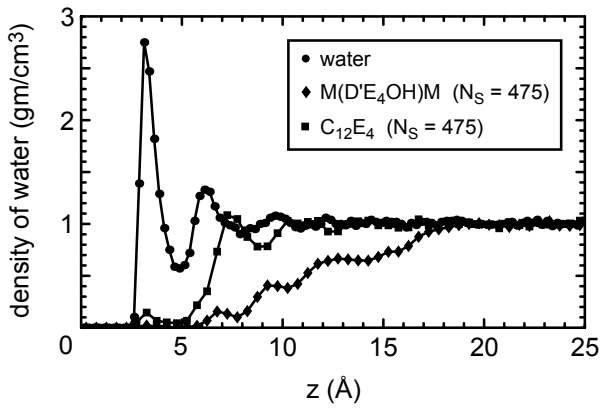

Figure 5.6: Water density in the normal direction.

water is recovered at $z \approx 20$ Å. The $C_{12}E_4$ molecules are not as effective at removing interfacial water as the trisiloxanes. Because the polyethoxylate surfactants are not as densely packed, the density of water reaches its bulk value at $z \approx 7.0$ Å.

The number of hydrogen bonds per water molecule is shown in Fig. 5.7 as a function of the z-coordinate. According to the geometric definition of Martí [174], two water molecules form a hydrogen bond if the oxygen-oxygen and oxygen-hydrogen separation distances are less than 3.6 and 2.4 Å, respectively. Furthermore, the angle between the vector formed by the oxygen atoms and the vector formed by the hydrogen atom and oxygen atom of the molecule of interest must be less than 30°. The same criteria can be applied to determine the number of hydrogen bonds between water and surfactants. For the pure water droplet we find a bulk value of 3.5 hydrogen bonds per water molecule. In the vicinity of the hydrophobic solid the number of hydrogen bonds is found to decrease. Molecules in this region are said to have daggling OH bonds. Water molecules are found to have more hydrogen bonds on average for the polyethyoxylate solution than for the trisiloxane case.

The $M(D'E_4OH)M/H_2O$ droplet did not spread appreciably because there were too many molecules on the liquid-vapor interface. The initial inverse surface concen-

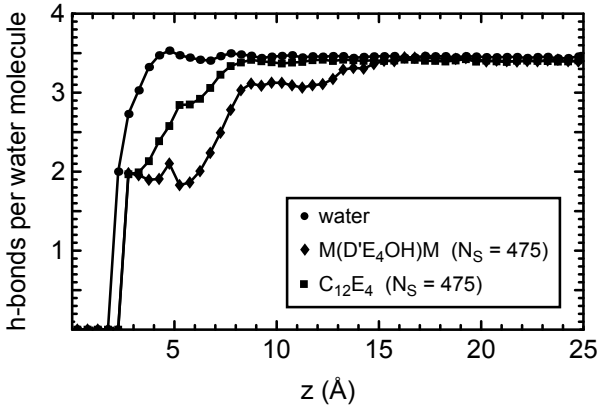

Figure 5.7: Number of hydrogen bonds per water molecule in the normal direction.

tration for both surfactant droplets was 42.3 Å^2/molecule. This value is higher than the inverse maximum packing concentration for a planar monolayer of M(D′E_4OH)M, which is 54.3 Å^2/molecule [35]. The surfactant molecules at the interface prevent the droplet from changing its shape. The $C_{12}E_4/H_2O$ did spread appreciably because the initial surface concentration is very similar to its maximum packing concentration where the minimum in γ is found. The maximum packing concentration of $C_{12}E_4$ at the liquid-vapor interface has been reported as 38 Å^2/molecule [175] and 44 ± 3 Å^2/molecule [176]. The value of γ for this system at initialization is 43.5 mN/m.

To test our hypothesis that there was too much surfactant in the trisiloxane case, 175 surfactant molecules were removed from the droplet at $t = 0.7$ ns and the simulation was continued. When this was done the droplet was found to spread more. The contact angle was found to decrease by 15° from $t = 0.7$ to 1.1 ns (Fig. 5.8). However, the final contact angle is comparable to the contact angle of the pure water droplet. A third simulation was run where at initialization only 250 M(D′E_4OH)M molecules where placed on the surface and 100 molecules were randomly distributed

throughout the bulk of the droplet. This gives an inverse surface concentration of 80.4 Å^2/molecule, which corresponds to an interfacial tension of 56.0 mN/m. In this case, the final value of θ was found to be 75°.

For the $C_{12}E_4/H_2O$ case, an additional run was conducted with 300 molecules instead of 475. For this system the initial inverse surface concentration is 67.0 Å^2/molecule, which corresponds to a liquid-vapor interfacial tension of 60.7 mN/m. It can be seen from Fig. 5.8 that the equilibrium contact angle is higher than that of the original case. The $C_{12}E_4/H_2O$ droplets appear to follow a classical wetting model where the droplet spreads until the forces at the three-phase contact line balance. Because the simulations are conducted with a fixed number of surfactants molecules, spreading ceases when the interfacial areas become large. It is expected that if more surfactant were added to the $N_S = 300$ droplet that additional spreading would be seen.

The wetting behavior of a droplet composed of 20,000 water molecules and 673 M(D′E_4OH)M molecules on a SAM with $\chi_p = 0.367$ was also studied. With five of the surfactant molecules initialized in the bulk of the droplet the initial inverse surface concentration was 67.7 Å^2/molecule. As in the previous cases very little spreading was seen. After 6.2 ns the temperature of the system was increased to 450 K. This caused several water molecules to escape from the droplet and act as a vapor. Additional spreading was seen but it was not dramatic.

5.3.2 Cylindrical Droplets

Wetting simulations were conducted for M(D′E_4OH)M/H_2O, MDM′E_4OH/H_2O, and $C_{12}E_4/H_2O$ in the form of cylindrical droplets. The same overall behavior was seen for the cylindrical droplets as for the spherical cases. That is, little spreading was

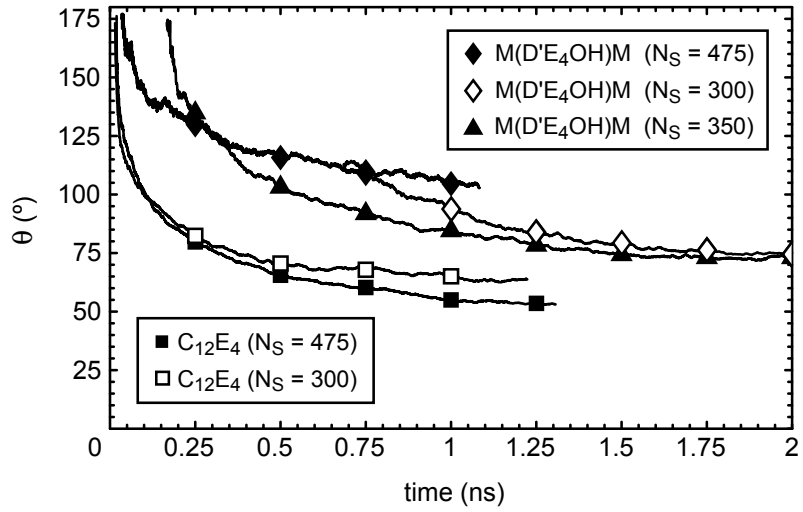

Figure 5.8: Contact angle versus time for five surfactant-laden droplets on graphite. The number of water molecules was 9997 in all cases.

observed. The final configuration of the M(D′E_4OH)M/H_2O droplet is shown in Fig. 5.9 at $t = 19.0$ ns. The initial radius and inverse surface concentration for each droplet were 5 nm and 44.2 Å^2/molecule, respectively.

The $C_{12}E_4$/H_2O droplet is found to have a lower center-of-mass position, z_{CM}, than the other droplets. This is because the initial surface concentration for this droplet is similar to the maximum packing concentration of $C_{12}E_4$ whereas for the hammer-like trisiloxane case the initial surface concentration is larger than its maximum packing concentration. The MDM′E_4OH/H_2O droplet is found to have an equilibrium value of z_{CM} that is slightly below that of the M(D′E_4OH)M/H_2O droplet (Fig. 5.10).

5.4 Conclusions

Droplet wetting simulations were conducted for aqueous trisiloxane and polyethoyxlate solutions. While the $C_{12}E_4$ systems showed a behavior that is consistent with a sim-

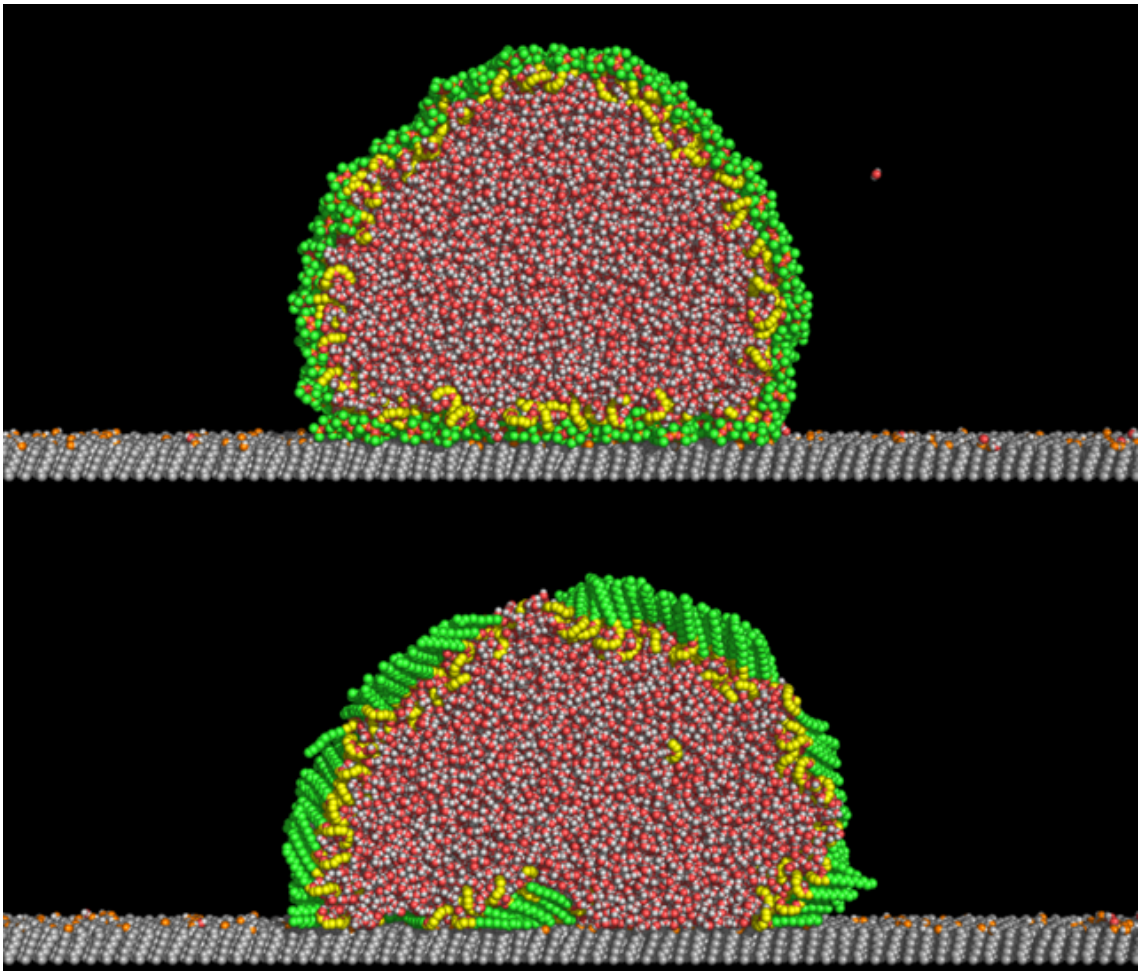

Figure 5.9: Final configurations of cylindrical $M(D'E_4OH)M/H_2O$ (top) and $C_{12}E_4/H_2O$ (bottom) droplets on a self-assembled monolayer with $\chi_p = 0.25$.

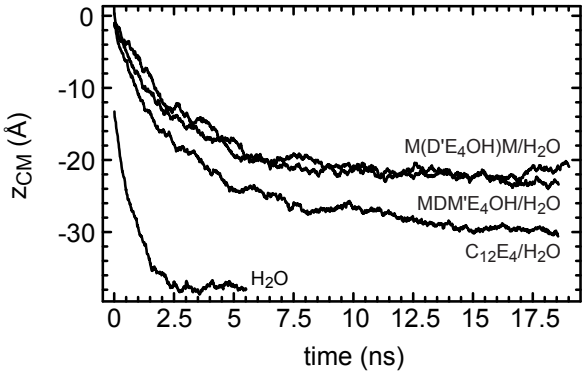

Figure 5.10: Center-of-mass position versus time for water and three surfactant-laden droplets.

ple wetting theory based on the Young equation, the trisiloxane systems showed a different behavior. For initial surface concentrations above the maximum packing concentration the M(D′E_4OH)M/H_2O and MDM′E_4OH/H_2O droplets did not spread appreciably. When the initial surface concentration was below the maximum packing concentration the M(D′E_4OH)M/H_2O droplet showed increased spreading but the final contact angle was still large.

The challenge of these droplet wetting simulations is to find a way to maintain the surface concentrations at values close to that of maximum packing throughout the simulation. In real systems, where the surface to volume ratio is orders of magnitude smaller, this is accomplished by surfactant molecules or molecular aggregates diffusing to the interface from the bulk and adsorbing. Because the time scales for diffusion and adsorption can be large ($\sim$1 ms), mimicing such behavior is a challenge for computer experiments where the total length of the simulation is restricted to tens of nanoseconds.

Chapter 6

Bulk and Interfacial Properties of Aqueous Superspreading and Alkyl Polyethoxylate Surfactant Solutions

Trisiloxane surfactants have the unique ability to promote the rapid and complete wetting of aqueous droplets on hydrophobic, hydrocarbon substrates. It has been a challenge to explain why these surfactants are superior to all others. To help understand this phenomena at the molecular scale we have conducted molecular dynamics simulations to probe the interfacial and bulk properties of these aqueous surfactant solutions. The surfactant molecules of a 35.2 wt% M(D′E_4OH)M solution, which were randomly distributed at initialization, were found to self-assemble into a bilayer in less than 50 ns at 375 K. The bilayer was shown to be stable for an additional 50 ns. The behavior of the alkyl polyethoxylate surfactant, $C_{12}E_4$, which

is composed of the same head group and a tail group with similar hydrophobicity as M(D′E_4OH)M, was studied for comparison. This linear surfactant was also found to form a bilayer on the same time scale. The adsorption isotherms at 298.15 K for each surfactant system were also determined. In the case of the M(D′E_4OH)M monolayer, the simulation results were found to overestimate the experimental values while for $C_{12}E_4$ the computed tensions are found to be within one standard deviation of the experimental data for each surface concentration considered. A second force field with a weaker interaction between trisiloxane groups gives much better agreement.

6.1 Introduction

Trisiloxane surfactants have the unique ability to promote the rapid and complete wetting of aqueous droplets on hydrophobic substrates such as polyethylene [8]. The phenomena is so dramatic that it is referred to as superspreading. The trisiloxanes have been used in agricultural applications [177, 178]. Their application has been restricted because they are only stable over a narrow pH range. While superspreading was first observed in the 1960s, its mechanism is still not understood.

Gradzielski et al. [6] examined the aqueous phase behavior of various siloxane surfactants. Scriven and Davis and coworkers investigated the phase behavior of aqueous trisiloxane solutions (M(D′E_nOH)M for $n = 5$, 8, 12, and 18) using a variety of experimental techniques including small-angle X-ray and neutron scattering, wide-angle X-ray scattering, and cryo-transmission electron microscopy [7]. The phase behavior was found to depend strongly on the number of ethylene oxide groups, n, and the terminal group. The surfactants with small n showed a tendency to form lamellar bilayers while those with large n tended for form structures with high

curvature such as hexagonally-packed cylindrical micelles. The strong dependence on the terminal group has been found by other authors [177].

Hill et al. [179] studied the aqueous phase behavior of M(D′E_8OH)M, M(D′$E_8$$OCH_3$)M, and M(D′$E_8$OAc)M as well as a linear surfactant with a trisiloxane hydrophobe, MDM′E_8OH. For concentrations less than 2 wt%, the surfactants were found to form unilamellar and multilamellar vesicles. Particles of an uncertain identity were also found. The terminal group was shown to strongly influence the phase behavior. The linear surfactant was found to have a similar spreading rate as the other three surfactants at 0.1 wt% on Parafilm. The phase behavior of cationic trisiloxane surfactants in aqueous solution has also been investigated [180].

Wagner et al. [21] determined phase transition temperatures for M(D′$E_n$$OCH_3$)M for $n = 5 - 9$ at concentrations of 1 and 5 wt%. The wetting and phase transition temperatures have been studied for ternary mixtures [12]. The commercial superwetting agent, Silwet L-77®, was also studied. Li et al. [10, 11] produced binary phase diagrams for M(D′E_6OH)M/H_2O and M(D′E_{10}OH)M/H_2O. For low concentrations at room temperature, M(D′E_6OH)M is found to coexist as monomer and the L_α phase. The authors also studied the ternary phase behavior of M(D′E_nOH)M for $n = 6$, 10, and 12 with three low molecular weight silicone oils and water.

The phase behavior of equimolar solutions of M(D′E_nOH)M and water at 25 °C has been studied for $n = 8 - 20$ [14]. The effect of decane as a third component was also investigated. Wagner and Strey [13] determined the phase diagram for a highly purified trimethylsilane surfactant and water. The trimethylsilanes have a higher hydrolytic stability than the M(D′E_nOR)M.

The liquid-vapor surface tension of these systems as a function of surface concentration has been determined using pendant bubble tensiometry [35]. The minimum

surface tensions for M(D′E_4OH)M and $C_{12}E_4$ were found to be 22 and 29 mN/m, respectively. Superspreading is not explained by the simple difference in surface tension values. Fluorocarbon surfactants have been shown to reduce the air-aqueous interfacial tension to 19 mN/m, but they do not exhibit superspreading. This emphasizes the importance of also reducing the solid-liquid tension.

Due to the long time scales involved with the self-assembly of surfactant systems (in some cases milliseconds) there are few simulation studies where an initially uniform surfactant solution has been shown to form the equilibrium phase on the time scale of the simulation. Maillet et al. [181] used all-atom molecular dynamics simulation to reproduce the micellization of cationic surfactants. The simulations correctly predicted the spherical shape and the aggregation number. Using a Lennard-Jones model, Goetz and Lipowsky [182] conducted Monte Carlo simulations that produced different molecular aggregate structures such as spherical micelles and bilayers depending on the surfactant concentration.

Other simulations have started with the final aggregate structure and ignored the assembly. de Moura and Freitas [183] looked at the exchange of surfactant between micelles of sodium octanoate in water. The average aggregation number and the radius of gyration of the micelle were in fair agreement with previous MD and SANS studies. The non-ionic surfactant C_8E_5 was studied by Garde et al. [184]. The authors found the shape of the micelle to deviate significantly from a sphere at multiple points throughout the simulation. Using a course-grained model, Srinivas et al. [185] studied the self-organization of aqueous surfactant solutions of $C_{10}E_3$ and $C_{12}E_5$ on graphite. A bilayer was found in the case of $C_{10}E_3$ and continuous hemicylinders were found for $C_{12}E_5$. The packing behavior is consistent with the critical packing parameter of each surfactant and AFM data.

Klein and coworkers have investigated many interfacial systems including the properties of water-ethanol solutions [186], water-butanol [187], the self-organization of cationic surfactants (C16TAB) at a hydrophobic substrate [188], a reverse micelle of $C_{12}E_2$ [189], and studies of the liquid crystalline lamellar phase of $C_{12}E_2$ [44]. Surfactant monolayer simulations have been conducted for the anionic surfactant AOT [190], $C_{12}E_2$ [191], and $C_{12}E_5$ [47]. Adsorption isotherms were not computed in these studies.

6.2 Simulation Methodology

We consider two surfactant species in this work. To understand their phase behavior we simulated solutions of either $M(\acute{D}E_4OH)M/H_2O$ or $C_{12}E_4/H_2O$ on a graphite substrate in air. Surfactant monolayers were simulated in a second set of simulations to determine the adsorption isotherms.

The parallel molecular dynamics (MD) simulations [120] were carried out at constant number of molecules, system volume, and temperature using the third-party code NAMD [121]. The Verlet method was used to perform the numerical integration of the equations of motion for the surfactant molecules while SETTLE [59] was used for water. All bond lengths in the surfactant were kept fixed using SHAKE [56]. The SPC/E interaction potential [54] was used for water while the OPLS-UA force field [122, 123] and a force field for polydimethylsiloxane [169] were used for the surfactants. The OPLS combining rules were used. The interaction between any pair of atoms in the same molecule which are separated by three or fewer bonds was excluded. Short-range interactions were cutoff at 12 Å with a switching function applied for separations greater than 10 Å. Periodic boundary

conditions in three dimensions were used. The simulations were run on DataStar at the San Diego Supercomputer Center. The atomic coordinates were written to file every 2 ps.

6.2.1 Solid-Liquid Interface and Bulk Properties

The surfactant behavior at the solid-liquid interface and in bulk were investigated. The M(D′E_4OH)M and $C_{12}E_4$ systems were initialized in the same manner. An aqueous surfactant film on a graphite substrate was simulated. The two layers of atoms composing the solid were kept fixed in position throughout the simulation [40]. A monolayer consisting of 63 surfactant molecules was set down at the solid-liquid interface at the beginning of the simulation. This corresponds to an inverse surface concentration of 65.1 $Å^2$/molecule, which is larger than the maximum packing value of M(D′E_4OH)M [36]. The surfactant molecules were arranged with their hydrophobes in contact with the substrate and their hydrophiles pointing away from the substrate into the solution. An additional 126 surfactant molecules were randomly distributed throughout the solution. The total number of water molecules was 8829. The box dimensions were $L_x = 72.47$ Å, $L_y = 56.61$ Å, and $L_z = 143.41$ Å. The temperature was increased in steps of roughly 25 K from 298.15 to 375 K over the first half of the simulation. This was done to speed up the self-assembly process. The simulations were carried out for 100 ns. The time step was 2 fs. The temperature of the system was controlled by rescaling the atomic velocities at each time step. Using twelve IBM p655 nodes or 96 processors the simulations ran at roughly 20 ms/step.

6.2.2 Properties of the Liquid-Vapor Interface

The adsorption isotherm for each surfactant was computed at 298.15 K. A slab of water arranged at ambient liquid density was placed in the center of the simulation cell. The surfactant molecules were arranged with their hydrophobes in air and their head groups extended into the solution. The water region is chosen to be thick enough to yield bulk properties in the center. The number of water molecules in all cases was 4511. The box dimensions were $L_x = 51.2$ Å, $L_y = 44.7$ Å, and $L_z = 162.0$ Å. The first 2 ns of the simulation was taken as equilibration. The time step was 1 fs. The temperature was maintained at 298.15 K by applying a Langevin thermostat, with a damping coefficient of 0.5 ps^{-1}, to non-hydrogen atoms. The PME technique [124, 125] was used to account for long-range interactions with the smallest number of grid points per direction being 0.92 $Å^{-1}$. Full electrostatics are essential for the calculation of the surface tension [192, 193, 165]. The surface tension was calculated using the pressure-integration technique:

$$\gamma = \frac{1}{2}\int_{-\infty}^{\infty}[p_{\perp}(z) - p_{\parallel}(z)]dz, \tag{6.1}$$

where $p_{\perp}$ and $p_{\parallel}$ are the normal and tangential pressures, respectively. For the geometry considered in this work, Eqn. 6.1 may be written as

$$\gamma = \frac{1}{2}\langle p_{\perp} - p_{\parallel}\rangle = \frac{L_z}{2}\left[\langle p_z\rangle - \frac{\langle p_x\rangle + \langle p_y\rangle}{2}\right]. \tag{6.2}$$

6.3 Results and Discussion

6.3.1 Solid-Liquid Interface and Bulk Properties

The starting configuration for the aqueous M(D′E_4OH)M solution on graphite is shown in Fig. 6.1. A monolayer of sixty-three M(D′E_4OH)M molecules has been created at the solution-graphite interface. The surfactant molecules away from the substrate are randomly distributed. The solution is 35.2 wt% surfactant. To our knowledge the phase diagram for M(D′E_4OH)M has not been determined. It is known, however, that M(ĎE_5OH)M gives the L_α phase at room temperature at 45 wt% [7]. During the first 10 ns most of the surfactant in the bulk had agglomerated to form an amorphous aggregate. Two surfactant molecules had made their way to the liquid-vapor interface. At 23 ns, there is a gap of approximately 10 Å separating the aggregate from the surfactant head groups in the monolayer at the solid-liquid interface. From 20 – 30 ns, the aggregate is found to extend down to the monolayer. A distinct bilayer spanning the yz-plane of the simulation cell is found 45 ns into the simulation. This structure was found to be stable for an additional 55 ns. The final configuration of the simulation is shown in Fig. 6.1. The hydrophilic head groups are parallel to the substrate and the hydrophobes are packed against one another. The same two M(D′E_4OH)M molecules that went to the liquid-vapor interface during the early stages of the simulation were found to remain there. The approximate height and thickness of the bilayer are 65 Å and 25 Å, respectively.

The bilayer is uniform throughout except at the top where it curves. The curvature allows the hydrophobic trisiloxane groups to remain packed together with the ethoxylate groups exposed to water. The same behavior is seen at the ends of cylindrical micelles. The bottom of the bilayer is also curved. The ethoxylate chains

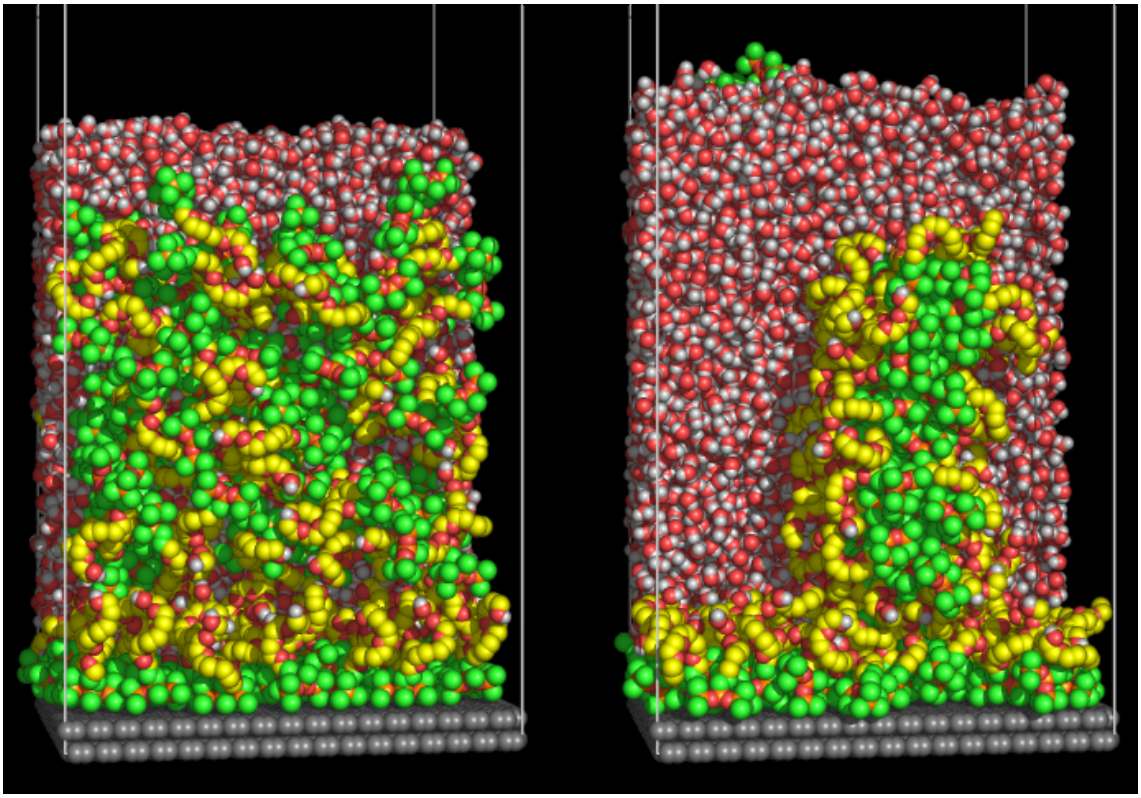

Figure 6.1: (Left) At $t = 0$, trisiloxane surfactant molecules are randomly distributed throughout an aqueous solution, which is in contact with a graphite substrate. A surfactant monolayer was arranged on the substrate. (Right) At $t = 100$ ns, the surfactant molecules are found to self-assemble into a bilayer. Water molecules have been removed from the front half of each image for visual clarity. The water molecules are shown with oxygen colored red and hydrogen in white while the surfactant molecules are shown with methyl and methylene groups as green/yellow, silicon as orange, oxygen as red, and hydrogen as white. The atoms of the graphite substrate are colored gray. The simulation cell, which is not completely shown in the vertical direction, is indicated by the white lines.

of the molecules at the bottom of the bilayer interact with water and the ethoxylate chains of the surfactant molecules composing the monolayer. Once formed the bilayer never detaches from the monolayer.

The temperature of the system is maintained at 375 K over the final 66 ns of the simulation. The height of the film at the end of the simulation is different than that at the beginning. This is due to the difference in densities caused by the change in temperature. The average position of the bilayer is seen to drift in the x-direction, wrapping the simulation cell twice over the course of the simulation. This is due to thermal fluctuations and suggests that the lateral interaction between the bilayer and monolayer is weak.

The number of surfactant molecules at the solid-liquid interface remained approximately constant over the course of the simulation. Fig. 6.2 shows a densely packed solid-liquid interface. The graphite substrate is not shown in this figure so that the arrangement of trisiloxane groups can be seen. Only a few of the hydrophilic moieties are also in contact with graphite. Almost no water is seen. This demonstrates the ability of the trisiloxane surfactants to remove interfacial water from hydrophobic substrates. The inverse surface concentration for M(D′E_4OH)M at a hydrophobic solid-liquid interface (octadecyltrichlorosilane) has been measured by ATR FTIR at the CAC to be 49 ± 3 Å^2/molecule [36]. The value at the final time step of the simulation is 61.2 Å^2/molecule, which is nearly identical to the value at initialization. Dong et al. [25] used AFM to examine the adsorption of M(D′E_nOH)M for $n = 6$, 8, and 12 on hydrophilic and hydrophobic substrates. All three surfactants were found to form planar monolayers on graphite and OTS. The packing density on OTS was found to be higher.

The coordinates of the central Si atom (or the Si atom of D′) of each trisiloxane

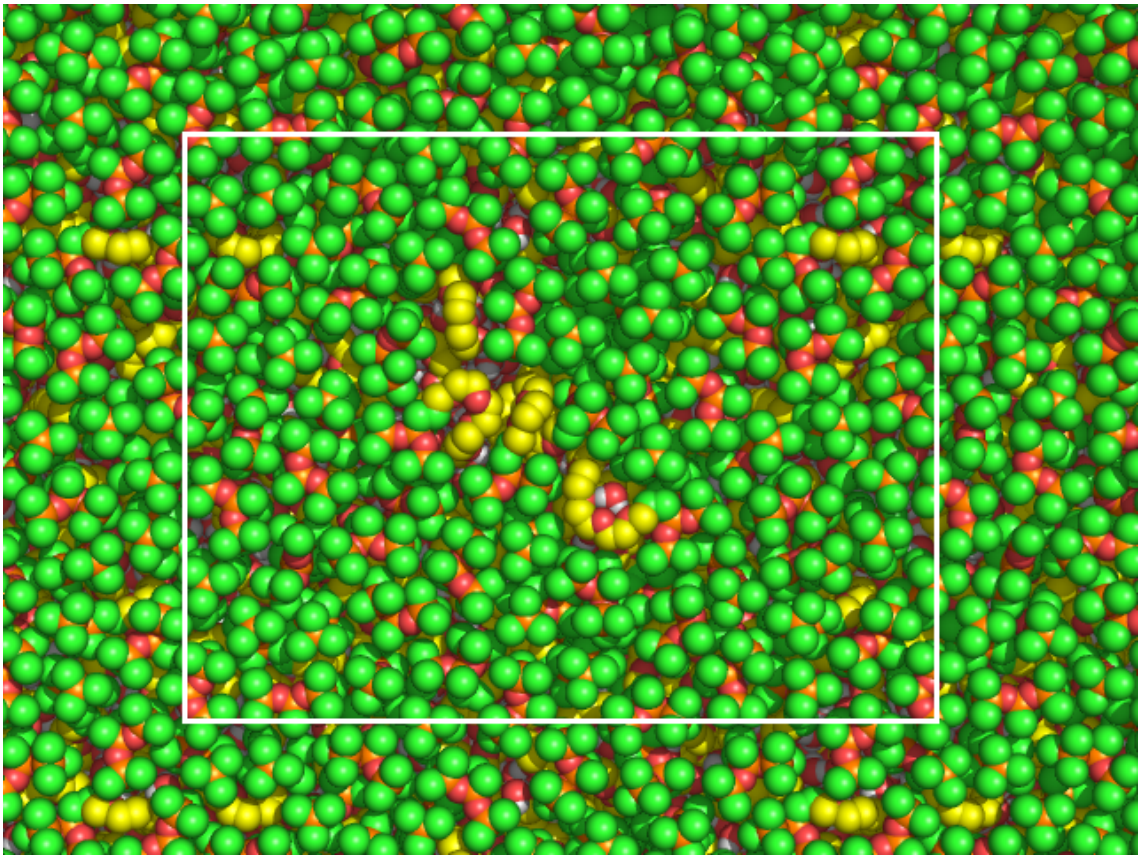

Figure 6.2: Solid-liquid interface of the M($D'E_4OH$)M/H_2O solution at $t = 100$ ns with the graphite substrate removed. The white rectangle indicates the transverse area of the central simulation cell. Same coloring scheme as Fig. 6.1.

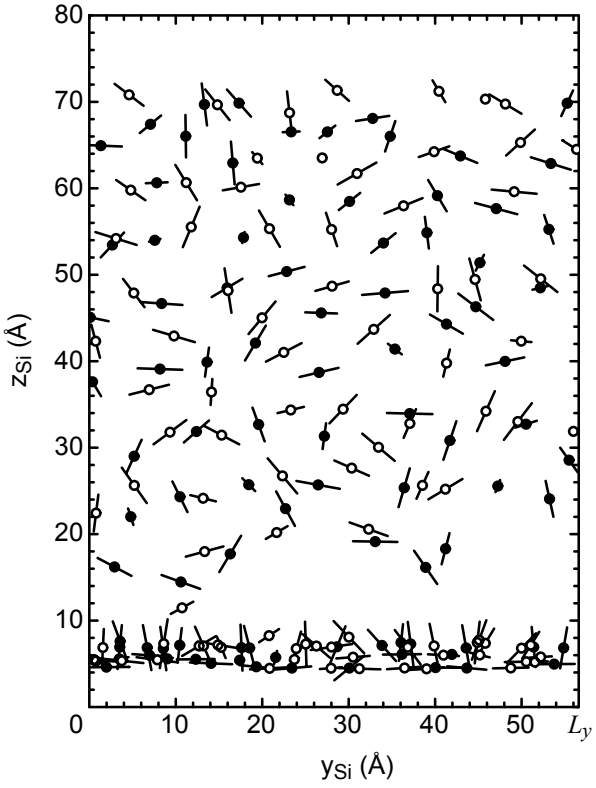

Figure 6.3: Positions of the central Si atoms in the yz-plane. Open/filled circles indicate that the hydrophilic moiety of the molecule extends from the bilayer in the positive/negative x-direction. The line through each circle indicates the orientation of the trisiloxane group.

group are plotted in Fig. 6.3. The orientations of the trisiloxane groups are indicated by the lines. The lines are the projection of the vector formed from the positions of the two terminal Si atoms per trisiloxane group in the yz-plane. Each line has been shifted so that it is centered about the position of the central Si atom. The distribution of lengths is sharply peaked. This indicates that the vast majority of trisiloxane groups are parallel to the yz-plane. There are eighty-seven surfactant molecules between $z = 25$ Å and 65 Å and forty-three of them have their hydrophilic moieties extending from the bilayer in the positive x-direction (open circles in Fig. 6.3). The area per molecule is $(65 \text{ Å} - 25 \text{ Å})(L_y)/87$ molecules $= 52.1$ Å^2/molecule. It will be shown that the bilayer composed of M(D′E_4OH)M molecules is more disordered and less dense than the $C_{12}E_4$ bilayer. There are very few central Si atoms between $z = 10$ Å and 20 Å because this region is occupied by the head groups of the surfactant molecules in the monolayer.

The starting configuration for the $C_{12}E_4$ system (at a concentration of 30.1 wt%) is shown in Fig. 6.4. During the first few nanoseconds of the simulation one of the surfactant molecules is seen to make its way to the liquid-vapor interface. This lone molecule was found to remain at the interface for the duration of the simulation. The bilayer structure is fully formed 54 ns into the simulation. It is interesting to note how the molecules pack. Because the ethoxylate chains form a helix in aqueous solution their projected areas are larger than those of the hydrocarbon chains (this is one reason why the C_mE_n surfactants are not as effective at reducing the interfacial tension as the trisiloxane surfactants). In order for the bilayer to form, the structure must have near zero curvature. To offset the large head group, two surfactants, one from each side of the bilayer, are found to pack their tail groups together thus creating more of a cylindrical shape as opposed to the conical shape

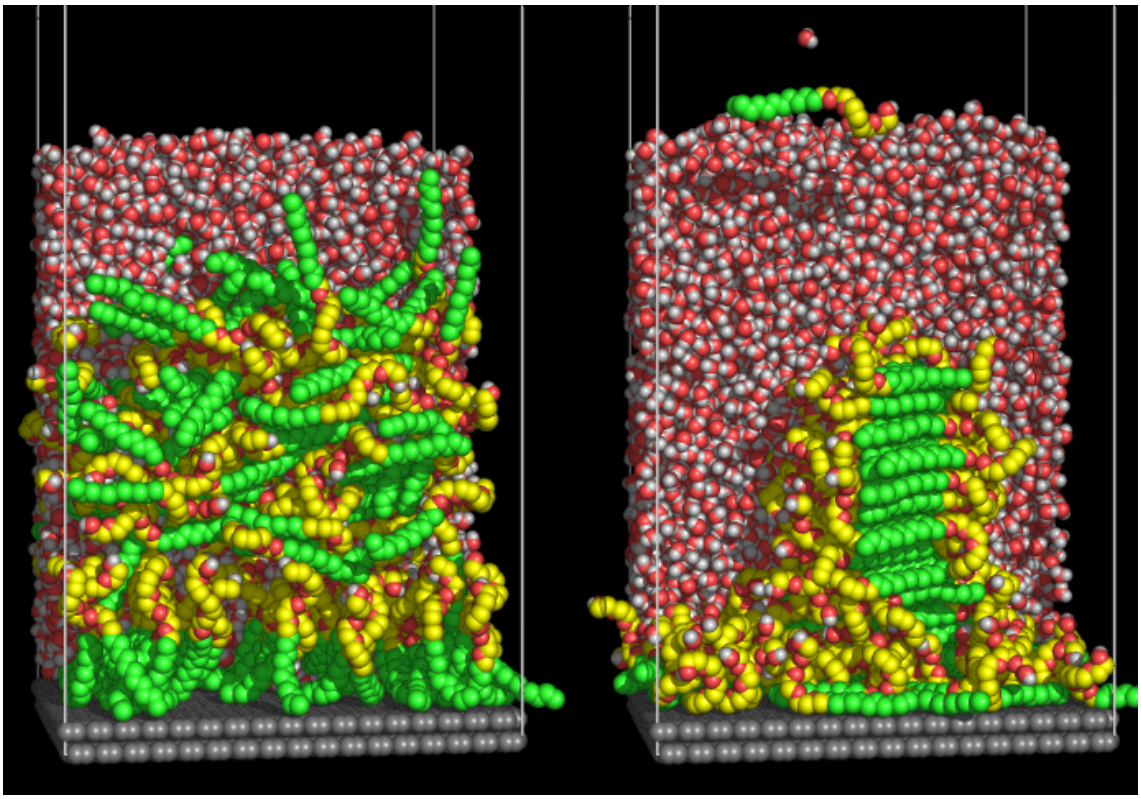

Figure 6.4: Same as Fig. 6.1 except for a $C_{12}E_4/H_2O$ solution.

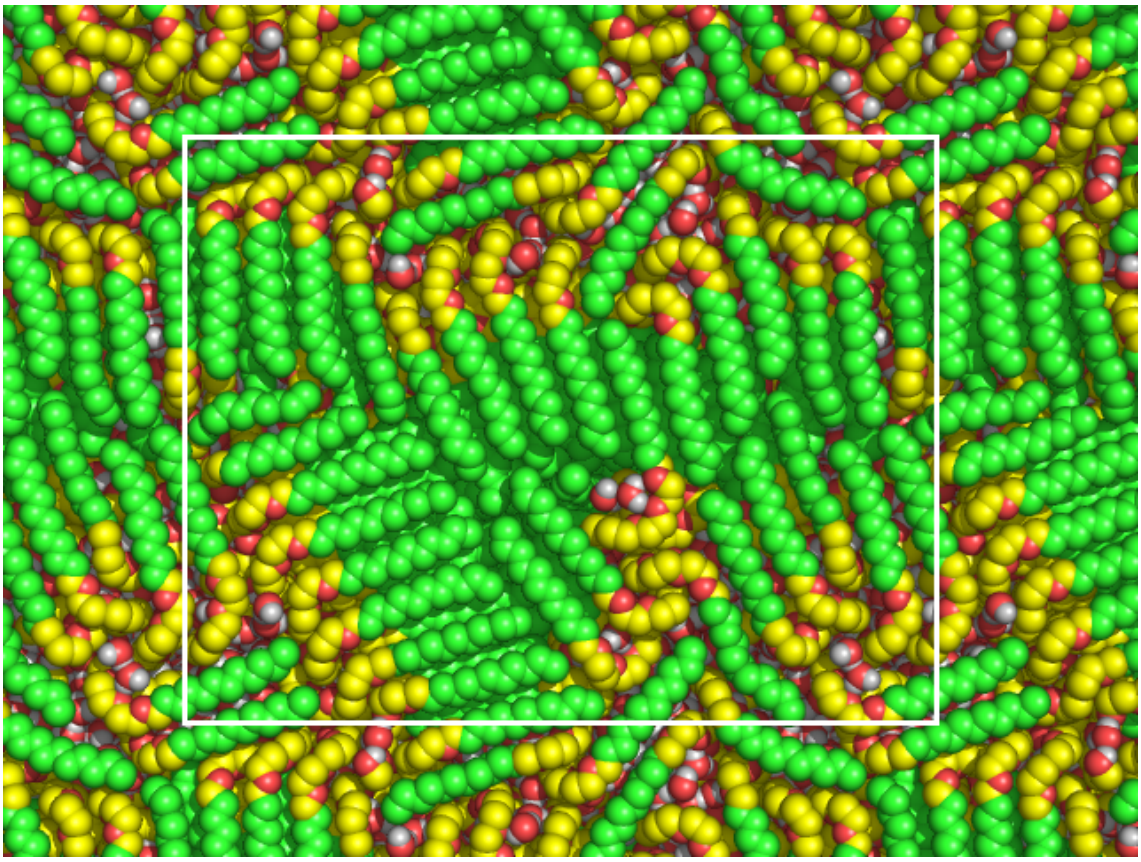

Figure 6.5: Solid-liquid interface for the $C_{12}E_4/H_2O$ solution at $t = 100$ ns with the graphite substrate removed. Same coloring scheme as Fig. 6.1.

of a single molecule. The $C_{12}E_4$ bilayer forms in the yz-plane with a height of 55 Å and a thickness of 30 Å. The result of this simulation is in agreement with the experimental work of Tiddy and coworkers [194] who predict the L_α phase for a 30.1 wt% solution at room temperature (Fig. 5 of Ref. [194]).

The behavior at the solid-liquid interface for the $C_{12}E_4/H_2O$ solution is quite different than that for the $M(D'E_4OH)M/H_2O$ solution. At initialization the surfactant backbones were normal to the substrate, but after less than a nanosecond they became mostly parallel. The solid-liquid interface of the final configuration of the simulation is shown in Fig. 6.5. The hydrocarbon chains are found to be lying down

on the graphite substrate. The hydrophilic moieties of each of these molecules are also in contact with the substrate. However, they are directed upward which allows the oxygen atoms of the ethoxylate chains to form bridged hydrogen bonds with water. The surfactant molecules have removed most of the interfacial water with there being fewer than ten water molecules per simulation cell. Many of the $C_{12}E_4$ molecules are aligned with their neighbors. This arrangement maximizes the van der Waals interaction between the hydrocarbon tails and allows water molecules to form hydrogen bonds with the head groups. These domains consist of up to roughly ten surfactants. The area per molecule for $C_{12}E_4$ at a hydrophobic solid-liquid interface has been measured to be 73 ± 4 Å^2/molecule [36] and 51 Å^2/molecule [195]. The value at the final time step of the simulation is 108.0 Å^2/molecule. Svitova et al. [23] studied the adsorption of $C_{12}E_3$ on graphite. For surfactant concentrations above the critical wetting concentration, the authors found hemicylinders and bilayers adsorbed on the substrate. The difference in surface concentration between the simulation and experiments may be due to the initial configuration of the system. If the simulation were initialized with more $C_{12}E_4$ molecules at the solid-liquid interface the lateral interactions may have been strong enough to maintain the monolayer. It may also be that the time scale for monolayer formation is far longer than the length of the simulation.

The average y- and z-positions of the atoms composing the hydrocarbon chain of each $C_{12}E_4$ molecule are denoted y_{HC} and z_{HC}, respectively. These coordinates are plotted in Fig. 6.6 for the final configuration of the simulation. The molecules are seen to form layers with a spacing between the layers of roughly 5 Å. From $z = 22$ to 52 Å, a triangular lattice with many defects is observed. Of the eighty-four molecules in this region thirty-seven have their hydrophilic moieties extending

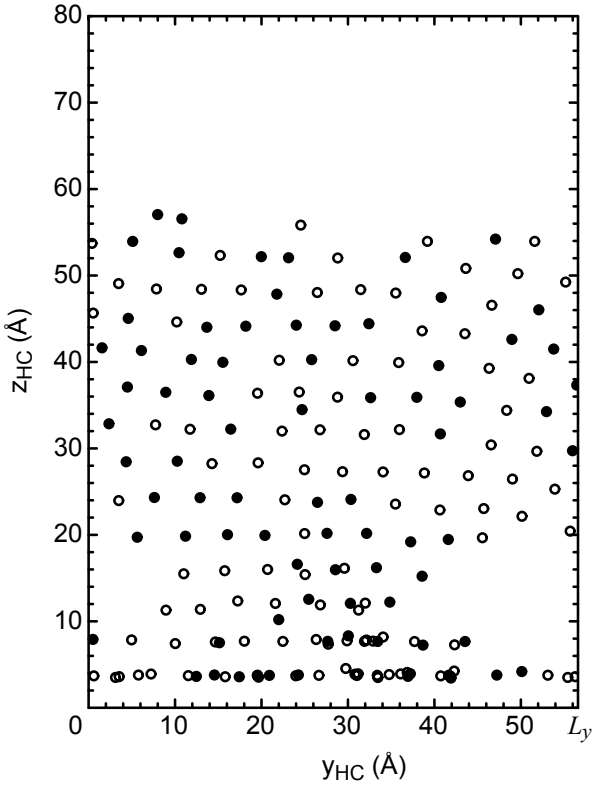

Figure 6.6: The average y- and z-coordinates of the atoms composing the hydrocarbon chain for each $C_{12}E_4$ molecule are shown in the yz-plane. Open/filled circles indicate that the hydrophilic moiety of the molecule extends from the bilayer in the positive/negative x-direction. The top and bottom planes of fixed atoms are located at $z = 0$ and -3.41 Å, respectively.

from the bilayer in the positive x-direction. The area per molecule over this region is 40.4 Å^2/molecule. If the molecules are assumed to form a monolayer instead of a bilayer then the area per molecule is 20.2 Å^2/molecule, which is very close to the value for SAMs of 21.4 Å^2/molecule.

6.3.2 Properties of the Liquid-Vapor Interface

Using Eqn. 6.2, the surface tension for pure water was found to be 58 mN/m. For the same water model, Ismail et al. [165] reported a value of 55.4 mN/m using the pressure-integration method and 49.9 mN/m using the capillary wave method. These values are roughly 20% lower than the experimental value of 72 mN/m.

The surface tension for the M(D′E_4OH)M/H_2O system is shown in Fig. 6.7a at room temperature for 91.5, 76.2, 65.3, and 57.2 Å^2/molecule. The solid curve in this figure is the experimental data [35]. The computed surface tension values overestimate the experimental values for all surface concentrations. However, the surface tension is seen to significantly decrease at the smallest area per molecule, so qualitative agreement is seen. An additional simulation was conducted at a higher temperature. For $T = 350$ K, the tension at the highest coverage was found to decrease to 43 ± 12 mN/m.

The side view of the M(D′E_4OH)M monolayer at 57.2 Å^2/molecule is shown in Fig. 6.8. The two monolayers are separated by a large region of bulk water. The trisiloxane groups are displaced from water while the hydrophilic chains form hydrogen bonds with water. The top view of the monolayer is shown in Fig. 6.9. The maximum packing concentration of M(D′E_4OH)M at the liquid-vapor interface is 53.4 Å^2/molecule [35]. While the simulation was conducted with a surface concentration slightly below the maximum packing value, Fig. 6.9 indicates that the

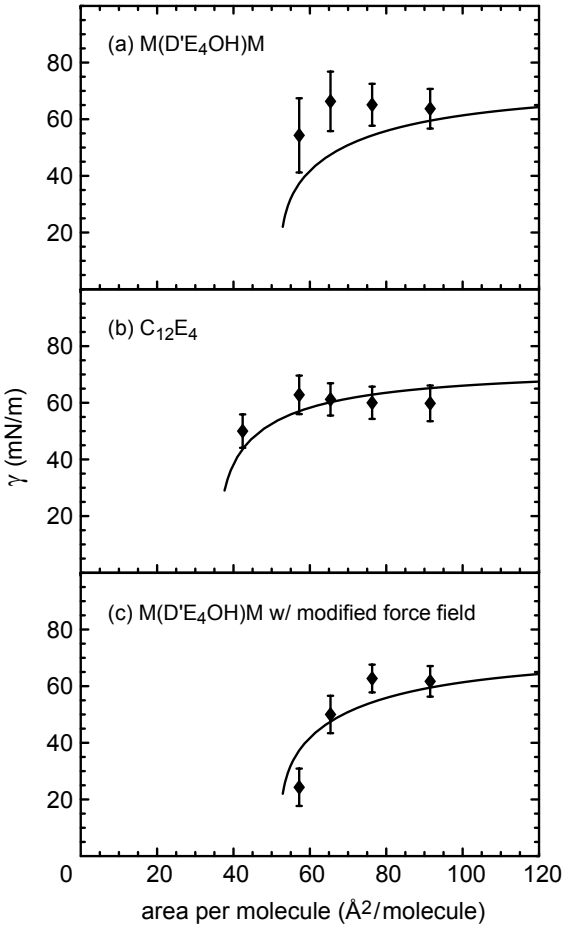

Figure 6.7: Adsorption isotherms at 298.15 K for monolayers of M(D′E_4OH)M and $C_{12}E_4$.

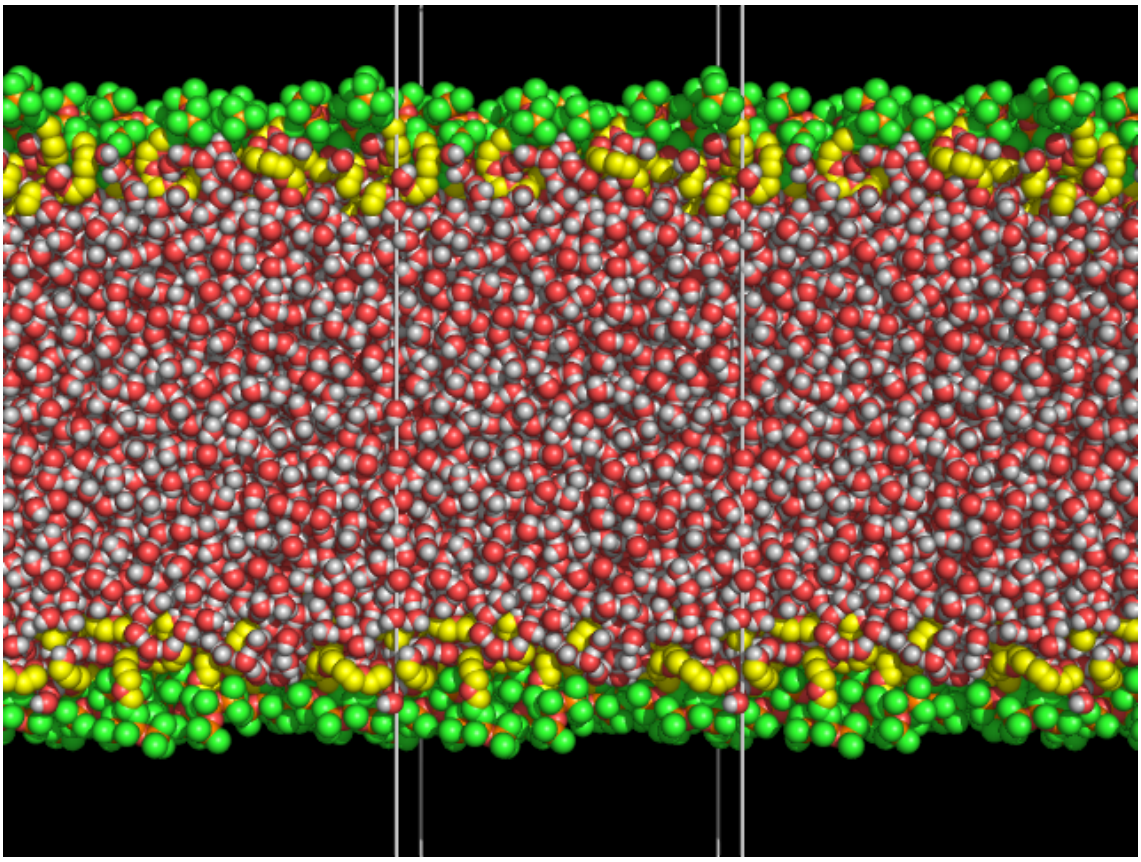

Figure 6.8: Side view of a M(D′E_4OH)M monolayer at 298.15 K with an inverse surface concentration of 57.2 Å^2/molecule. The central simulation cell, which is not completely shown in the vertical direction, is indicated by the white lines. Same coloring scheme as Fig. 6.1.

monolayer is densely packed with less than five water molecules visible.

The surface tension for the $C_{12}E_4/H_2O$ system is shown in Fig. 6.7b. Because $C_{12}E_4$ has a lower maximum packing concentration, an additional simulation with an area per molecule of 42.4 Å^2/molecule was also run. All five data points are within one standard deviation of the experimental data. As with the trisiloxane simulations, the surface tension is found to be essentially constant until the smallest inverse surface concentration is reached.

These simulations provide pictures of the interfacial surfactant phase behavior.

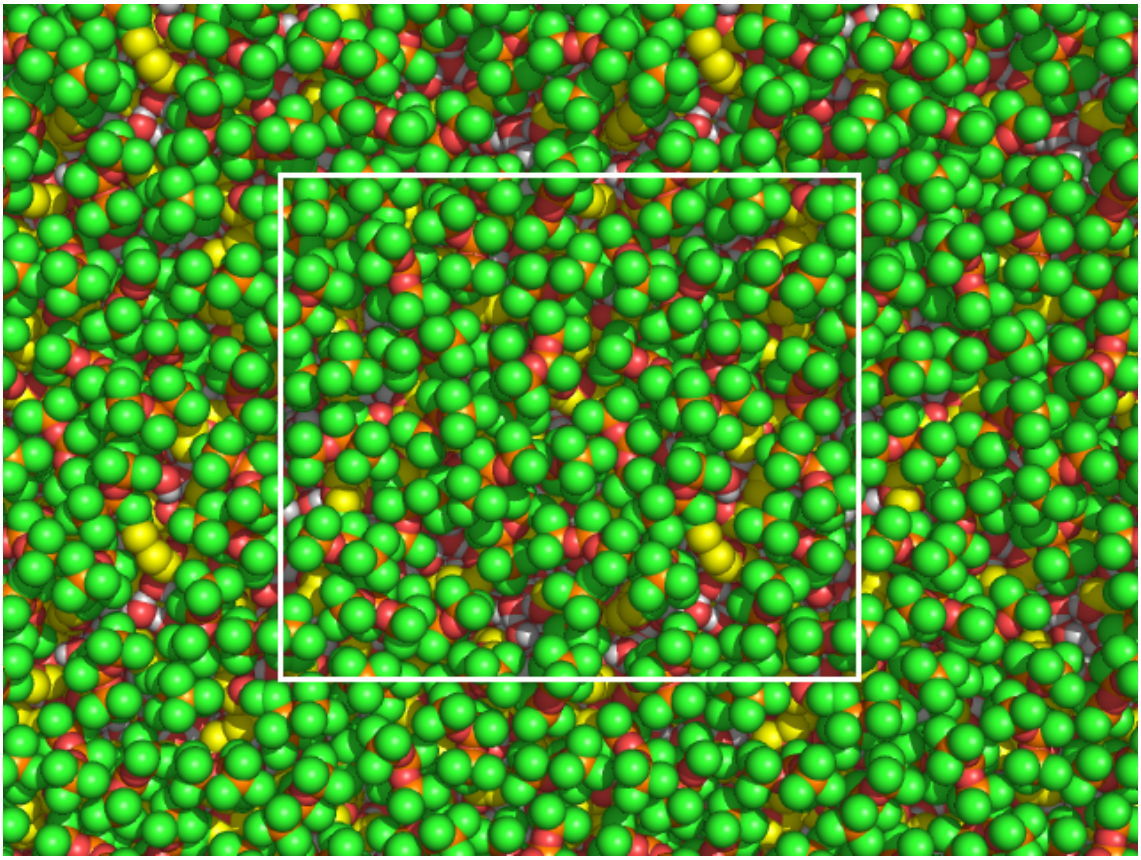

Figure 6.9: Same as Fig. 6.8 except the top view is shown.

At low surface concentrations many of the chains are found to be lying down, which is consistent with a gaseous phase. At the highest coverage the hydrocarbon chains are found to align in a given direction and with a common tilt angle of approximately 30°. This behavior is very similar to that of self-assembled monolayers [62].

The side view of the $C_{12}E_4$ monolayer at 57.2 Å^2/molecule is shown in Fig. 6.10. The maximum packing concentration of $C_{12}E_4$ at the liquid-vapor interface has been reported as 38 Å^2/molecule [175] and 44 ± 3 Å^2/molecule [176]. In Fig. 6.11, the monolayer is seen to have large areas where water is exposed to air. The surfactant molecules have clustered together to maximize the van der Waals interaction between the hydrocarbon chains. The head group of each chain is found to be interacting with water. For the same value of the area per molecule the M(D′E_4OH)M and $C_{12}E_4$ systems are quite different.

Additional simulations were conducted with a modified force field for the trisiloxane case. The Lennard-Jones parameters for the Si and O atoms of the hydrophobe were replaced with parameters for methylene from the OPLS-UA force field. This leads to a weaker interaction. The charge on each atom was made zero while the bond lengths, valence angles, and dihedrals were left unchanged. By doing this we are essentially replacing the trisiloxane chain with a hydrocarbon chain. The simulation results for the modified force field are shown in Fig. 6.7c. Much better agreement is seen when compared to the same experimental data for M(D′E_4OH)M. For instance, γ at the highest coverage is 21 mN/m compared to the experimental value of 22 mN/m.

It is tempting to try to explain the lack of spreading of the surfactant-laden drops in Chapter 5 in terms of the results presented here, but such an explanation can not be made. The surfactant-laden drops did not spread at high surface concentrations

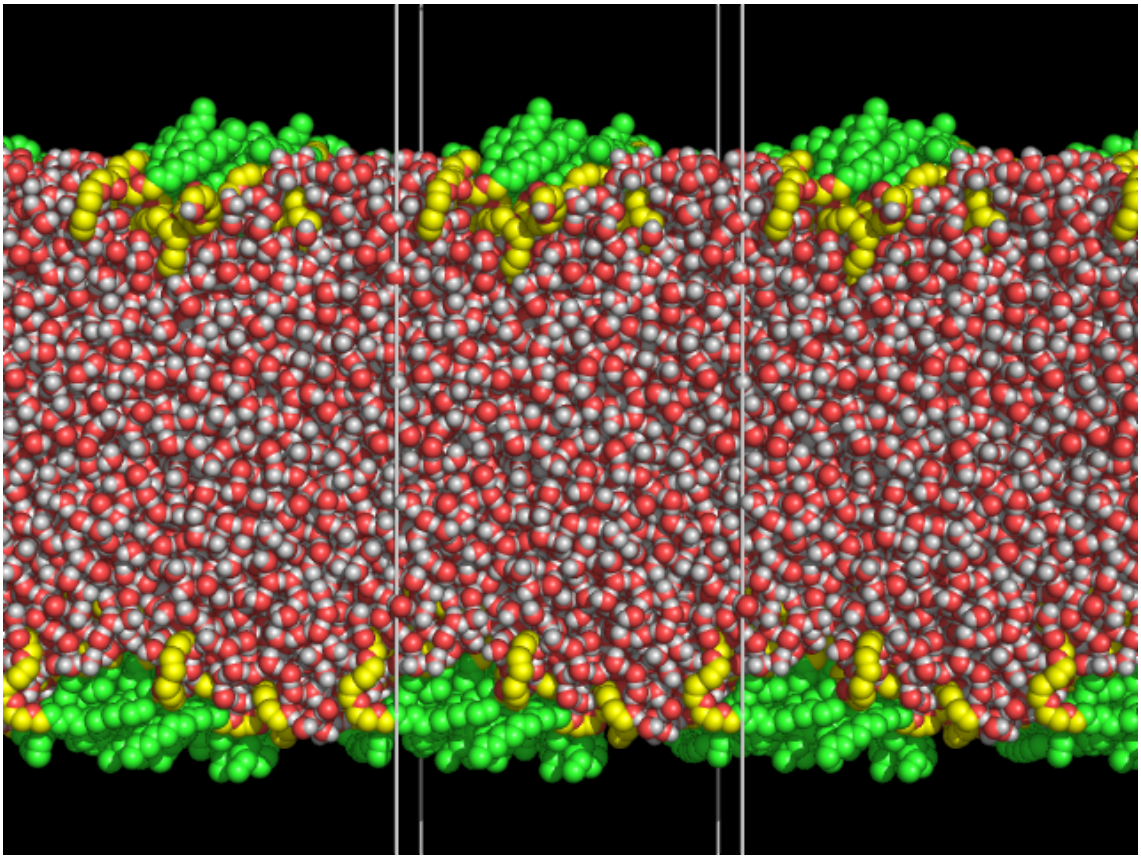

Figure 6.10: Side view of a $C_{12}E_4$ monolayer at 298.15 K with an inverse surface concentration of 57.2 $Å^2$/molecule. The central simulation cell, which is not completely shown in the vertical direction, is indicated by the white lines. Same coloring scheme as Fig. 6.1.

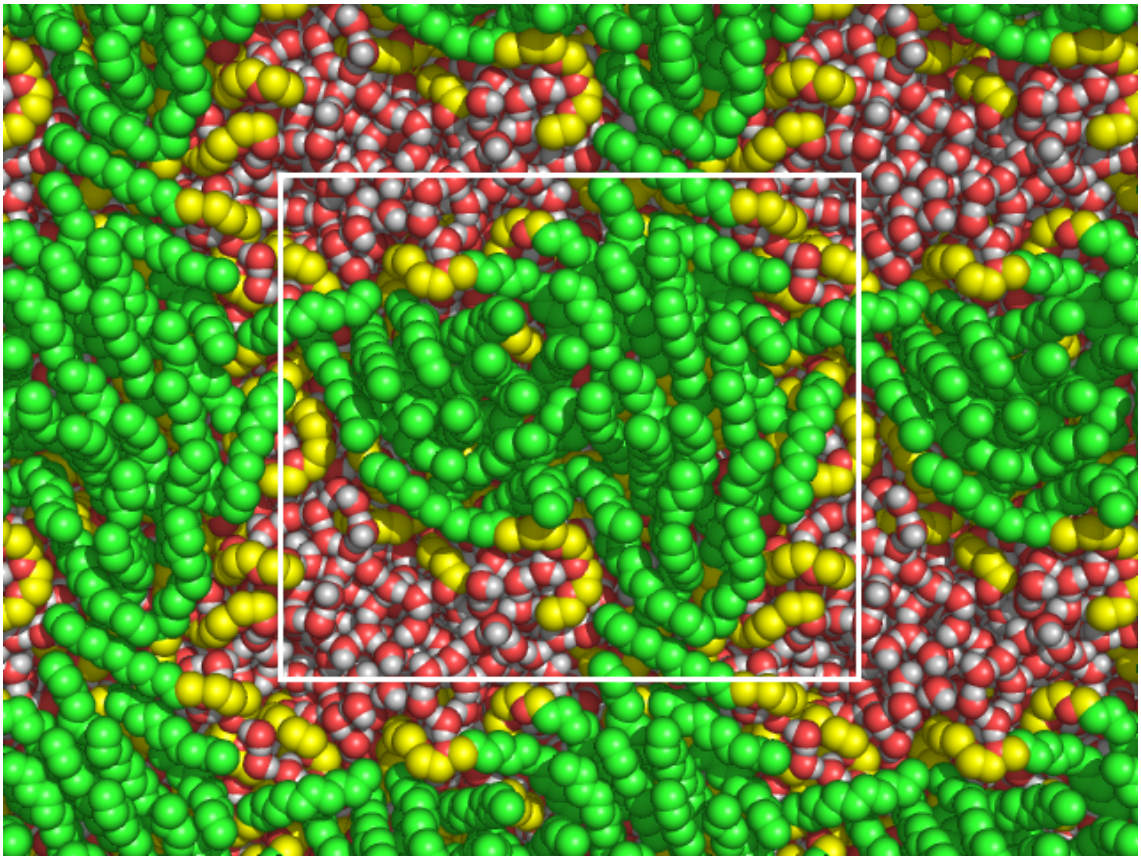

Figure 6.11: Same as Fig. 6.10 except the top view is shown.

because the drops were too small. Also, the surface tension values computed here were for planar interfaces. In the drop wetting simulations the curvature of the drops is large and may influence γ.

6.4 Conclusions

The bulk and interfacial behavior of M(D′E_4OH)M/H_2O and $C_{12}E_4$/H_2O solutions have been examined using parallel molecular dynamics simulations. An initially uniform aqueous solution of trisiloxane surfactant molecules with four ethylene oxide groups was shown to self-assemble into a bilayer in tens of nanoseconds. The self-assembly was promoted at early times by the interaction of the surfactant aggregate and the surfactant monolayer at the graphite-solution interface. Similar results were found for the alkyl polyethoxylate surfactant which is consistent with the experimentally determined phase diagram. The pressure integration method was used for the two surfactant systems to obtain the adsorption isotherms at room temperature. The simulations showed that the surfactants did not reduce the liquid-vapor tension until the highest surface concentration was reached. A modified force field for the superspreading surfactant resulted in better agreement with the experimental data. One possible key to the mechanism of superspreading is the formation of a reverse bilayer at the droplet edge. Since the correct phase behavior was seen in this study it is possible that drop wetting simulations may also predict the reverse bilayer when the correct system size and geometry are used.

Chapter 7

Summary and Future Work

In Chapter 3, the water contact angle of a homogeneous self-assembled monolayers was computed for different values of χ_p. The computed values showed good agreement with experimental data. The SPC/E water model was used for these simulations. Because this model has a larger water-water interaction strength it predicts larger contact angles in comparison to other simple, three-site models. Future work should quantify this difference. That is, how do the computed values of the water contact angle change when the SPC or TIP-3P model is used.

The line tension was computed for monolayers with $\chi_p = 0$ and 0.25 in Chapter 3. The line tension for the more hydrophilic monolayers was not found because large drop sizes were needed to ensure that the height of the drop was larger than the sum of the interfacial thicknesses. Additional CPU time would allow for the calculation of these values with no change to the simulation protocol. Molecular simulation provides a reliable way to determine τ because the system is guaranteed to be free of contaminants and the substrate can be made atomically-smooth and homogeneous.

In Chapter 4, the motion of a pure liquid droplet on a wetting gradient was examined. These simulations considered a droplet on a flat substrate in air. With lab-on-a-chip devices in mind, studies of droplet motion between parallel wetting gradients should be carried out. In real systems it is likely that the fluid will be confined to a channel instead of on a single substrate in air where it may evaporate or become contaminated. The relationship between droplet speed and the distance between the gradient surfaces could be compared to simulation data. And the polar terminal group (e.g., $-OH$, $-NH_2$, or $-CO_2H$) of the monolayer should be varied to determine its effect on the motion of the droplet. Experimental work in the area of controlling and studying fluids on the nanoscale is far behind the simulation and theoretical work.

In previous Lennard-Jones studies of the wetting of hydrophobic substrates by surfactant-laden droplets and in the present study, which used potential functions for real materials, many of the initial droplet configurations had all the surfactant at the liquid-vapor interface. If these systems follow a simple wetting theory based on the Young equation then each droplet is expected to spread until the surface forces at the contact line balance. As the droplet spreads the area per molecule of the liquid-vapor and solid-liquid interfaces is reduced. For continued spreading the surface concentrations must be maintained at values close to the maximum packing concentration. In the previous wetting simulations there is no way for this to happen. Attempts to load the bulk of the droplet with additional surfactant fail because of the long times needed for diffusion and adsorption. Also, as surfactant is added to the bulk the weight percentage of surfactant soon exceeds that of water.

If these wetting studies are continued for either Lennard-Jones or real materials they should be done with cylindrical droplets and simple substrate models. With

such choices it may be possible to load surfactant on the surface as well as in the bulk of the droplet and see additional spreading. However, given the large area to volume ratios of these droplets the additional spreading will not be dramatic. The advantage of the cylindrical shape over that of the spherical is that more solvent particles can be simulated for the same surface concentration of surfactant and CPU time. The fluid should interact with the substrate through a simple, corrugated 9-3 potential unless it is necessary to consider polar surfaces in which case the Coulomb potential is unavoidable.

Droplet wetting simulations to date have followed what one might call the direct or naïve approach where a surfactant-laden spherical droplet in the vicinity of a solid substrate is allowed to spread freely. Different lines of thinking are needed to overcome the limitations of the direct approach. One strategy proposed by J. Koplik to simulate a bilayer at the spreading edge of a trisiloxane droplet without simulating the entire droplet is shown in Fig. 7.1. The solution is confined between the substrate and two additional hydrophobic walls, which are fixed in place. A narrow region that is a few angstroms greater than the predicted bilayer thickness for the surfactant is left open for the bilayer to pass through. Preliminary simulations of this system indicate that it may suffer from the same problems as the droplet wetting simulations. That is, as the fluid makes its way out of the reservoir the surface concentrations decrease due to the area expansion and spreading ceases. Long simulation times are needed for more surfactant to diffuse and adsorb at the interfaces. Future attempts may consider a highly concentrated surfactant solution. The monolayer was created with $\chi_p = 0.25$.

Preliminary simulations of neat M(D′E_4OH)M droplets on methyl- and hydroxyl-terminated SAMs have been conducted. The number of surfactant molecules per

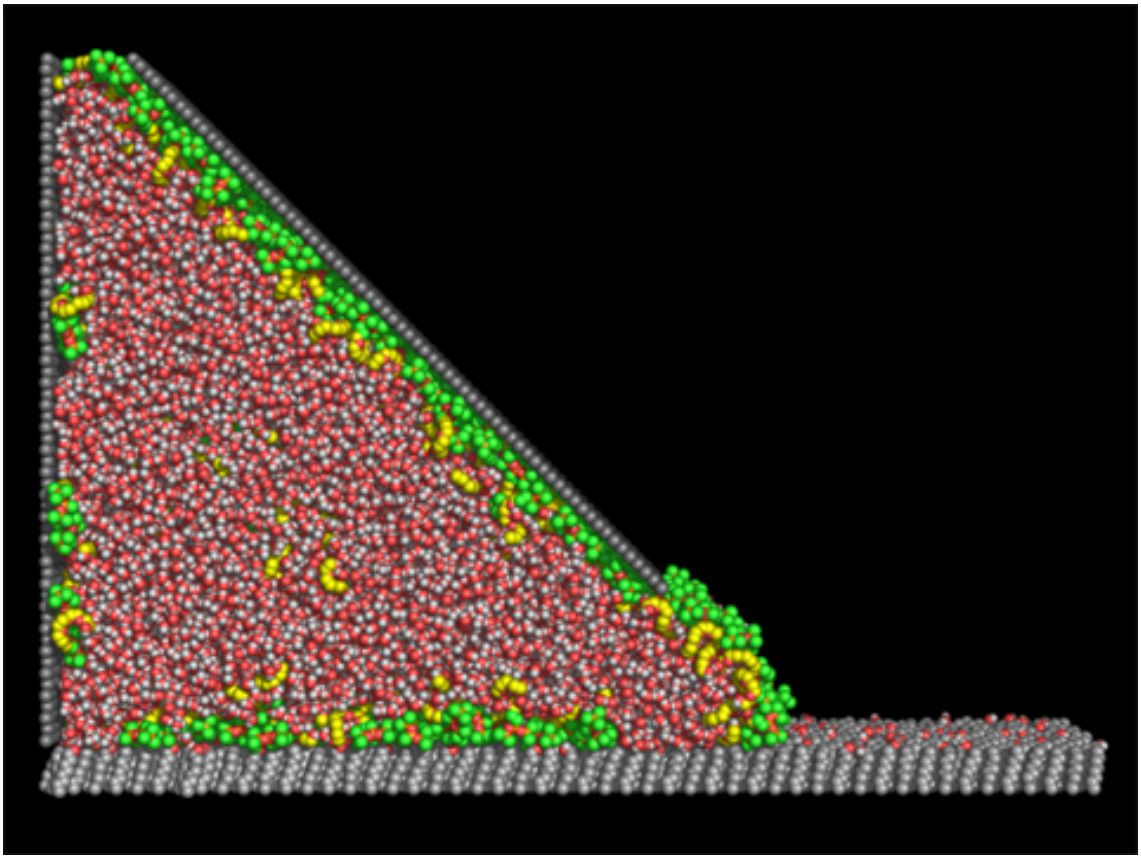

Figure 7.1: A wetting system with additional walls that are designed to promote the formation of a bilayer.

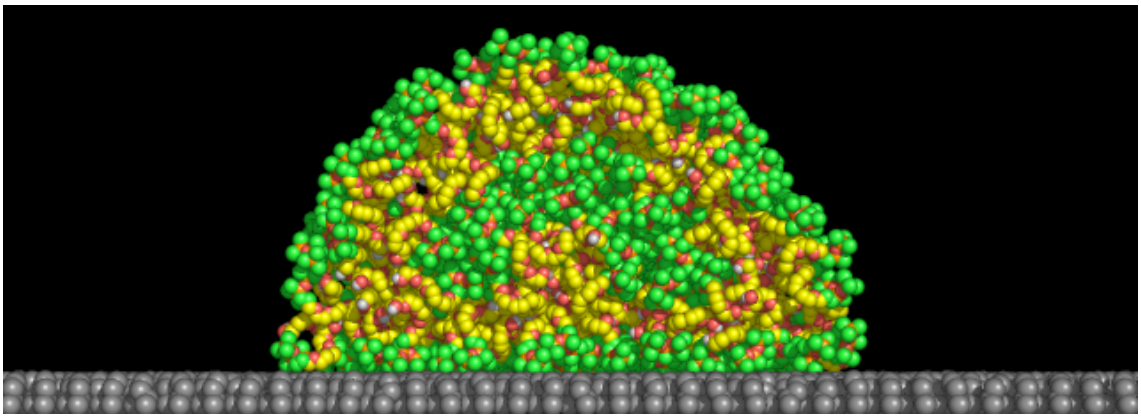

Figure 7.2: Cross-sectional view of a neat droplet of 500 M(D′E_4OH)M molecules at equilibrium on a methyl-terminated SAM at 450 K. The 2000 water molecules in the simulation are not shown. Same coloring scheme as Fig. 6.1.

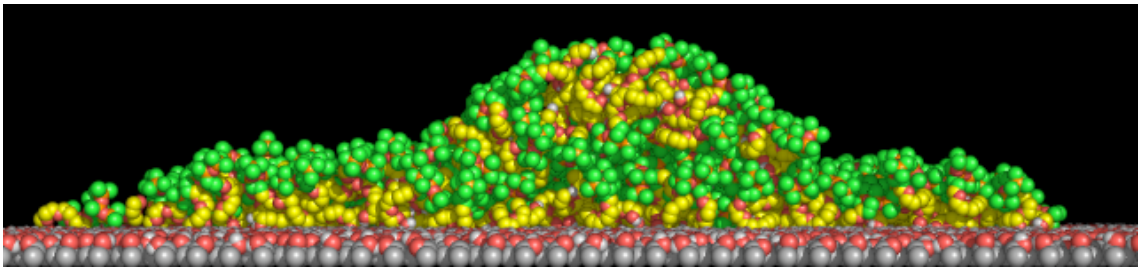

Figure 7.3: Same as Fig. 7.2 except for a hydroxyl-terminated SAM.

droplet was 500. Cases with and without water were considered. None of the droplets spread appreciably at room temperature. When the temperature was increased to 450 K the droplet with water on the hydrophobic substrate gave a layered structure (Fig. 7.2) and the droplet with water of the hydrophilic substrate gave a sand pile-shape (Fig. 7.3). Similar profiles at room temperature were found for M(D′E_8OH)M by Tiberg and Cazabat (Figs. 2a and 2d of Ref. [28]).

The initially randomly-located surfactant molecules of solutions of M(D′E_4OH)M/H_2O and $C_{12}E_4/H_2O$ on graphite were found to form bilayer structures in tens of nanoseconds at 298.15 K. A similar simulation of $C_{12}E_8/H_2O$ solution at a concentration of 24.9 wt%, which is known to form spherical micelles (Fig. 8 of Ref. [194]), was

started but never finished because the CPU time allocation expired. This simulation should be continued to see if a micelle is formed.

The adsorption isotherm for each surfactant system was determined. The simulation results for the trisiloxane surfactant overestimated the surface tension. When the trisiloxane group was replaced with a hydrocarbon chain (while retaining the original structure) the results showed better agreement with experiment. A force field for polydimethylsiloxane (PDMS) was used to describe the interaction between trisiloxane groups [169]. Sides et al. [196] point out that this force field was not optimized for bulk PDMS. Additional force fields for PDMS are available but they either use non-standard potentials [197] or explicit hydrogen atoms [198, 196, 199, 200]. Future work may focus on validating the surfactant force field or developing a new one. At a minimum the force field should reproduce the liquid density and the enthalpy of vaporization. A simulation in the isobaric-isothermal ensemble would produce these values. The mass density of various trisiloxanes may be found in Ref. [7]. And the enthalpy of vaporization is $\Delta H^{vap} \approx -E_{liq}/N + RT$, where E_{liq} is the potential energy of the liquid, N is the number of molecules, R is the universal gas constant, and T is the temperature.

Binary mixtures of alkyl polyethyoxylates and linear alcohols have been shown to reduce the liquid-air tension to low values. For instance, a mixture of $C_{12}E_8$ and $C_{12}E_0$ at the appropriate concentrations reduce the water-air tension to $\sim$22.5 mN/m at room temperature. Molecular dynamics simulation may be used to study the structure of these interfaces to gain a deeper understanding of the synergism.

Appendix A

Surfactant Force Field

The alkyl polyethoxylate surfactants are described by the OPLS-UA force field while the trisiloxane surfactants are described by this and a second force field [169]. To prevent hydrogen bonds from forming between the hydrogen atom of the hydroxyl group with the oxygen atom of the adjacent ethoxylate group (i.e., a 1–5 interaction) the dihedral potential coefficient for the H–O–C–C angle was increased by a factor of ten. The TraPPE-UA force field solves this problem by introducing a repulsive interaction between the two atoms [201].

Bond	Length (Å)
O–H^a	1.000
O–H^b	0.945
CH_2–O^{b,e}	1.430
CH_2–CH_2^c	1.516
CH_2–O^c	1.410
CH_2–CH_2^e	1.530
CH_2–CH_3^e	1.530
CH_2–Si^d	1.880
Si–CH_3^d	1.880
Si–O^d	1.600

Valence	k_θ	θ_0 (°)
H–O–H^a	–	109.47
H–O–CH_2^b	110.02	108.5
O–CH_2–CH_2^b	100.09	108.0
CH_2–O–CH_2^c	124.20	112.0
O–CH_2–$CH_2^{c,e}$	100.00	112.0
CH_2–CH_2–$CH_2^{c,e}$	124.20	112.0
CH_2–CH_2–CH_3^e	124.20	112.0
CH_2–CH_2–Si^d	124.20	112.0
CH_2–Si–CH_3^d	99.94	109.5
CH_2–Si–O^d	99.94	109.5
Si–O–Si^d	28.28	144.0
O–Si–O^d	188.98	109.5
CH_3–Si–O^d	99.94	109.5
CH_3–Si–CH_3^d	99.94	109.5

The valence potential energy is given by $U = \frac{k_\theta}{2}(\theta - \theta_0)^2$.
k_θ is given in units of kcal/mol/rad^2.

Table A.1: Bond lengths and valence angles. ^{a}water, ^{b}alcohol group, ^{c}ethoxylate group, ^{d}trisiloxane group, and ^{e}hydrocarbon.

Dihedral	V_1	V_2	V_3
H–O–CH_2–CH_2^b	12.550	0.0	0.0
O–CH_2–CH_2–$CH_2^{b,c}$	0.702	−0.212	3.060
O–CH_2–CH_2–O^c	0.702	−0.212	3.060
CH_2–O–CH_2–$CH_2^{c,e}$	4.744	−1.398	2.140
O–CH_2–CH_2–$CH_2^{c,e}$	1.411	−0.271	3.145
CH_2–CH_2–CH_2–CH_2^e	1.411	−0.271	3.145
CH_2–CH_2–CH_2–CH_3^e	1.411	−0.271	3.145
CH_2–CH_2–CH_2–Si^e	1.411	−0.271	3.145
CH_2–CH_2–Si–CH_3^e	1.411	−0.271	3.145
CH_3–CH_2–Si–O^e	1.411	−0.271	3.145
CH_2–Si–O–Si^d	0.0	0.0	1.801
Si–O–Si–CH_3^d	0.0	0.0	1.801
O–Si–O–Si^d	0.0	0.0	1.801
The dihedral potential energy is given by $U = \frac{V_1}{2}(1+\cos\phi) + \frac{V_2}{2}(1-\cos 2\phi) + \frac{V_3}{2}(1+\cos 3\phi)$. V_i are given in units of kcal/mol.			

Table A.2: Dihedral angle parameters for the surfactant molecules. [a]water, [b]alcohol group, [c]ethoxylate group, [d]trisiloxane group, and [e]hydrocarbon.

Nonbonded i–i	σ_{ii} (Å)	ϵ_{ii}	q_i (e)
H–H^a	0.0	0.0	0.4238
O–O^a	3.166	650.2	−0.8476
H–H^b	0.0	0.0	0.265
O–O^b	3.070	711.8	−0.700
CH_2–CH_2^b	3.905	493.9	0.435
CH_2–CH_2^c	3.905	493.9	0.0
O–O^c	3.047	817.8	−0.580
Si–Si^d	3.385	2448.0	0.300
CH_3–CH_3^d	3.790	753.2	0.0
O–O^d	2.960	849.3	−0.300
CH_2–CH_2^d	3.905	493.9	0.0
CH_3–CH_3^e	3.905	732.5	0.0
C–C^f	3.214	236.3	0.0

The Lennard-Jones potential energy is given by $U = 4\epsilon_{ij}[(\sigma_{ij}/r_{ij})^{12} - (\sigma_{ij}/r_{ij})^6]$.
ϵ_{ij} are given in units of J/mol.
The Coulomb interaction is $(4\pi\epsilon_0)^{-1} q_i q_j r_{ij}^{-1}$.

Table A.3: Lennard-Jones and Coulomb parameters for the surfactant molecules. ^{a}water, ^{b}alcohol group, ^{c}ethoxylate group, ^{d}trisiloxane group, ^{e}hydrocarbon, and ^{f}graphite.

Appendix B

Best-Fit Ellipse

The profile of a sessile drop on a homogeneous substrate is found to be circular by solving the Young-Laplace equation with the static contact angle entering as a boundary condition. This solution procedure is more involved for a drop on a wetting gradient because the profile is no longer axisymmetric and strictly the system is out of equilibrium.

The time-average of the liquid-vapor boundary profile gives a set of points $\{x_i, z_i\}$ describing the droplet profile. These data points are fit to an ellipse in order to obtain the advancing and receding contact angles, the positions of the advancing and receding edges, and the base length. The profile data points are fit to the following:

$$\left[\frac{(x-x_0)\cos\psi-(z-z_0)\sin\psi}{a}\right]^2 + \left[\frac{(z-z_0)\cos\psi+(x-x_0)\sin\psi}{b}\right]^2 = 1, \quad \text{(B.1)}$$

where a is the semimajor axis, b is the semiminor axis, (x_0, z_0) is the center, and ψ

is the angle of rotation. Eqn. B.1 has two solutions for $z(x)$:

$$z(x) = (A \pm D + E)/F, \tag{B.2}$$

where

$$\begin{aligned}
A &= (a^2 + b^2)z_0 \\
B &= a^2 + b^2 - 2(x - x_0)^2 \\
C &= (a - b)(a + b)\cos 2\psi \\
D &= \sqrt{2}ab\sqrt{B + C} \\
E &= (a - b)(a + b)(z_0 \cos 2\psi - (x - x_0)\sin 2\psi) \\
F &= a^2 + b^2 + (a - b)(a + b)\cos 2\psi.
\end{aligned}$$

Data points within 5 Å of the top of the monolayer were ignored because the liquid density varies over this region. Only the positive solution of Eqn. B.2 (i.e., $z(x) = (A + D + E)/F$) was needed for this work.

A nonlinear fitting algorithm was used to find the optimal values of a, b, x_0, z_0, and ψ for each boundary profile considered. Eqn. B.1 can also be solved for $x(z)$. This solution combined with an expression for the substrate height allows one to calculate the positions of the advancing and receding edges of the droplet. The derivative of Eqn. B.2 is needed to calculate the contact angle.

The root-mean-square error is used as a measure of the fit:

$$E = \left[\frac{1}{n}\sum_{i=1}^{n}(z_i - z(x_i))^2\right]^{1/2}, \tag{B.3}$$

where n is the number of data points in the set $\{x_i, z_i\}$. We find for the $N = 2000$ droplet that the minimum, average, and maximum E values are 0.25, 0.45, and 0.64 Å, respectively, while for the $N = 4000$ case we find 0.35, 0.53, and 0.76 Å.

Bibliography

[1] M. Knoche. *Weed Res.*, 34:221, 1994.

[2] P. G. de Gennes. Wetting: statics and dynamics. *Rev. Mod. Phys.*, 57(3):827, 1985.

[3] E. G. Schwartz and W. G. Reid. *Ind. Eng. Chem.*, 56:26, 1964.

[4] K. P. Ananthapadmanabhan, E. D. Doddard, and P. Chandar. *Colloid. Surface.*, 44:281, 1990.

[5] S. Zhu, W. G. Miller, L. E. Scriven, and H. T. Davis. *Colloid. Surface. A*, 90:63, 1994.

[6] M. Gradzielski, H. Hoffmann, P. Robisch, W. Ulbricht, and B. Grüning. *Tenside Surfact. Deterg.*, 27:366, 1990.

[7] M. He, R. M. Hill, Z. Lin, L. E. Scriven, and H. T. Davis. *J. Chem. Phys.*, 97:8820, 1993.

[8] R. M. Hill. *Curr. Opin. Colloid In.*, 3:247, 1998.

[9] R. Wagner, Y. Wu, H. v. Berlepsch, and L. Perepelittchenko. *Appl. Organometal. Chem.*, 14:177, 2000.

[10] X. Li, R. M. Washenberger, L. E. Scriven, and H. T. Davis. *Langmuir*, 15:2267, 1999.

[11] X. Li, R. M. Washenberger, L. E. Scriven, and H. T. Davis. *Langmuir*, 15:2278, 1999.

[12] R. Wagner, Y. Wu, H. v. Berlepsch, F. Rexin, T. Rexin, and L. Perepelittchenko. *Appl. Organometal. Chem.*, 13:621, 1999.

[13] R. Wagner and R. Strey. *Langmuir*, 15:902, 1999.

[14] H. Kunieda, H. Taoka, T. Iwanaga, and A. Harashima. *Langmuir*, 14:5113, 1998.

[15] T. Stoebe, Z. Lin, R. M. Hill, M. D. Ward, and H. T. Davis. *Langmuir*, 12:337, 1996.

[16] T. Stoebe, Z. Lin, R. M. Hill, M. D. Ward, and H. T. Davis. *Langmuir*, 13:7270, 1997.

[17] T. Stoebe, R. M. Hill, M. D. Ward, and H. T. Davis. *Langmuir*, 13:7276, 1997.

[18] T. Stoebe, Z. Lin, R. M. Hill, M. D. Ward, and H. T. Davis. *Langmuir*, 13:7282, 1997.

[19] T. F. Svitova, R. M. Hill, and C. J. Radke. *Langmuir*, 17:235, 2001.

[20] Z. Lin, R. M. Hill, T. Davis, and M. D. Ward. *Langmuir*, 10:4060, 1994.

[21] R. Wagner, Y. Wu, G. Czichocki, H. v. Berlepsch, F. Rexin, and L. Perepelittchenko. *Appl. Organometal. Chem.*, 13:201, 1999.

[22] T. Svitova, R. M. Hill, Y. Smirnova, A. Stuermer, and G. Yakubov. *Langmuir*, 14:5023, 1998.

[23] T. Svitova, R. M. Hill, and C. J. Radke. *Colloid. Surface. A*, 183-185:607, 2001.

[24] L. M. Grant, F. Tiberg, and W. A. Ducker. *J. Phys. Chem. B*, 102:4288, 1998.

[25] J. Dong, G. Mao, and R. M. Hill. *Langmuir*, 20:2695, 2004.

[26] T. Svitova, H. Hoffmann, and R. M. Hill. *Langmuir*, 12:1712, 1996.

[27] T. E. Gentle and S. A. Snow. *Langmuir*, 11:2905, 1995.

[28] F. Tiberg and A. M. Cazabat. *Langmuir*, 10:2301, 1994.

[29] A. M. Cazabat, N. Fraysse, F. Heslot, P. Levinson, J. Marsh, F. Tiberg, and M. P. Valignat. *Adv. Colloid Interface Sci.*, 48:1, 1994.

[30] E. Ruckenstein. *J. Colloid Interface Sci.*, 179:136, 1996.

[31] N. V. Churaev, N. E. Esipova, R. M. Hill, V. D. Sobolev, V. M. Starov, and Z. M. Zorin. *Langmuir*, 17:1338, 2001.

[32] A. D. Nikolov, D. T. Wasan, A. Chengara, K. Koczo, G. A. Policello, and I. Kolossvary. *Adv. Colloid Interface Sci.*, 96:325, 2002.

[33] S. Rafaï, D. Sarker, V. Bergeron, J. Meunier, and D. Bonn. *Langmuir*, 18:10486, 2002.

[34] S. Rafaï and D. Bonn. *Physica A*, 358:58, 2005.

[35] N. Kumar, A. Couzis, and C. Maldarelli. *J. Colloid and Interface Sci.*, 267:272, 2003.

[36] N. Kumar, C. Maldarelli, and A. Couzis. *Colloid. Surface. A*, 277:98, 2006.

[37] T. D. Blake, C. Decamps, J. De Coninck, M. de Ruijter, and M. Voue. *Colloid. Surface. A*, 154:5, 1999.

[38] J. Hautman and M. L. Klein. *Phys. Rev. Lett.*, 67(13):1763, 1991.

[39] M. Lundgren, N. L. Allan, T. Cosgrove, and N. George. *Langmuir*, 18:10462, 2002.

[40] T. Werder, J. H. Walther, R. L. Jaffe, T. Halicioglu, and P. Koumoutsakos. *J. Phys. Chem. B*, 107:1345, 2003.

[41] C. F. Fan and T. Cagin. *J. Chem. Phys.*, 103(20):9053, 1995.

[42] M. Lundgren, N. L. Allan, T. Cosgrove, and N. George. *Langmuir*, 19:7127, 2003.

[43] W. Mar and M. L. Klein. *J. Phys.: Condens. Matter*, 6:A381, 1994.

[44] S. Bandyopadhyay, M. Tarek, M. L. Lynch, and M. L. Klein. *Langmuir*, 16:942, 2000.

[45] Y. C. Kong, D. Nicholson, N. G. Parsonage, and L. Thompson. *J. Chem. Soc., Faraday Trans.*, 90(16):2375, 1994.

[46] Y. C. Kong, D. Nicholson N. G. Parsonage, and L. Thompson. *J. Chem. Soc., Faraday Trans.*, 91(23):4261, 1995.

[47] H. Kuhn and H. Rehage. *J. Phys. Chem. B*, 103:8493, 1999.

[48] Y. Shen, A. Couzis, J. Koplik, C. Maldarelli, and M. S. Tomassone. *Langmuir*, 21:12160, 2005.

[49] M. S. Tomassone, A. Couzis, C. M. Maldarelli, J. R. Banavar, and J. Koplik. *J. Chem. Phys.*, 115:8634, 2001.

[50] M. S. Tomassone, A. Couzis, C. M. Maldarelli, J. R. Banavar, and J. Koplik. *Langmuir*, 17:6037, 2001.

[51] H.-Y Kim, Q. Yin, and K. A. Fichthorn. *J. Chem. Phys.*, 125:174708, 2006.

[52] W. A. Steele. *Surface Science*, 36:317, 1973.

[53] M. P. Allen and D. J. Tildesley. *Computer Simulation of Liquids*. Oxford University Press, New York, 1987.

[54] H. J. C. Berendsen, J. R. Grigera, and T. P. Straatsma. *J. Phys. Chem.*, 91:6269, 1987.

[55] W. G. Hoover. *Physical Review A*, 31(3):1695, 1985.

[56] J. P. Ryckaert, G. Ciccotti, and H. J. C. Berendsen. *J. Comput. Phys.*, 23:327, 1977.

[57] H. C. Andersen. *J. Comput. Phys.*, 52:24, 1983.

[58] V. Krautler, W. F. van Gunsteren, and P. H. Hunenberger. *J. Comput. Chem.*, 22(5):501, 2001.

[59] S. Miyamoto and P. A. Kollman. *J. Comput. Chem.*, 13(8):952, 1992.

[60] G. S. Grest, B. Dunweg, and K. Kremer. *Comput. Phys. Comm.*, 55:269, 1989.

[61] S. Plimpton. *J. Comput. Phys.*, 117:1, 1995.

[62] F. Schreiber. *Progress in Surface Science*, 65:151, 2000.

[63] K. L. Prime and G. M. Whitesides. *J. Am. Chem. Soc.*, 115:10714, 1993.

[64] P. A. DiMilla, J. P. Folkers, H. A. Biebuyck, R. Härter, G. P. López, and G. M. Whitesides. *J. Am. Chem. Soc.*, 116:2225, 1994.

[65] C. Boulas, J. V. Davidovits, F. Rondelez, and D. Vuillaume. *Microelectron. Eng.*, 28:217, 1995.

[66] Y. Xia, X.-M Zhao, and G. M. Whitesides. *Microelectron. Eng.*, 32:255, 1996.

[67] G. K. Jennings and P. E. Laibinis. *J. Am. Chem. Soc.*, 119:5208, 1997.

[68] C. D. Bain, J. Evall, and G. M. Whitesides. *J. Am. Chem. Soc.*, 111:7155, 1989.

[69] C. D. Bain and G. M. Whitesides. *J. Am. Chem. Soc.*, 111:7164, 1989.

[70] C. D. Bain, H. A. Biebuyck, and G. M. Whitesides. *Langmuir*, 5:723, 1989.

[71] J. P. Folkers, P. E. Laibinis, and G. M. Whitesides. *Langmuir*, 8:1330, 1992.

[72] P. Laibinis, R. Nuzzo, and G. Whitesides. *J. Phys. Chem.*, 96:5097, 1992.

[73] J. L. Wilbur, A. Kumar, H. A. Biebuyck, E. Kim, and G. M. Whitesides. *Nanotechnology*, 7(4):452, 1996.

[74] E. W. Wollman, D. Kang, C. D. Frisbie, I. M. Lorkovic, and M. S. Wrighton. *J. Am. Chem. Soc.*, 116:4395, 1994.

[75] J. Y. Huang, D. A. Dahlgren, and J. C. Hemminger. *Langmuir*, 10:626, 1994.

[76] T. A. Jung, A. Moser, H. J. Hug, D. Brodbeck, R. Hofer, H. R. Hidber, and U. D. Schwartzm. *Ultramicroscopy*, 42-44:1446, 1992.

[77] X.-D Xiao, G.-Y Liu, D. H. Charych, and M. Salmeron. *Langmuir*, 11:1600, 1995.

[78] R. D. Piner, J. Zhu, F. Xu, S. Hong, and C. A. Mirkin. *Science*, 283:661, 1999.

[79] M. Preuss and H-J. Butt. *J. Colloid Interface Sci.*, 208:168, 1998.

[80] A. M. Jackson, J. W. Myerson, and F. Stellacci. *Nature Materials*, 3:330, 2004.

[81] L. Bertilsson and B. Liedberg. *Langmuir*, 9:141, 1993.

[82] S. J. Stranick, A. N. Parikh, Y.-T. Tao, D. L. Allara, and P. S. Weiss. *J. Phys. Chem.*, 98:7636, 1994.

[83] S. J. Stranick, S. V. Atre, A. N. Parikh, M. C. Wood, D. L. Allara, N. Winograd, and P. S. Weiss. *Nanotechnology*, 7:438, 1996.

[84] K. Tamada, M. Hara, H. Sasabe, and W. Knoll. *Langmuir*, 13:1558, 1997.

[85] W. A. Hayes, H. Kim, X. Yue, S. S. Perry, and C. Shannon. *Langmuir*, 13:2511, 1997.

[86] S-I. Imabayashi, D. Hobara, and T. Kakiuchi. *Langmuir*, 13:4502, 1997.

[87] S. Imabayashi, N. Gon, T. Sasaki, D. Hobara, and T. Kakiuchi. *Langmuir*, 14:2348, 1998.

[88] S. Arnold, Z. Q. Feng, T. Kakiuchi, W. Knoll, and K. Niki. *J. Electroanal. Chem.*, 438:91, 1997.

[89] T. Kakiuchi, M. Iida, N. Gon, D. Hobara, S-I. Imabayashi, and K. Niki. *Langmuir*, 17:1599, 2001.

[90] P. A. Lewis, R. K. Smith, K. F. Kelly, L. A. Bumm, S. M. Reed, R. S. Clegg, J. D. Gunderson, J. E. Hutchison, and P. S. Weiss. *J. Phys. Chem. B*, 105:10630, 2001.

[91] K. Salaita, A. Amarnath, D. Maspoch, T. B. Higgins, and C. A. Mirkin. *J. Am. Chem. Soc.*, 127:11283, 2005.

[92] P. Hong Phong, V. V. Sokolov, N. Nishi, M. Yamamoto, and T. Kakiuchi. *J. Electroanal. Chem.*, 600:35, 2007.

[93] N. J. Brewer and G. J. Leggett. *Langmuir*, 20:4109, 2004.

[94] A. B. D. Cassie. *Discuss. Faraday Soc.*, 3:11, 1948.

[95] M. Lundgren, N. L. Allan, and T. Cosgrove. *Langmuir*, 23:1187, 2007.

[96] M. H. Adao, M. de Ruijter, M. Voué, and J. De Coninick. *Phys. Rev. E*, 59:746, 1999.

[97] V. M. Samsonov, V. V. Dronnikov, A. A. Volnukhina, and S. D. Muravyev. *Surface Science*, 532:560, 2003.

[98] S. Brandon, N. Haimovich, E. Yeger, and A. Marmur. *J. Colloid Interface Sci.*, 263:3237, 2003.

[99] S. Brandon, A. Wachs, and A. Marmur. *J. Colloid Interface Sci.*, 191:110, 1997.

[100] J. Hautman and M. L. Klein. *J. Chem. Phys.*, 91:4994, 1989.

[101] J. Hautman and M. L. Klein. *J. Chem. Phys.*, 93:7483, 1990.

[102] C. E. D. Chidsey and D. N. Loiacono. *Langmuir*, 6:682, 1990.

[103] N. Camillone, C. E. D. Chidsey, G. y Liu, and G. J. Scoles. *Chem. Phys.*, 98:3503, 1993.

[104] P. Fenter, P. Eisenberger, and K. S. Liang. *Phys. Rev. Lett.*, 70:2447, 1993.

[105] W. Mar and M. L. Klein. *Langmuir*, 10:188, 1994.

[106] M. Sprik, E. Delamarche, B. Michel, U. Rothlisberger, M. L. Klein, H. Wolf, and H. Ringsdorf. *Langmuir*, 10:4116, 1994.

[107] A. J. Pertsin and M. Grunze. *Langmuir*, 10:3668, 1994.

[108] J.-P Bucher, L. Santesson, and K. Kern. *Appl. Phys. A*, 10:979, 1994.

[109] E. Delamarche, B. Michel, Ch. Gerber, D. Anselmetti, H.-J Güntherodt, H. Wolf, and H. Ringsdorf. *Langmuir*, 10:2869, 1994.

[110] G. E. Poirier and M. J. Tarlov. *Langmuir*, 10:2853, 1994.

[111] R. Bhatia and B. J. Garrison. *Langmuir*, 13:4038, 1997.

[112] R. Bhatia and B. J. Garrison. *Langmuir*, 13:765, 1997.

[113] T. Li, I. Chao, and Y. Tao. *J. Phys. Chem. B*, 102:2935, 1998.

[114] B. Rai, P. Sathish, C. P. Malhotra, Pradip, and K. G. Ayappa. *Langmuir*, 20:3138, 2004.

[115] S. Vemparala, B. B. Karki, R. K. Kalia, A. Nakano, and P. Vashishta. *J. Chem. Phys.*, 121(9):4323, 2004.

[116] O. Alexiadis, V. A. Harmandaris, V. G. Mavrantzas, and L. Delle Site. *J. Phys. Chem. C*, 111:6380, 2007.

[117] A. Riposan and G. Liu. *J. Phys. Chem. B*, 110:23926, 2006.

[118] S. R. Holmes-Farley, C. D. Bain, and G. M. Whitesides. *Langmuir*, 4:921, 1988.

[119] O. Dannenberger, K. Weiss, H.-J. Himmel, B. Jager, M. Buck, and C. Woll. *Thin Solid Films*, 307:183, 1997.

[120] D. Frenkel and B. Smit. *Understanding Molecular Simulation*. Academic Press, London, 2nd edition, 2002.

[121] J. C. Phillips, R. Braun, W. Wang, J. Gumbart, E. Tajkhorshid, E. Villa, C. Chipot, R. D. Skeel, L. Kale, and K. Schulten. *J. Comput. Chem.*, 26:1781, 2005.

[122] W. L. Jorgensen. *J. Phys. Chem.*, 90:1276, 1986.

[123] W. L. Jorgensen, J. D. Madura, and C. J. Swenson. *J. Am. Chem. Soc.*, 106:6638, 1984.

[124] T. A. Darden, D. M. York, and L. G. Pederson. *J. Chem. Phys.*, 98:10089, 1993.

[125] U. Essmann, L. Perera, M. L. Berkowitz, T. Darden, H. Lee, and L. Pederson. *J. Chem. Phys.*, 103:8577, 1995.

[126] M. J. de Ruijter, T. D. Blake, and J. De Coninick. *Langmuir*, 15:7836, 1999.

[127] Y. Arima and H. Iwata. *Biomaterials*, 28:3074, 2007.

[128] S. Semal, C. Bauthier, M. Voué, J. J. Vanden Eynde, R. Gouttebaron, , and J. De Coninck. *J. Phys. Chem. B*, 104:6225, 2000.

[129] T. Ederth and B. Leidberg. *Langmuir*, 16:2177, 2000.

[130] S. D. Evans, R. Sharma, and A. Ulman. *Langmuir*, 7:156, 1991.

[131] P. T. Mikulski, L. A. Herman, and J. A. Harrison. *Langmuir*, 21:12197, 2005.

[132] L. Boruvka and A. W. Neumann. *J. Chem. Phys.*, 66:5464, 1977.

[133] A. Amirfazli and A. W. Neumann. *J. Colloid Interface Sci.*, 110:121, 2004.

[134] M. Preuss and H-J. Butt. *Langmuir*, 14:3164, 1998.

[135] A. Amirfazli, A. Keshavarz, L. Zhang, and A. W. Neumann. *J. Colloid Interface Sci.*, 256:152, 2003.

[136] H.-K Guo and H.-P Fang. *Chin. Phys. Lett.*, 22(4):787, 2005.

[137] H. P. Greenspan. *J. Fluid Mech.*, 84:125, 1978.

[138] F. Brochard. *Langmuir*, 5:432, 1989.

[139] M. K. Chaudhury and G. M. Whitesides. *Science*, 256:1539, 1992.

[140] H. Elwing, S. Welin, A. Askendal, U. Nilsson, and I. Lundstrom. *J. Colloid Interface Sci.*, 119:203, 1987.

[141] M. L. Ford and A. Nadim. *Phys. Fluids*, 6(9):3183, 1994.

[142] S. Daniel, M. K. Chaudhury, and J. C. Chen. *Science*, 291:633, 2001.

[143] K. Ichimura, S. Oh, and M. Nakagawa. *Science*, 288:1624, 2000.

[144] S. Daniel and M. K. Chaudhury. *Langmuir*, 18:3404, 2002.

[145] S. Daniel, S. Sircar, J. Gliem, and M. K. Chaudhury. *Langmuir*, 20:4085, 2004.

[146] H. Suda and S. Yamada. *Langmuir*, 19:529, 2003.

[147] Y. Ito, M. Heydari, A. Hashimoto, T. Konno, A. Hirasawa, S. Hori, K. Kurita, and A. Nakajima. *Langmuir*, 23:1845, 2007.

[148] R. S. Subramanian, N. Moumen, and J. B. McLaughlin. *Langmuir*, 21:11844, 2005.

[149] R. G. Cox. *J. Fluid Mech.*, 168:169, 1986.

[150] N. Moumen, R. Shankar Subramanian, and J. B. McLaughlin. *Langmuir*, 22:2682, 2006.

[151] F. D. Dos Santos and T. Ondarcuhu. *Phys. Rev. Lett.*, 75(16):2972, 1995.

[152] S. Lee and P. Laibinis. *J. Am. Chem. Soc.*, 122:5395, 2000.

[153] G. C. H. Mo, W. Y. Liu, and D. Y. Kwok. *Langmuir*, 21:5777, 2005.

[154] J. Zhang and Y. Han. *Langmuir*, 23:6136, 2007.

[155] G. M. Whitesides and P. E. Laibinis. *Langmuir*, 6:87, 1990.

[156] L. Dubois and R. Nuzzo. *Annu. Rev. Phys. Chem.*, 43:437, 1992.

[157] C. Vericat, M. E. Vela, G. A. Benitez, J. A. Martin Gago, X. Torrelles, and R. C. Salvarezza. *J. Phys.: Condens. Matter*, 18:867, 2006.

[158] G. E. Poirier. *Chem. Rev.*, 97:1117, 1997.

[159] X. Torrelles, C. Vericat, M. Vela, M. H. Fonticelli, M. Millone, R. Felici, T. Lee, J. Zegenhagen, G. Munoz, J. A. Martin-Gago, and R. C. Salvarezza. *J. Phys. Chem. B*, 110:5586, 2006.

[160] A. Dupuis and J. M. Yeomans. *Int. J. Numer. Fluids*, 50:255, 2006.

[161] G. S. Grest, D. R. Heine, and E. B. Webb. *Langmuir*, 22(10):4745, 2006.

[162] J. D. Halverson, J. Koplik, A. Couzis, and C. Maldarelli. *To be submitted.*

[163] J. Koplik, T.-S. Lo, M. Rauscher, and S. Dietrich. *Phys. Fluids*, 18:031104, 2006.

[164] P. A. Thompson, W. B. Brinckerhoff, and M. O. Robbins. *J. Adhesion Sci. Technol.*, 7:535, 1993.

[165] A. E. Ismail, G. S. Grest, and M. J. Stevens. *J. Chem. Phys.*, 125:014702, 2006.

[166] A. Glättli, X. Daura, and W. F. van Gunsteren. *J. Chem. Phys.*, 116(22):9811, 2002.

[167] K. Sekimoto, R. Oguma, and K. Kawaski. *Ann. Phys.*, 176:359, 1987.

[168] S. McNamara, J. Koplik, and J. R. Banavar. *in International Conference on Computational Science-ICCS 2001, V. N. Alexandrov, J. J. Dongarra, B. A. Juliano, R. S. Renner, and C. J. K. Tan, Eds. (Springer, New York, 2001), pp. 551.*

[169] R. M. Sok, H. J. C. Berendsen, and W. F. van Gunsteren. *J. Chem. Phys.*, 96:4699, 1992.

[170] J. Kurzak and B. M. Pettitt. *J. Parallel. Distrib. Comput.*, 65:870, 2005.

[171] L. Greengard and V. Rokhlin. *J. Comput. Phys.*, 73:325, 1987.

[172] J. Board and K. Schulten. *Comput. Sci. Eng.*, page 76, 2000.

[173] J. A. Lupo, Z. Wang, A. M. McKenney, R. Pachter, and W. Mattson. *J. Mole. Graph. Model.*, 21:89, 2002.

[174] J. Martí. *J. Chem. Phys.*, 110:6876, 1999.

[175] C.-T. Hsu, M.-J. Shao, and S.-Y. Lin. *Langmuir*, 16:3187, 2000.

[176] J. R. Lu, R. K. Thomas, and J. Penfold. *Adv. Colloid Interface Sci.*, 84:143, 2000.

[177] J. Venzmer and S. P. Wilkowski. *Pesticide Formulations and Application Systems: 18th. Volume, ASTM STP 1347, J. D. Nalewaja, G. R. Gross, and R. S. Tann, Eds., American Society for Testing and Materials*, 1998.

[178] M. W. Kennedy, J. Venzmer, and S. P. Wilkowski. *FISAA, Memphis*, 1998.

[179] R. M. Hill, M. He., and H. T. Davis. *Langmuir*, 10:1724, 1994.

[180] M. He, Z. Lin, L. E. Scriven, H. T. Davis, and S. A. Snow. *J. Phys. Chem.*, 98:6148, 1994.

[181] J.-B. Maillet, V. Lachet, , and P. V. Coveney. *Phys. Chem. Chem. Phys.*, 1:5227, 1999.

[182] R. Goetz and R. Lipowsky. *J. Chem. Phys.*, 108:7397, 1998.

[183] A. F. de Moura and L. C. G. Freitas. *Chem. Phys. Lett.*, 411:474, 2005.

[184] S. Garde, L. Yang, J. S. Dordick, and M. E. Paulaitis. *Mol. Phys.*, 100:2299, 2002.

[185] G. Srinivas, S. O. Nielsen, P. B. Moore, and M. L. Klein. *J. Am. Chem. Soc.*, 128:848, 2006.

[186] M. Tarek, D. J. Tobias, and M. L. Klein. *J. Chem. Soc., Faraday Trans.*, 92(4):559, 1996.

[187] B. Chen, J. I. Siepmann, and M. L. Klein. *J. Am. Chem. Soc.*, 124:12232, 2002.

[188] S. Bandyopadhyay, J. C. Shelley, M. Tarek, P. B. Moore, and M. L. Klein. *J. Phys. Chem. B*, 102:6318, 1998.

[189] R. Allen, S. Bandyopadhyay, and M. L. Klein. *Langmuir*, 16:10547, 2000.

[190] J. Chanda, S. Chukraborty, and S. Bandyopadhyay. *J. Phys. Chem. B*, 109:471, 2005.

[191] S. Bandyopadhyay and J. Chanda. *Langmuir*, 19:10443, 2003.

[192] J. Alejandre, D. J. Tildesley, and G. A. Chapela. *J. Chem. Phys.*, 102:4574, 1995.

[193] S. E. Feller, R. W. Pastor, A. Rojnuckarin, S. Bogusz, and B. R. Brooks. *J. Phys. Chem.*, 100:17011, 1996.

[194] D. J. Mitchell, G. J. T. Tiddy, L. Waring, T. Bostock, and M. P. McDonald. *J. Chem. Soc., Faraday Trans.*, 79:975, 1983.

[195] G. Fragneto, J. R. Lu, D. C. McDermoott, R. K. Thomos, A. R. Rennie, P. D. Gallagher, and S. K. Satija. *Langmuir*, 12:477, 1996.

[196] S. W. Sides, J. Curro, G. S. Grest, M. J. Stevens, T. Soddemann, A. Habenschuss, and J. D. Londono. *Macromolecules*, 35:6455, 2002.

[197] A. L. Frischknecht and J. G. Curro. *Macromolecules*, 36:2122, 2003.

[198] I. Bahar, I. Zuniga, R. Dodge, and W. L. Mattice. *Macromolecules*, 24:2986, 1991.

[199] J. S. Smith, O. Borodin, and G. D. Smith. *J. Phys. Chem. B*, 108:20340, 2004.

[200] H. Sun, S. J. Hagler, J. R. Maple, and A. T. Hagler. *J. Am. Chem. Soc.*, 116:2978, 1994.

[201] J. M. Stubbs, J. J. Potoff, and J. I. Siepmann. *J. Phys. Chem. B*, 108:17596, 2004.